

Investigations of laser stability in the KATRIN Raman setup and first depolarisation measurements with tritium at TLK

Diplomarbeit

vorgelegt von

Sebastian Fischer

bei Prof. Dr. G. Drexlin

Institut für experimentelle Kernphysik, Fakultät für Physik,
Karlsruher Institut für Technologie

Korreferent Prof. Dr. H.H. Telle
Department of Physics, Swansea University (Wales)

FAKULTÄT FÜR PHYSIK
KARLSRUHER INSTITUT FÜR TECHNOLOGIE

11. JUNI 2010

Erklärung

Hiermit versichere ich, die vorliegende Arbeit selbständig angefertigt, alle dem Wortlaut oder Sinn nach entnommenen Inhalte anderer Werke an den entsprechenden Stellen unter Angabe der Quellen kenntlich gemacht und keine weiteren Hilfsmittel verwendet zu haben.

Sebastian Fischer
Karlsruhe, den 11. Juni 2010

Deutsche Zusammenfassung

Das Ziel des KATRIN (**K**arlsruhe **TR**itium **N**eutrino) Experiment ist die modellunabhängige Bestimmung der Masse m_ν des Elektron-Antineutrinos mit einer Sensitivität von $200 \text{ meV}/c^2$. Dazu untersucht das KATRIN Experiment das Spektrum des β Zerfalls des Wasserstoffisotops Tritium im Bereich des Endpunkt von ca. $18,6 \text{ keV}$, wo sich eine endliche Neutrinomasse auf die Form des β -Spektrums auswirkt. KATRIN verwendet eine fensterlose, gasförmige Tritiumquelle mit hoher Luminosität und einen hochauflösenden elektrostatischen Filter.

Um die geplante Sensitivität von $200 \text{ meV}/c^2$ zur erreichen, muss die systematische Unsicherheit der Observablen m_ν^2 auf $0.017 \text{ eV}^2/c^4$ reduziert werden. Eine vergleichbare statistischen Unsicherheit wird nach einer Messzeit von ca. 3 Jahren erreicht. Zur Minimierung der systematische Unsicherheit muss jede Komponente des KATRIN Experiments auf 10^{-3} genau stabilisiert und entsprechend überwacht werden. Der wichtigste Parameter der Tritiumquelle ist die Gassäulendichte ρd , die durch eine entsprechende Stabilisierung der wesentlichen Parameter der Quelle ebenfalls auf 10^{-3} stabilisiert wird. Zu diesen gehört neben der Temperatur des Quellrohrs, der Einspeiserate des Tritiumgases und der Pumpleistung der verwendeten Turbomolekularpumpen die isotopische Reinheit ε_T des Tritiumgases, das in die Quelle eingespeist wird.

Eine Variation der isotopischen Reinheit ε_T führt zu einer Änderung der Aktivität der Quelle, was sich direkt auf die Zählrate des Detektors und entsprechend auf das zu messende β Spektrum auswirkt. Außerdem führt eine Veränderung von ε_T zur Veränderung von systematischen Effekten in der gasförmigen Quelle, wie z.B. der Streuung der β -Elektronen an Gasmolekülen und zur Änderung der Wahrscheinlichkeiten, dass die Tochtermoleküle des β -Zerfalls sich in einem angeregten Zustand befinden. Beide Effekte führen zu einer Veränderung des β -Spektrum und wirken sich daher auf die Messung von m_ν aus.

Für KATRIN wird daher eine hohe und stabile isotopische Reinheit $\varepsilon_T > 95 \%$ benötigt, was durch einen geschlossenen Tritiumkreislauf, kombiniert mit einer Entfernung von Verunreinigungen und einer Einspeisung mit hochreinem Tritium erreicht wird. Ein Laser Raman (LARA) System wird dazu verwendet die isotopische Reinheit in-line im Tritiumkreislauf kurz vor der Einspeisung in das Quellrohr von KATRIN mit 10^{-3} Präzision zu überwachen. Das dazu genutzte LARA System, LARA1 genannt, wurde in den Jahren 2005 bis 2007 von R. Lewis entwickelt [Lew07], am Tritium Labor Karlsruhe (TLK) aufgebaut und von M. Schlösser eingehend getestet und charakterisiert [Sch09].

Im Rahmen dieser Arbeit wurde ein weiteres LARA System, LARA2, aufgebaut, das primär zur Untersuchung von systematischen Effekten in der Laser Raman Spektroskopie für KATRIN und zur Bestimmung von spektroskopischen Konstanten von Tritium genutzt wird. Beide Systeme haben einen ähnlichen Aufbau, jedoch wurden bei LARA2

aufgrund der unterschiedlichen Anforderungen und aus Kostengründen Komponenten mit geringerer Leistung verwendet.

Im ersten Schwerpunkt dieser Arbeit wurde gezielt der Einfluss von Temperaturschwankungen auf die Stabilität des Systems und insbesondere des Lasers untersucht, da bereits in [Sch09] Temperatureinflüsse für eine Verschlechterung der Präzision der LARA1 Systems verantwortlich gemacht wurden. Das LARA2 System wurde mit einer Probenzelle betrieben, die sich aus Sicherheitsgründen innerhalb einer Handschuhbox befand und somit ermöglichte Tritiummischungen mit über $1.3 \cdot 10^{11}$ Bq zu untersuchen. Viele der aus den Messungen gewonnen Erkenntnisse können aufgrund des ähnlichen Aufbaus und der ähnlichen Komponenten auf das LARA1 übertragen werden und somit zur Verbesserung des KATRIN Experiments beitragen.

Im zweiten Schwerpunkt dieser Arbeit wurde die Möglichkeit getestet, spektroskopische Konstanten von Tritium experimentell zu überprüfen, für die derzeit nur theoretisch berechnete Werte zur Verfügung stehen. Dies ist für KATRIN von Relevanz, da die molekilspezifischen Konstanten zur genauen Bestimmung der Gaszusammensetzung benötigt werden. Die grundsätzliche Möglichkeit einer experimentellen Überprüfung konnte in ersten Messungen gezeigt werden, jedoch müssen noch störende systematische Effekte identifiziert und eliminiert werden, bevor eine tatsächliche Überprüfung der theoretischen Berechnungen möglich ist.

Im Folgenden wird ein kurzer Überblick der einzelnen Kapitel gegeben. Für eine ausführliche Darstellung und die dazugehörigen Quellenangaben sei auf den anschließenden (englischen) Haupttext verwiesen.

1. Einführung

Die Eigenschaften der Neutrinos werden seit ihrer “Erfindung” durch W. Pauli im Jahr 1930 intensiv erforscht. Jedoch ergeben sich für experimentelle Untersuchungen besondere Herausforderungen aufgrund der Tatsache, dass Neutrinos nur schwach wechselwirken und somit schwer nachzuweisen sind. Ein Schwerpunkt der Neutrinoforschung ist die Bestimmung ihrer winzigen Masse, für die es bis heute nur Obergrenzen gibt. Die Entdeckung von Neutrinooszillationen zeigte, dass die verschiedenen Neutrinomassenzustände unterschiedliche und somit von null verschiedene Massen haben, jedoch kann aus diesen Experimenten nicht die tatsächliche Masse bestimmt werden. Obergrenzen für die Summe der drei Neutrinomassen können aus kosmologischen Beobachtungen bestimmt werden, jedoch sind diese stark modellabhängig. Direkte Messungen der Neutrinomasse aus der Untersuchung der Kinematik der β -Zerfälle beruhen alleinig auf der Annahme von Drehimpuls- und Energieerhaltung und ergaben die derzeit strengsten Obergrenzen auf die Neutrinomasse.

2. Das KATRIN Experiment

In diesem Kapitel wird ein Überblick über das KATRIN Experiment gegeben, das die Neutrinomasse in einer direkten, modellunabhängigen Messung aus dem β -Zerfall von Tritium bestimmen wird. Das Ziel von KATRIN ist die Messung von m_ν mit $200 \text{ meV}/c^2$ Sensitivität, was einer Verringerung der derzeitigen Obergrenze um eine Größenordnung entspricht. KATRIN misst dazu das integrierte β -Spektrum des Tritiumzerfalls mit Hilfe des sogenannten elektrostatischen MAC-E Filters¹. Der MAC-E Filter kollimiert die isotrop emittierten Elektronen adiabatisch zu einem breiten Strahl während sie gegen ein elektrostatisches Potential laufen. Elektronen mit genügend großer longitu-

¹Magnetic Adiabatic Collimation and Electrostatic Filter

dinaler Energie können die Potentialbarriere passieren und werden im Detektorsystem nachgewiesen.

Systematische Effekte in der Tritiumquelle von KATRIN machen eine Überwachung der isotopischen Reinheit des Tritiumgases nötig, was mit einem Laser Raman System realisiert wird.

3. Der Raman Effekt

Der Raman Effekt beschreibt die inelastische Streuung von Photonen an Molekülen. Dabei findet eine Änderung des Anregungszustands des Moleküls und ein Energieaustausch zwischen Molekül und Photon statt, was zu einer Änderung der Wellenlänge des gestreuten Lichts gegenüber der ursprünglichen Wellenlänge führt. Anhand des Spektrums des gestreuten Lichts lassen sich die verschiedenen Wasserstoffisotope H_2 , HD, D_2 , HT, DT und T_2 identifizieren und quantifizieren. Daher ist Laser Raman Spektroskopie ein geeignetes Mittel die isotopische Reinheit ε_T in KATRIN zu bestimmen.

Für eine genaue Bestimmung der Gaszusammensetzung sind molekülspezifische Konstanten, die mittlere Polarisierbarkeit a und der anisotrope Anteil γ , nötig. Für Tritium sind derzeit nur theoretisch berechnete Werte vorhanden, die experimentell überprüft werden sollten. Es wird eine Methode zur experimentellen Messung des Verhältnisses a/γ vorgeschlagen, die eine erste Überprüfung ermöglicht.

4. Beschreibung des experimentellen Aufbaus

Die Hauptkomponenten des im Rahmen dieser Arbeit aufgebauten Laser Raman System sind ein 532 nm Laser mit 2 W Ausgangsleistung, eine ultrahoch-vakuumdichte Gasprobenzelle, LARA Zelle genannt, und ein Spektrograph mit CCD Kamera zur Detektion des gestreuten Lichts. Abbildung 1 zeigt den Aufbau und die wesentlichen Komponenten.

Der Laser wird auf den Mittelpunkt der LARA Zelle fokussiert, in dem sich das Tritiumgas befindet. Das gestreute Licht wird senkrecht zur Strahlrichtung gesammelt und auf eine Glasfaser fokussiert, die es zu einem Filter leitet, der die ursprüngliche Wellenlänge des Lasers unterdrückt, bevor es in den Spektrograph eintritt. Dort wird es in Spektrallinien zerlegt, die von einer CCD Kamera in einer Langzeitbelichtung von typischerweise 250 s aufgezeichnet werden. Filter, Spektrograph und Kamera befinden sich aus Platzgründen je nach verwendetem Spektrograph unter oder neben dem optischen Aufbau.

Um höhere Aktivitäten als 10^{10} Bq innerhalb der LARA Zelle handhaben zu können, muss die LARA Zelle aus Sicherheitsgründen von einer zweiten Hülle, in Form einer Handschuhbox, umschlossen sein. In dieser Konfiguration kann die LARA Zelle grundsätzlich mit bis zu 800 mbar befüllt werden, was einer maximalen Aktivität von ca. $6 \cdot 10^{11}$ Bq entspricht.

5. Untersuchungen zur Laserstabilität

Mehrere Messungen wurden mit dem LARA2 Aufbau durchgeführt, u.a. mit einer inaktiven Gasmischung aus $H_2:HD:D_2$ mit ca. 200 mbar Gesamtdruck und einer aktiven Gasmischung mit 217 mbar Gesamtdruck und einer T_2 Konzentration von $> 85\%$. Typische Raman Spektren beider Messungen sind in Abbildung 2 gezeigt. In beiden Messungen konnte eine Variation der Lasertemperatur aufgrund der verschiedenen Betriebsmodi des Lüftungsystems des Labors festgestellt werden. Dies führte zu einer Veränderung der Richtung des Laserstrahls in vorwiegend vertikaler Richtung und somit zu einer Störung der Messung.

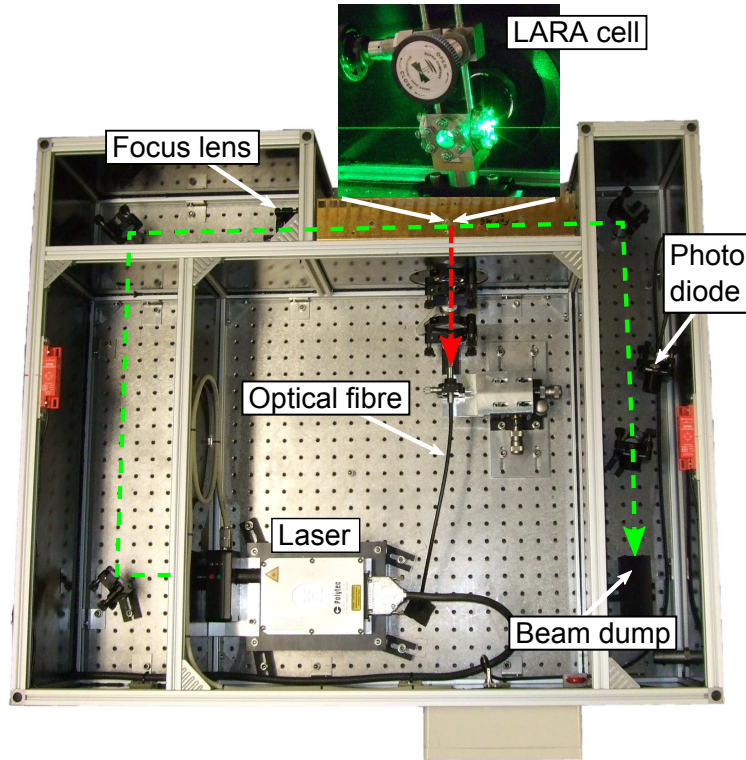


Abbildung 1: Aufsicht auf den LARA2 Aufbau. Zu sehen ist eine Aufsicht auf den LARA2 Aufbau mit den wesentlichen Komponenten: Laser, fokussierende Linse und LARA Zelle und Glasfaser. Das gestreute Licht (rot) wird senkrecht zur Strahlrichtung gesammelt und auf eine Glasfaser fokussiert, die es zum Spektrograph und zur CCD Kamera leitet (beide nicht sichtbar in diesem Bild).

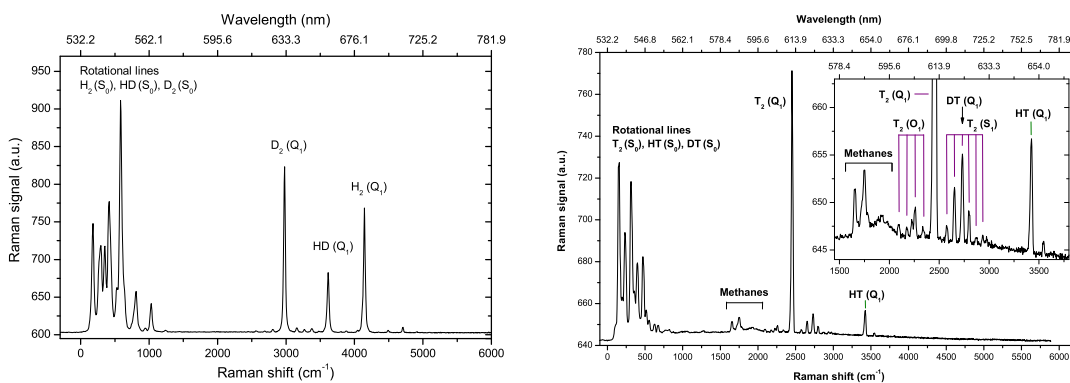


Abbildung 2: Spektrum der H₂:HD:D₂ Messung (links) und der Tritiummessung (rechts). Beide Messungen wurden mit 2 W Laserleistung und einer Belichtungszeit von 250 s aufgenommen. Links sind deutlich die dominierenden Spektrallinien der drei Isotopologe zu sehen. Im rechten Spektrum dominiert Tritium, die weiteren Gasbestandteile HT, DT sowie tritiierte Methane sind im vergrößerten Bildausschnitt zu erkennen.

Entsprechend konnte in diesen Zeiträumen eine deutliche Abnahme der Präzision der Messung im Vergleich zu Phasen mit konstanter Lasertemperatur festgestellt werden; beispielsweise von $3,5 \cdot 10^{-3}$ zu $6,3 \cdot 10^{-3}$ im Falle der Tritiummessung. Des Weiteren wurde eine vermutlich elektromagnetische, Störung der Messelektronik durch den Betrieb von Pumpen und Ventile der Handschuhbox beobachtet. Unstimmigkeiten der redundanten Laserleistungsmessungen wurden festgestellt, welche vermutlich auf Instabilitäten der verwendeten Vorverstärker zurückzuführen ist. Alle Effekte sind nicht tolerierbar und müssen für einen stabilen Betrieb der LARA Systeme unterbunden werden. Dies ist besonders für den in KATRIN verwendeten LARA1 Aufbau von Bedeutung. Ausgehend auf den Ergebnissen dieser Messungen konnten mehrere Verbesserungen vorgeschlagen werden.

6. Erste Depolarisationsmessungen mit Tritium am TLK

Ausgehend auf der in Kapitel 3 entwickelten Methode zur Bestimmung der molekülspezifischen Konstanten a und γ wurden erste Testmessungen an Tritiumgas durchgeführt. Es wurde die Variation der Intensität der Spektrallinien als Funktion der Polarisationsrichtung des einfallenden Laserlichts gemessen. In der vorläufigen Datenauswertung wurde die reale Geometrie des Aufbaus berücksichtigt und eine weitere Korrektur vorgeschlagen, jedoch noch nicht angewandt. Es konnte der grundsätzlich zu erwartende Effekt beobachtet werden und somit die Machbarkeit der experimentellen Bestimmung der a/γ Verhältnisse gezeigt werden. Die quantitative Analyse zeigt jedoch noch eine deutliche systematische Abweichung der experimentellen Werte von den theoretischen Vorhersagen, die auf die derzeit noch nicht vollständige Datenanalyse oder auf einen noch nicht bekannten systematischen Effekt zurückzuführen ist. Aus diesem Grund wird eine erneute, weitergehende Analyse vorgeschlagen, sowie Vergleichsmessungen mit H_2 oder D_2 , für die experimentelle und theoretische Referenzdaten vorhanden sind.

7. Zusammenfassung und Ausblick

Zusammenfassend lässt sich sagen, dass mit dem LARA2 Aufbau ein zweites Messsystem erfolgreich im TLK in Betrieb genommen werden konnte. Eine umfassende Studie von Störeffekten auf den Langzeitbetrieb der LARA Systeme konnte durchgeführt werden und mehrere Störquellen identifiziert werden. Dies erlaubt eine weitere Verbesserung der beiden Aufbauten mit dem Ziel eine Messpräzision von besser als 10^{-3} jederzeit für das KATRIN Experiment garantieren zu können.

Die ersten Messungen und Datenauswertungen zur experimentellen Überprüfung der molekülspezifischen Konstanten a und γ von Tritium zeigen, dass der vorgeschlagene Ansatz erfolgsversprechend ist und weiter verfolgt werden sollte. Jedoch sind weitere Untersuchungen zu systematischen Effekten nötig, um eine ausreichend hohe Genauigkeit für die Überprüfung der theoretischen Werte zu erreichen.

Eine Verbesserung der Präzision und der Nachweisgrenze um mehrere Größenordnungen versprechen fortgeschrittene spektroskopische Methoden wie z.B. Cavity Ring-Down Spectroscopy und Stimulated Raman Spectroscopy, deren Anwendbarkeit auf Wasserstoffisotope in der Zukunft ebenfalls am TLK untersucht werden.

Contents

Deutsche Zusammenfassung	i
Contents	ix
List of Figures	xi
List of Tables	xiii
1 Introduction	1
2 The KATRIN experiment	9
2.1 Neutrino mass measurement using tritium β -decay	9
2.1.1 Tritium β -decay	10
2.1.2 Measurement of the electron spectrum with the MAC-E filter . .	11
2.1.3 Present results of neutrino mass determination	13
2.2 Description of main components of KATRIN	14
2.2.1 The Windowless Gaseous Tritium Source	15
2.2.2 The Transport Section	19
2.2.3 The Tandem Spectrometers	20
2.2.4 The Detector Section	21
2.2.5 The Rear Section	22
2.3 Necessity of Laser Raman measurements for KATRIN	22
3 The Raman effect	25
3.1 Excitation of diatomic molecules	27
3.1.1 Rotational excitation	27
3.1.2 Vibrational excitation	28
3.1.3 Line intensities	34

3.1.4	Population factor for hydrogen isotopologues	35
3.1.5	Line strength function and polarisability tensor	38
3.2	Overview and status of calculations of polarisability	41
3.3	Experimental determination of α/γ ratios	42
4	Description of the experimental setup LARA2	47
4.1	Motivation for second Laser Raman setup at TLK	47
4.2	General description of LARA2	48
4.3	The components of LARA2	50
4.3.1	The breadboard	50
4.3.2	The Excel 2 W laser	51
4.3.3	Laser beam path	53
4.3.4	The LARA cell	53
4.3.5	The collection optics	56
4.3.6	The spectrographs: Spectra Pro 500i and HTS	56
4.3.7	The CCD detectors: PIXIS:400B and PIXIS:2kB	58
4.3.8	Monitoring tools	59
4.3.9	Interlock system and data acquisition	60
4.3.10	Acquisition and processing software	60
5	Investigations of laser stability	63
5.1	Importance of laser stability for KATRIN	64
5.2	Overview of measurements performed	65
5.3	Run#1: Operation without active base plate cooling	65
5.3.1	Experimental setup	65
5.3.2	Measurement and analysis procedure	67
5.3.3	Discussion of Results	67
5.4	Run#2: Long term measurement of H ₂ , HD and D ₂	69
5.4.1	Experimental setup	69
5.4.2	Measurement and analysis procedure	70
5.4.3	Discussion of Results	70
5.5	Run#3: Long term measurement of T ₂ at LOOPINO	74
5.5.1	Experimental setup	74
5.5.2	Measurement procedure and analysis	75

5.5.3	Discussion of Results	75
5.5.3.1	Periodic disturbance of laser power and beam position	80
5.5.3.2	Temperature profile of laser base plate	81
5.5.3.3	Beam position and base plate temperature	82
5.5.3.4	Contradictory trends of laser power readings	83
5.6	Influence of laser stability on precision	85
5.7	Conclusions and consequences for KATRIN	89
6	First depolarisation measurements with tritium at TLK	93
6.1	Consideration of scattering geometry	94
6.1.1	Consideration of solid angle of collection optics	94
6.1.2	Consideration of extended scattering region	98
6.2	Experimental setup	99
6.3	Measurement procedure	100
6.4	Data analysis and preliminary results	101
6.5	Conclusion and consequences for KATRIN	109
7	Summary and Outlook	111
A	Malfunction in position read-out of LM-10 sensor	115
B	Estimate of beam walk at position of LARA cell	117
C	Characterisation of wave plate induced beam-walk	123
D	ROOT Macro for depolarisation measurement	127
	Bibliography	132

List of Figures

1	Aufsicht auf den LARA2 Aufbau	iv
2	Spektrum der H ₂ :HD:D ₂ Messung und der Tritiummessung	iv
1.1	Scenarios of neutrino masses	4
1.2	Neutrino density and neutrino masses	8
2.1	Electron spectrum of tritium β decay	11
2.2	Principle of MAC-E filter	12
2.3	Results of tritium β decay experiments on m_ν^2	13
2.4	The main components of the KATRIN experiment	15
2.5	Schematic drawing of WGTS and tritium density profile	16
2.6	Simplified flow diagram of the KATRIN Inner Loop system	17
2.7	3D model and schematic drawing of WGTS cryostat and source tube	18
2.8	Delivery of the demonstrator to KIT	18
2.9	3D drawing of DPS2-F and picture from the arrival at KIT	20
2.10	The Main Spectrometer surrounded by the external air coil systems	21
3.1	Quantum mechanical picture of Rayleigh and Raman scattering	26
3.2	Schematic drawing of a setup for Raman spectroscopy	26
3.3	Rigid and non-rigid rotator	28
3.4	Morse potential	30
3.5	Energy levels of the harmonic and anharmonic oscillator	31
3.6	Typical Raman spectrum of a diatomic molecule	32
3.7	Line positions in Stokes part of Raman spectra	33
3.8	Theoretical spectrum of T ₂ for a constant line strength function	36
3.9	Theoretical spectrum of all hydrogen isotopologues	37
3.10	Polarisation ellipsoid of a hetero-nuclear molecule	38
3.11	Definition of scattering geometry	39

3.12	Definition of scattering geometry with variable direction of scattered light	43
3.13	Variation of line strength function	44
4.1	Schematic drawing of LARA2 setup	49
4.2	Optics of LARA	50
4.3	Side view of LARA2 setup	51
4.4	Excel laser on heat sink	52
4.5	LARA cell outside of glove box	54
4.6	Simplified flow diagram of LOOPINO	55
4.7	LARA cell inside appendix	55
4.8	Optical fibres	56
4.9	Top view of Czerny-Turner spectrograph and transmitting spectrograph	57
4.10	Quantum efficiency of PIXIS cameras	58
5.1	Run#1: Experimental setup of LARA2	66
5.2	Run#1: Overheating of laser due to insufficient base plate cooling . . .	68
5.3	Run#2: Experimental setup of LARA2	69
5.4	Run#2: Wave plate after damage	70
5.5	Run#2: Spectrum of H ₂ , HD and D ₂	71
5.6	Run#2: Absolute and relative intensities	72
5.7	Run#2: Laser power, beam position and laser base plate temperature .	73
5.8	Run#3: Experimental setup of LARA2	75
5.9	Run#3: Spectrum of T ₂ , DT and HT	76
5.10	Run#3: Absolute and relative intensities of T ₂ , DT and HT	77
5.11	Run#3: Laser power, beam position and laser temperature	79
5.12	Run#3: Oxygen concentration in ISS glove box and laser parameters . .	80
5.13	Run#3: Laser and LARA cell temperature	81
5.14	Run#3: Temperature influence on laser power	84
5.15	Run#2: Achieved precision relative peak intensity of H ₂ , D ₂ and HD . .	87
5.16	Run#3: Achieved precision relative peak intensity of T ₂	88
6.1	Schematic drawing of LARA cell window and flange (Side view)	95
6.2	Scattering geometry and parametrisation of aperture by angles φ and θ	97
6.3	Consideration of extended scattering region	98
6.4	Schematic drawing of LARA cell window and flange (Top view)	99

6.5	Experimental setup of depolarisation measurements	100
6.6	Spectrum of the Q_1 branch of T_2 for $\psi_{\text{mount}} = 88^\circ$ and $\psi_{\text{mount}} = 136^\circ$. . .	101
6.7	Laser parameters during depolarisation measurement	103
6.8	Variation of absolute peak intensities in depolarisation measurement . . .	105
6.9	Data analysis without geometrical considerations	107
7.1	Test of the retro reflection mirror	113
A.1	Malfunction of LM-10 sensor	116
B.1	Experimental setup of LARA2 in run#3	117
B.2	Hypothetical optical setup	119
C.1	Determination of beam walk due to rotation of “thick” wave plate	124
C.2	Determination of beam walk due to rotation of “thin” wave plate	124
C.3	Beam profiles measured with webcam monitor	125
C.4	Beam walk due to rotation of “thick” and “thin” wave plate	126

List of Tables

1.1	Fermions of the standard model	2
3.1	Classification of transitions by selection rules	32
4.1	Specifications of Excel laser	52
4.2	Specifications of available spectrographs at TLK	57
4.3	Specifications of PIXIS cameras	59
5.1	Parameters of Run#1	66
5.2	Parameters of Run#2	69
5.3	Parameters of Run#3	74
5.4	Periods of run#2 and run#3 for calculation of precision	85
6.1	Parameters of depolarisation measurement	100
6.2	Determination of a/γ ratios	106
6.3	Determination of a/γ ratios without geometrical considerations	107
B.1	Typical ray transfer matrices	118
B.2	Parameters for determination of beam walk	119

Chapter 1

Introduction

This work focuses on Laser Raman spectroscopy for the KARlsruhe TRItium Neutrino experiment (KATRIN), which is the next generation tritium β decay experiment. The aim of KATRIN is the direct, i.e. model independent, measurement of the electron anti-neutrino mass with 200 meV sensitivity which corresponds to an improvement in sensitivity by a factor of 10 to foregoing experiments. This chapter gives a brief overview of neutrinos, their properties and relevance for cosmology and the measurements of the neutrino mass.

Postulation and first detection of neutrinos

In 1914 the electron spectrum of the β decay of ^{214}Pb and ^{214}Bi was measured by J. Chadwick [Cha14] and a continuous spectrum was observed. This was contradictory to the expectation of a discrete spectrum with a distinct electron energy since it was assumed that the β decay is a two-body decay, similar to α and γ decay. In order to explain the observed continuous β spectrum without violation of energy conservation the anti-neutrino¹ $\bar{\nu}_e$ was postulated by W. Pauli [Pau30] as a third particle that also participates in the, now three-body, β decay

$$n \rightarrow p + e^- + \bar{\nu}_e. \quad (1.1)$$

Since it is electrical neutral, the neutrino can leave the experiment without being observed but carries away the energy which is necessary to fulfil energy conservation.

Based on this hypothesis E. Fermi developed a theoretical description of β decay, which is still valid today for low energies when taking the violation of parity conservation into account, and concluded that the shape of the high energetic end of the β spectrum depends on the mass of the neutrino which has to be small in comparison to the mass of the electron [Fer34].

The first neutrino, the electron anti-neutrino, was discovered in 1956 by F. Reines and C. L. Cowan [Rei56] by the inverse β decay reaction

$$\bar{\nu}_e + p \rightarrow n + e^+ \quad (1.2)$$

¹Pauli initially proposed the name “neutron”. After the discovery of the neutral nucleus, the neutron, in 1932 [Cha32a] [Cha32b], the nomenclature for the hypothetical particle was changed to “neutrino” since the observed neutron was too heavy to be the postulated particle by Pauli.

Table 1.1: Fermions of the standard model. The 12 fermions and their possible interactions are summarised in this table. The fermions are subdivided into three generations.

	Generations			Electric	Spin	Interactions
	1	2	3	Charge		
Leptons	ν_e	ν_μ	ν_τ	0	1/2	Weak
	e^-	μ^-	τ^-	$- e $	1/2	Weak, electromagnetic
Quarks	u	c	t	$+2/3 e $	1/2	Weak, electromagnetic, strong
	d	s	b	$-1/3 e $	1/2	Weak, electromagnetic, strong

using a water filled detector located close to the Savannah River Reactor (USA) nuclear power plant which acted as an intense source of electron anti-neutrinos $\bar{\nu}_e$. The tiny experimentally determined cross section of $\sigma = (11 \pm 2.6) \cdot 10^{-44} \text{ cm}^2$ for the inverse β decay reaction [Rei59] was in agreement with theoretical predictions.

Evidence for a second generation of neutrinos, the muon neutrinos ν_μ , was found by Lederman, Schwartz and Steinberger in 1962 in the AGS neutrino experiment in Brookhaven [Dan62]. The discovery of the third generation of neutrinos, the tau neutrinos ν_τ , was achieved in 2000 by Kodama et al. in the DONUT experiment [Kod01] at the Tevatron accelerator. A fourth generation of light neutrinos, i.e. with $m_\nu < 45 \text{ GeV}/c^2$, is not expected to exist since it was not found at the e^+e^- collider LEP at CERN and since the total number $N = 2.92 \pm 0.05$ of light neutrino generations was determined from the decay width of the Z boson [PDG08].

The three neutrinos and their corresponding anti-particles are part of the standard model of particle physics that describes the 12 fundamental fermions and their anti-particles as well as the bosons that mediate the forces between the fermions. The fermions and their possible interactions are shown in table 1.1. The neutrinos are massless according to the standard model although a non-zero mass can be included into it.

Non-zero neutrino masses and neutrino oscillations

If neutrinos have non-zero masses m_1 , m_2 and m_3 , the weak flavour eigenstates $|\nu_\alpha\rangle = |\nu_e\rangle, |\nu_\mu\rangle, |\nu_\tau\rangle$ will, in general, not be identical with the mass eigenstates $|\nu_i\rangle = |\nu_1\rangle, |\nu_2\rangle, |\nu_3\rangle$. The flavour eigenstates are described as superpositions of the mass eigenstates, connected by a unitary 3×3 mixing matrix U

$$|\nu_\alpha\rangle = \sum_k U_{\alpha k} |\nu_k\rangle, \quad (1.3)$$

similar to the CKM matrix in the quark sector that connects the weak and strong eigenstates of the quarks. After the generation of a neutrino with total energy E and flavour α in a weak interaction its mass eigenstates travel in space with different

velocities depending on their masses m_i . This yields to a non-zero probability

$$\begin{aligned} P(\alpha \rightarrow \beta; L, E) &= \left| \sum_k U_{\alpha k} U_{\beta k}^* e^{-i \frac{m_k^2}{2} \cdot \frac{L}{E}} \right|^2 \\ &= \sum_{kl} U_{\alpha k} U_{\alpha l}^* U_{\beta k}^* U_{\beta l} e^{-\Delta_{kl}(L, E)} \end{aligned} \quad (1.4)$$

to observe the neutrino after a certain path length L being in a different flavour eigenstate $\beta \neq \alpha$ than the initial flavour eigenstate with

$$\Delta_{kl}(L, E) = \frac{\Delta m_{kl}^2}{2} \cdot \frac{L}{E} \quad \text{and} \quad \Delta m_{kl}^2 = m_k^2 - m_l^2 \quad (1.5)$$

[Sch97]. This phenomena is called neutrino oscillation and was proposed by Pontecorvo in 1967 [Pon67] [Gri69] for the two neutrino flavours (ν_e, ν_μ) which were known at that time. The path length L is often also referred to as *baseline*.

In case of two neutrino flavours, i.e. $\Delta m^2 = m_1^2 - m_2^2$, equation 1.4 can be simplified to

$$P(\alpha \rightarrow \beta; L, E) = \sin^2 2\theta \cdot \sin^2 \left(1.267 \cdot \Delta m^2 [\text{eV}^2] \frac{L [\text{m}]}{E [\text{MeV}]} \right) \quad (1.6)$$

where θ is referred to as the mixing angle [Sch97]. The oscillation probabilities change if the neutrinos travel through matter instead of vacuum due to the MSW² effect [Wol78], a resonance effect of the $\bar{\nu}_e$ with the electrons of the surrounding matter. Note that the probability for a neutrino oscillation always depends on the difference of the squares of the mass eigenvalues but not on the absolute value of the mass eigenvalues.

Neutrino oscillations were observed in the last decade for atmospheric neutrinos (e.g. by Super-Kamiokande [Fuk98]), neutrinos from nuclear reactor (e.g. by KamLAND [Egu03]), and neutrinos from particle accelerators (e.g. by K2K [Ali05] and MINOS [Mic06]) using different baselines. Neutrino oscillation played also an important role in case of solar neutrinos since it allowed to explain the so-called solar neutrino problem.

The sun continuously emits electron neutrinos which are produced in fusion reactions. The net reaction is given by



with neutrino energies of the order of a few MeV [Sch97]. A significant deficit in the electron neutrino flux rate from the sun was observed by R. Davis in the Homestake experiment [Dav68] compared to the theoretical predictions. Other experiments, e.g. GALLEX [Ans92], verified but also could not explain this deficit. The solar neutrino problem was solved in 2001 when the Sudbury Neutrino Observatory (SNO) measured the first time the *total* neutrino flux rate, i.e. the flux rate of ν_e, ν_μ and ν_τ , from the sun using 1000 tons of heavy water (D₂O) and 2 tons of salt (NaCl) as detector material. The total neutrino flux rate of $(5.44 \pm 0.99) \cdot 10^6 \text{ cm}^2 \text{ s}^{-1}$ [Ahm01] was in very good agreement with the predictions of the standard solar models [Bah06] [Tur01] and indicated that a fraction of the electron neutrinos that are produced in the sun change their flavour on their way to the earth due to neutrino oscillation.

²Mikheyev-Smirnov-Wolfenstein

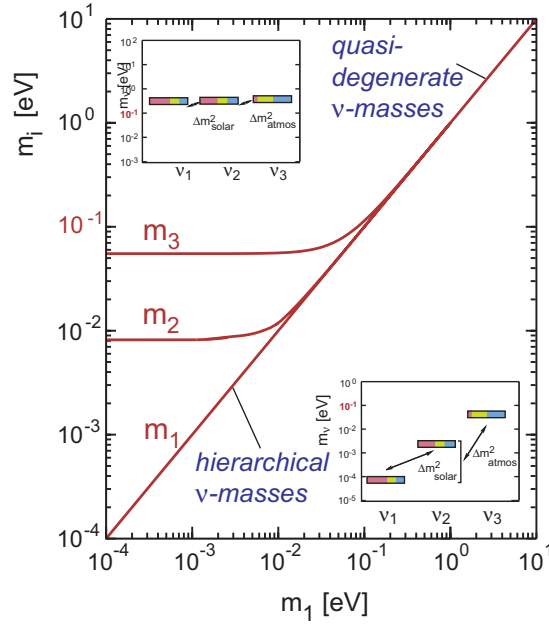


Figure 1.1: Scenarios of neutrino masses. The masses of the three neutrino mass eigenstates m_1 , m_2 , m_3 are shown as a function of the lightest eigenstate with mass m_1 . In the case of the quasi-degenerate scenario, the lightest neutrino mass m_1 is large in comparison to the mass splittings and hence all mass eigenstates have comparable masses. In case of the hierarchical scenario, m_1 is small in comparison to the mass splittings and hence the neutrino mass eigenstates differ significantly in mass. Figure taken from [KAT05].

The two mass splittings

$$\begin{aligned}\Delta m_{\text{solar}}^2 &\equiv \Delta m_{12}^2 = (7.59 \pm 0.20) \cdot 10^{-5} \text{ eV}^2/c^4 \\ \Delta m_{\text{atm}}^2 &\equiv \Delta m_{32}^2 = (2.43 \pm 0.13) \cdot 10^{-3} \text{ eV}^2/c^4\end{aligned}\quad (1.8)$$

between the three mass eigenstates are determined by an analysis of neutrino oscillations of solar and atmospheric neutrinos, respectively [PDG08], and show that the third mass eigenstate is significantly separated from the two other mass eigenstates. A hierarchical and a quasi-degenerate scenario of neutrino masses (indicated in figure 1.1) are possible since the absolute neutrino mass scale is not yet determined.

Determination of absolute neutrino mass scale

The measurement of the absolute mass of at least one neutrino species allows to determine the masses of all neutrinos using the mass splittings obtained from neutrino oscillation experiments. This can be accomplished by indirect and direct measurements which will be briefly explained in this section.

The two most important indirect neutrino mass measurements are the neutrinoless double- β decay and cosmological observations.

- **Neutrinoless double- β decay**

The “normal” double- β decay ($2\nu\beta\beta$ decay) is a simultaneous β decay of two neutrons in a nucleus (A, Z) with mass number A and atomic number Z

$$(A, Z) \rightarrow (A, Z + 2) + 2e^- + 2\bar{\nu}_e \quad (1.9)$$

in which two electrons e^- and two electron anti neutrinos $\bar{\nu}_e$ are emitted. The $2\nu\beta\beta$ decay is a rare but allowed process in the standard model of particle physics and was first observed in 1987 [Ell87]. The spectrum of the total energy of the two emitted electrons is continuous since the neutrinos can carry away an arbitrary fraction of the available kinetic energy.

The neutrinoless double- β decay ($0\nu\beta\beta$ decay)

$$(A, Z) \rightarrow (A, Z + 2) + 2e^- \quad (1.10)$$

is a hypothetical, beyond standard model process that violates the lepton number [Ott08] [Sch97]. In the $0\nu\beta\beta$ decay the neutrino is a virtual particle which is emitted as right-handed ν_R particle in the first β decay $n \rightarrow p + e^- + \bar{\nu}_e$ and absorbed in the second inverse β decay $\nu_e + n \rightarrow p + e^-$ as left-handed ν_L particle. This is only possible if the neutrino is a Majorana neutrino and hence its own anti particle, i.e. $\bar{\nu}_e = \nu_e$ and $\nu_L = \bar{\nu}_L$ ($\nu_R = \bar{\nu}_R$). The change of helicity is possible if neutrinos are massive particles. The signature of the $0\nu\beta\beta$ decay is a monoenergetic energy spectrum of the total energy of the two emitted electrons at $Q = (m(A, Z) - m(A, Z + 2)) c^2$.

The so-called effective neutrino mass m_{ee} is the coherent sum of the mass eigenstates m_j and is connected to the decay rate $\Gamma_{0\nu\beta\beta}$ of the $0\nu\beta\beta$ decay [Cho07]

$$\Gamma_{0\nu\beta\beta} = G^{0\nu\beta\beta} |M_{\text{nuc}}|^2 m_{ee}^2 \quad \text{with} \quad m_{ee} = \left| \sum_{j=1}^3 U_{ej}^2 m_j \right| \quad (1.11)$$

where U_{ej} are the now complex elements of the neutrino mixing matrix since they include complex Majorana phases. M_{nuc} is the nuclear matrix element of the $0\nu\beta\beta$ decay and $G^{0\nu\beta\beta}$ a phase space factor. Due to the complex Majorana phases the effective neutrino mass m_{ee} can be smaller than the masses m_j of the mass eigenstates. The Heidelberg-Moskow-Experiment has reached the highest sensitivity on m_{ee} by the investigation of the ^{76}Ge decay. The collaboration published a 4.2σ evidence for $m_{ee} = (0.24 - 0.58) \text{ eV}/c^2$ [Kla04] which is controversially discussed in the community. Several experiments, e.g. GERDA [Sch05], Majorana [Aal05], Cuore [Ped08] and EXO [Aki05] aim to verify this result.

- **Neutrino masses from cosmological observations**

The cosmic microwave background (CMB) and its non-statistical fluctuations are a relict from the decoupling of the photons from matter, about 380,000 years after the Big Bang. It was mapped in highest detail by the WMAP satellite [Ben03]. The CMB can be described as a black body radiation with $(2.728 \pm 0.004) \text{ K}$ temperature [Fix96] with fluctuations on the 10^{-5} level which represent the distribution of matter in the early universe. An expansion of the temperature fluctuations in spherical harmonics up to the power $l \approx 1000$ is used to deduce cosmological parameters like the total mass density Ω_{tot} , the dark energy mass density Ω_{Λ} , the matter mass density Ω_{m} , the baryonic mass density Ω_{b} and the neutrino density Ω_{ν} .

Based on the seven-year data of WMAP the upper limit on the sum of the neutrino masses is [Kom10]

$$\sum m_{\nu} < 1.3 \text{ eV}/c^2 \quad (95 \% \text{C.L.}). \quad (1.12)$$

When combined with the latest distance measurements from the Baryon Acoustic Oscillation (BAO) in the distribution of galaxies [Per09] and the measurement of the Hubble constant [Rie09] the upper limit on the sum of the neutrino masses can be further lowered to [Kom10]

$$\sum m_\nu < 0.58 \text{ eV}/c^2 \quad (95 \text{ \%C.L.}). \quad (1.13)$$

Both limits are strongly model dependent since cosmological models have to be applied for the deduction of the neutrino mass from the multipole expansion of the temperature fluctuations of the CMB.

The direct neutrino mass measurements are based on the relativistic energy momentum relation

$$E^2 = p^2 c^2 + m^2 c^4 \quad (1.14)$$

which connects the total energy E with the momentum p , the speed of light c and the rest mass m . The direct measurements can be subdivided into time-of-flight measurements and the study of weak decays.

- **Time-of-flight measurements from supernova neutrinos**

Supernovas, and especially the type II supernovas, are intense astrophysical sources of neutrinos. During the core collapse of the progenitor star typically about 10^{57} protons are “neutronised”, i.e. they are transformed into neutrons by the electron capture reaction



within about 100 msec [Sch97]. Neutrinos are also produced by the thermal neutrino pair production

$$e^+ + e^- \rightarrow \nu_\alpha + \bar{\nu}_\alpha \quad \text{with } \alpha = e, \mu, \tau. \quad (1.16)$$

The neutrinos are emitted from the star within about 10-20 s since they scatter several times in the very dense ($\rho \approx 5 \cdot 10^{14} \text{ g/cm}^3$) core material. They carry away about $10^{53} \text{ erg} \approx 10^{46} \text{ J}$, i.e. about 99 % of the gravitational energy which is released by the supernova [Sch97].

About two dozen neutrinos from the famous supernova 1987A in the Large Magellanic Cloud were detected within about 10 sec by neutrino detectors at Baksan, Caucas [Ale88], in the Morton Thiokol mine, Ohio [Bra88] and in the Kamioka mine, Japan [Hir88]. The energy of the neutrinos varied from about 10 - 40 MeV with the more energetic neutrinos arriving before the less energetic ones. Assuming that the neutrinos were emitted simultaneously and applying further assumptions concerning the dynamics of the supernova an upper limit on the electron neutrino mass of

$$m_{\nu_e} < 5.7 \text{ eV}/c^2 \quad (95 \text{ \%C.L.}) \quad (1.17)$$

can be deduced [Lor02].

- **Study of weak decays**

The study of the electron spectrum from nuclear β decay

$$(A, Z) \rightarrow (A, Z + 1) + e^- + \bar{\nu}_e \quad (1.18)$$

allows to determine the mass m_{ν_e} of the electron anti neutrino. The currently most stringent limit [PDG08] of

$$m_{\nu_e} < 2 \text{ eV}/c^2 \quad (95\% \text{ C.L.}) \quad (1.19)$$

on the electron anti neutrino mass were achieved by the study of the tritium β decay which will be discussed in detail in section 2.1.

Another promising candidate for the study of the kinematics of β decays is the isotope ^{187}Re which can be used to build cryogenic bolometers that act simultaneously as β source and detector. The energy released by the β decay of ^{187}Re is deposited in the bolometer and detected as a temperature rise of the bolometer.

The Milano experiment [Sis04] published the most stringent limit of

$$m_{\nu_e} < 15 \text{ eV}/c^2 \quad (90\% \text{ C.L.}) \quad (1.20)$$

from ^{187}Re β decay experiments. The successor experiment MARE-I aims to improve the sensitivity to about $2 \text{ eV}/c^2$ [Sis07].

Impact of non-zero neutrino masses on cosmology

The Big Bang has left a blackbody radiation of so-called relic neutrinos, similar to the cosmic microwave background, with an average density of 10^9 neutrinos per baryon in the universe. At the time of decoupling from matter (< 2 s after the Big Bang) the relict neutrinos had an average energy of about $1 - 2$ MeV and hence were still relativistic. They therefore contribute to the total matter density Ω_{tot} of the universe as neutrino hot dark matter (νHDM) due their large number and small but non-zero masses. The relic neutrinos played an important role in the formation of large scale structure in the early universe since νHDM was able to smear out matter density fluctuations in diffusion-like processes [Han04] [Ott08]. The neutrino density Ω_ν contribution to Ω_{tot} depends on the sum of the neutrino masses

$$\Omega_\nu h^2 = \sum m_\nu / 94 \text{ eV} \quad (1.21)$$

where h is the Hubble constant. The parameter space for Ω_ν is constrained by experiments to the interval $0.001 < \Omega_\nu < 0.15$ whereby the upper limit comes from tritium β decay experiments and the lower limit from the measurement of the atmospheric mass splitting Δm_{atm}^2 .

The determination or a significant constraint of the neutrino masses and hence of Ω_ν would lead to a better understanding of the role of νHDM in formation of large scale structure in the early universe. The projected sensitivity of $200 \text{ meV}/c^2$ (90 % C.L.) of the KATRIN (KArlsruhe TRItium Neutrino) experiment will allow to probe Ω_ν down to about 0.01 as shown in figure 1.2.

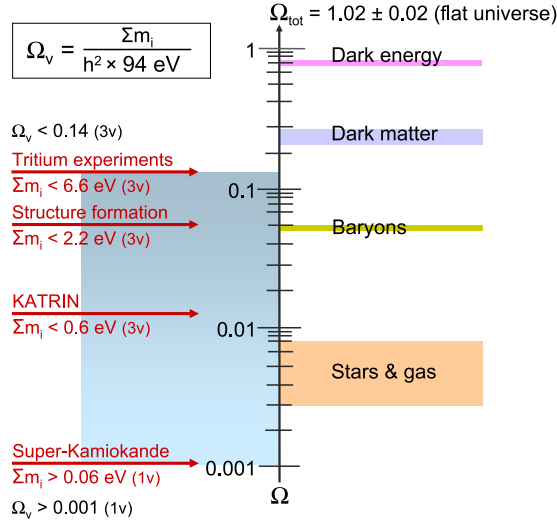


Figure 1.2: Neutrino density and neutrino masses. The contributions of dark energy, cold dark matter, baryonic matter to the total matter density Ω_{tot} is compared to Ω_ν . The currently allowed parameter space of Ω_ν will be probed by the KATRIN experiment down to about 0.01 [KAT05].

In order to reach 200 meV sensitivity the total systematic uncertainty of the KATRIN experiment has to be significantly reduced in comparison to the foregoing experiments. This will be amongst others achieved by a stabilisation of the key parameters of KATRIN to 10^{-3} level.

A Laser Raman (LARA) setup is used in the KATRIN experiment to monitor the gas composition of the tritium gas before being injected into the source part of KATRIN. The long term stability of the LARA setup, and especially of the built-in laser, and its response to changes of environmental conditions are crucial for the reliability of the LARA measurement during non-stop operation over typical measurement periods of about 60 days. The impact of temperature variations and environmental influences on the stability of the laser is investigated within this thesis. Furthermore first measurements of molecular specific constants of tritium, which are necessary for the accurate determination of the gas composition, are performed within this work.

This thesis is structured in the following way: After an introduction into tritium β decay experiments, and the KATRIN experiment in particular, in chapter 2 the fundamentals of Laser Raman spectroscopy are described in chapter 3. The experimental setup for Laser Raman spectroscopy, which was build up within the scope of this thesis, is described in chapter 4. Chapter 5 focuses on investigations concerning the stability of the laser in the LARA setup. The first measurement of the molecular specific constants which are necessary for the accurate determination of the gas composition are described in chapter 6.

Chapter 2

The KATRIN experiment

The aim of the KATRIN experiment is the model independent measurement of the electron anti-neutrino mass m_ν by the study of the electron spectrum of the tritium β decay. After 3 years of measurement time the expected sensitivity for a neutrino mass discovery with 5σ significance is $0.35 \text{ eV}/c^2$ [KAT05]. If the shape of the tritium β spectrum is compatible with a zero anti-neutrino mass, KATRIN will be able to set an upper limit of $m_\nu < 0.2 \text{ eV}/c^2$ (90 % C.L.). This corresponds to a reduction of the current upper limit on m_ν by one order of magnitude.

In this chapter an overview of the KATRIN experiment will be given. Section 2.1 gives a general description on the tritium beta decay (2.1.1) and the so-called MAC-E filter (2.1.2) which is used for the measurement of the electron spectrum. The results of the previous direct neutrino mass measurements are summarised in subsection 2.1.3. In section 2.2 the major components of KATRIN are presented. The influence of systematic effects on the sensitivity of the neutrino mass determination and the need of a continuous monitoring of the gas composition in the source are presented in section 2.3. This chapter mainly bases on [KAT05].

2.1 Neutrino mass measurement using tritium β -decay

The study of the kinematics of weak decays, in particular of the tritium β decay, is a suitable method for the determination of the neutrino mass. For this reason, neutrino mass measurements based on tritium β decay were performed since the forties. All results until 1972 were compatible within the error bars with a vanishing anti-neutrino mass and hence only upper limits on the anti-neutrino mass were stated [Ber72]. In 1980 an evidence for anti-neutrino mass between 14 and 46 eV/c^2 was found [Lub80] but was soon disproved by other experiments. In the nineties the sensitivity of the experiments had improved but still only upper limits could be given on the anti-neutrino mass. The results of the last 20 years will be discussed in detail in subsection 2.1.3.

2.1.1 Tritium β -decay

The tritium β decay



allows the determination of the electron anti-neutrino mass m_ν ¹ by the measurement of the energy spectrum of the emitted electron. Tritium is one of the best suited isotopes for neutrino mass experiments due to five fundamental aspects:

- The fraction of decay events that is relevant for the determination of m_ν is proportional to $1/E_0^3$ where E_0 is the endpoint energy of the *beta* decay, i.e. the total decay energy minus the recoil energy of the daughter nucleus. The endpoint energy of tritium is $E_0 \approx 18.6$ keV and the second lowest endpoint energy of all β emitters.
- The tritium β decay is a super-allowed decay with a rather short half-life of 12.3 y. This allows to setup up a source of β electrons with high spectral activity by a rather small amount of tritium.
- The nuclear matrix element of the super-allowed tritium β decay is independent of the electron energy and m_ν . Therefore the dependence of the spectral shape on m_ν is only given by the phase space.
- The probability that a β electron inelastically scatters on tritium in the source and therefore loses energy is low due to the low atomic number of tritium.
- The electron shell and the nucleus of helium and the hydrogen isotopologue tritium are very simple. This allows to reliably calculate the final states of the β decay taking the molecular rotational and vibrational excitations [Dos08] and radiative corrections [Rep83] into account.

The spectrum of the emitted electrons, i.e. the number of emitted electrons with a certain energy E per time interval, can be calculated from Fermi's golden rule [Wei03]

$$\frac{d^2N}{dt dE} = C \cdot F(Z, E) \cdot p(E + m_e c^2)(E_0 - E) \sqrt{(E_0 - E)^2 - m_\nu^2 c^4} \cdot \Theta(E_0 - E - m_\nu c^2) \quad (2.2)$$

where m_ν is the mass of the electron anti-neutrino. E , p and m_e are the kinetic energy, the momentum and the mass of the β electron. $F(Z, E)$ is the Fermi function which takes into account the coulomb interaction of the emitted electron with the positive charged helium nucleus ${}^3\text{He}^+$. It is independent of m_ν and precisely known due to the simple nuclear structure of tritium and ${}^3\text{He}$. E_0 is the so-called endpoint energy, i.e. the total decay energy minus the recoil energy of the daughter nucleus. The step function $\Theta(E_0 - E - m_\nu c^2)$ ensures energy conservation. The constant

$$C = \frac{G_f^2}{2\pi^3 \hbar^7 c^5} \cos^2 \theta_c |M_{\text{nuc}}|^2 \quad (2.3)$$

is given by the Fermi constant G_f , the Cabbibo angle θ_c and the nuclear matrix element M_{nuc} of the tritium β decay [Kra05]. Note that the actual observable in (2.2) is m_ν^2 and not m_ν .

¹For simplification the notation m_ν is used instead of the actual notation $m_{\bar{\nu}_e}$.

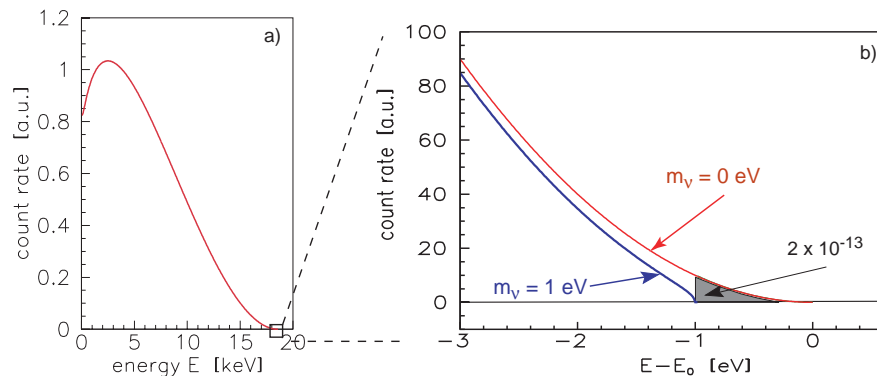


Figure 2.1: Electron spectrum of tritium β decay. *Left:* Full β spectrum. The count rate decreases towards the endpoint of $E_0 = 18.6$ keV. *Right:* The last 3 eV of the β spectrum before the endpoint. In this region the effect of a non-vanishing electron anti-neutrino mass on the spectrum becomes present; here shown for the case $m_\nu = 1$ eV/ c^2 . Only a fraction of $2 \cdot 10^{-13}$ of all β decays falls into the last eV of the spectrum [KAT05].

The electron spectrum depends on m_ν^2 , but a significant influence is only visible if $(E_0 - E)^2 \approx m_\nu^2 c^4$, i.e. for electron energies close to the endpoint. In figure 2.1 the full spectrum is plotted as well as the section close to the endpoint for the two cases $m_\nu = 0$ and $m_\nu = 1$ eV/ c^2 . The neutrino mass m_ν is usually determined by a four-parameter fit of equation (2.2) to the measured electron spectrum with the fit parameters C , m_ν^2 and E_0 and background rate.

Besides the symbol ${}^3\text{H}$, tritium is typically also denoted by T which will be the standard nomenclature of this thesis.

2.1.2 Measurement of the electron spectrum with the MAC-E filter

The so-called MAC-E filter (magnetic adiabatic collimation combined with an electrostatic filter), developed by Kruit and Head [Krui83], has become the standard technique in the last 2 decades years for the measurement of the endpoint region of the tritium β spectrum.

The Magnetic Adiabatic Collimation (MAC) is a concept to adiabatically collimate the electrons, that were isotropically emitted in the source, while they are running against the Electrostatic ($-E$) retarding potential. Without this collimation, some electrons could not pass the filter even if they had enough kinetic energy because only the kinetic energy component parallel to the electrostatic retarding potential determines if the electrons are transmitted or not. The principle of the magnetic adiabatic collimation is described in detail in figure 2.2. The MAC-E filter acts as an electrostatic high-pass filter that rejects all electrons below a chosen kinetic energy $|eU|$, where e is the charge of the electron and U the applied retarding voltage. Electrons with higher energies can pass the filter and reach a detector which counts the electrons. Hence the MAC-E filter measures the integrated β spectrum, i.e.

$$\int_{E=eU}^{E_0} \frac{d^2 N}{dt dE} dE. \quad (2.4)$$

Not all transversal energy is transferred into longitudinal energy by the MAC-E filter. The remaining transversal kinetic energy ΔE of the electrons in the analysis plane,

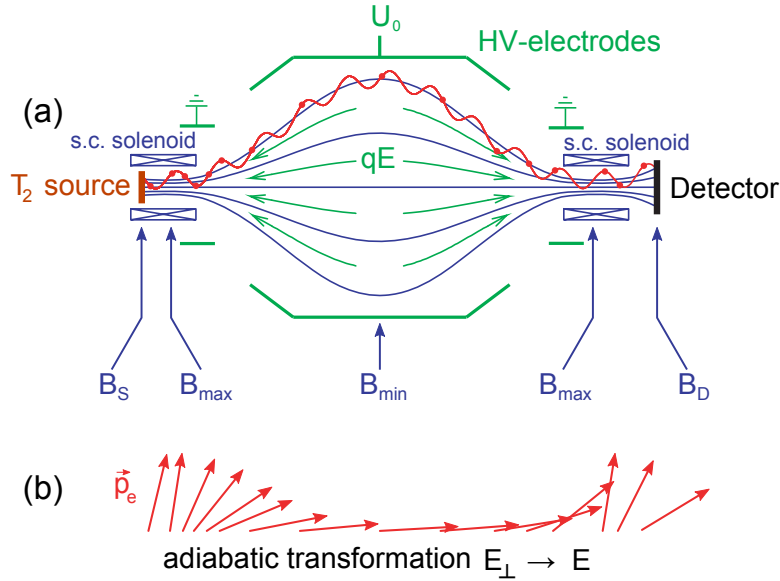


Figure 2.2: Principle of MAC-E filter. (a) A superconducting solenoid is placed in front, i.e. on the left side, of a vacuum vessel. The tritium source, which is placed into the centre of the solenoid for the sake of simplicity, isotropically emits electrons. Electrons that are emitted into a solid angle of nearly 2π are caught by the magnetic field lines (blue) and enter the vacuum tank while spiralling around the diverging magnetic field lines due to the cyclotron motion. The magnetic field strength drops by many orders of magnitude towards the centre of the vacuum tank. Therefore the magnetic gradient force transfers nearly all energy of the cyclotron motion into longitudinal energy which is illustrated by the momentum arrows in (b). This transfer is adiabatic since the magnetic field strength drops slowly enough during one cycle of the cyclotron motion. The electrons are simultaneously flying against a electrostatic retarding potential, formed by the cylindrical electrodes (green), that reaches its maximum at the centre of the vacuum vessel. Electrons with high enough longitudinal kinetic energy can pass the retarding potential and reach the detector while low energetic electrons are deflected. Behind the maximum of the electrostatic barrier, the electrons are re-accelerated and the magnetic field lines converge towards a second superconducting solenoid placed at the back of the vacuum vessel. Therefore all electrons that can pass the electrostatic barrier in the centre of the the vessel are guided to and counted by the detector that is placed behind the second solenoid. According to [KAT05].

i.e. the plane in which the electrostatic potential reaches its maximum, determines the relative sharpness $\Delta E/E$ of the electrostatic filter. $\Delta E/E$ depends only on the ratio of the minimum magnetic field strength B_A to the maximum magnetic field strength.

$$\frac{\Delta E}{E} = \frac{B_A}{B_{\max}} \quad (2.5)$$

B_{\max} can be enlarged up to technical feasible field strengths of several Tesla to improve the relative sharpness of an MAC-E filter. Alternatively, B_A can be reduced down to certain limits: The earth's magnetic field becomes non-negligible and has to be compensated. The size of the spectrometer vessel, which increases with decreasing B_A due to the conservation of magnetic flux, is also limited due to technical limits.

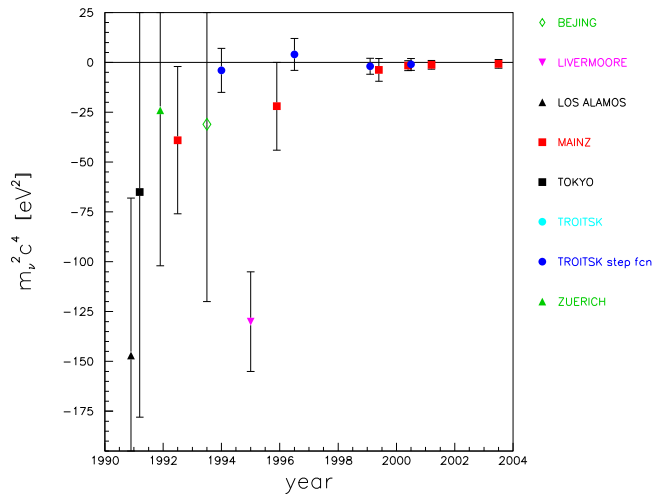


Figure 2.3: Results of tritium β decay experiments on m_ν^2 . The sensitivity of direct neutrino mass measurements increased significantly in the last 20 years. [KAT05]

2.1.3 Present results of neutrino mass determination

The results of tritium β decay experiments of the last 20 years are shown in figure 2.3.

Until now all tritium β decay experiments, besides the controversial result from 1980, have yielded only upper limits on the neutrino mass. The two most stringent limits in the last 14 years were set by the experiments in Mainz and Troitsk which both used a MAC-E filter. These results shall be presented briefly now.

In the Troitsk experiment a MAC-E filter and a windowless gaseous tritium source (WGTS) were used. The result of the analysis of the data from 1994-1998 [Lob99] is

$$m_\nu^2 = (-1.9 \pm 3.4_{\text{fit}} \pm 2.2_{\text{syst}}) \text{ eV}^2/c^4. \quad (2.6)$$

This corresponds to an upper limit on the anti-neutrino mass of

$$m_\nu < 2.5 \text{ eV}/c^2 \quad (95\% \text{ C.L.}). \quad (2.7)$$

An improved result was published in a conference proceeding in 2003 with $m_\nu^2 = -2.3 \pm 2.5 \pm 2.0 \text{ eV}^2/c^4$ and $m_\nu < 2.05 \text{ eV}/c^2$ (95% C.L.) [Lob03] but is not taken into account by the Particle Data Group [PDG08].

The Mainz experiment used a MAC-E filter and a quench condensed tritium source. The analysis of the last 70 eV before the endpoint of the data from 1998, 1999 and 2001 [Kra05] results in

$$m_\nu^2 = (-0.6 \pm 2.2_{\text{stat}} \pm 2.1_{\text{syst}}) \text{ eV}^2/c^4 \quad (2.8)$$

This is also compatible with $m_\nu = 0$ but gives the current best upper limit on m_ν of

$$m_\nu < 2.3 \text{ eV}/c^2 \quad (95\% \text{ C.L.}) \quad (2.9)$$

for a direct neutrino mass measurement.

A combined analysis of the Particle Data Group, based on the upper limit from the Troitsk and Mainz experiments, yields to an upper limit of $m_\nu < 2 \text{ eV}/c^2$ (95% C.L. [PDG08]) on the electron anti neutrino mass.

As already shown in chapter 1, a better knowledge of the neutrino mass is necessary to answer fundamental questions of particle and astroparticle physics and cosmology. A further reduction of the upper limit on the electron anti-neutrino mass cannot be expected by additional data from the existing experiments since the systematic uncertainties are dominating the total uncertainties of the experiments. Therefore the next generation tritium β decay experiment KATRIN (KARlsruhe TRITium Neutrino experiment) is currently being set up to increase the sensitivity on the electron anti-neutrino mass by one order of magnitude, i.e. from about $2 \text{ eV}/c^2$ to $200 \text{ meV}/c^2$. It comprises a super-luminous tritium source with a MAC-E filter and an energy resolution $\Delta E < 1 \text{ eV}$.

2.2 Description of main components of KATRIN

The KATRIN setup consists of several main components, shown in figure 2.4:

- The Rear Section that is attached to one end of the tritium source and is used for monitoring and calibration.
- The Windowless Gaseous Tritium Source (WGTS) which provides the electrons from tritium β decay. The WGTS consists of a source tube which is surrounded by a cryostat (WGTS cryostat) and of the tritium loops (Inner Loop) which are necessary for the stable injection of tritium into the source tube.
- The Transport Section adiabatically guides the electrons from the WGTS to the spectrometers and in parallel reduces the tritium flow rate by 14 orders of magnitude. It consists of two subsystems: The Differential Pumping Section (DPS2-F) and the Cryogenic Pumping Section (CPS).
- The MAC-E type Main Spectrometer and a smaller but similar Pre-Spectrometer that is placed in front of it. The Pre-Spectrometer is used for pre-filtering the β electrons while the actual energy measurement is done by the Main Spectrometer.
- The Detector Section at the end of the Main Spectrometer for counting the electrons that passed the spectrometers.

All tritium bearing components, i.e. the Rear Section, the WGTS and the Transport Section will be set up inside the Tritium Laboratory Karlsruhe that supplies the necessary infrastructure and expertise for safe tritium handling. In the following subsections, the main components of KATRIN will be briefly presented.

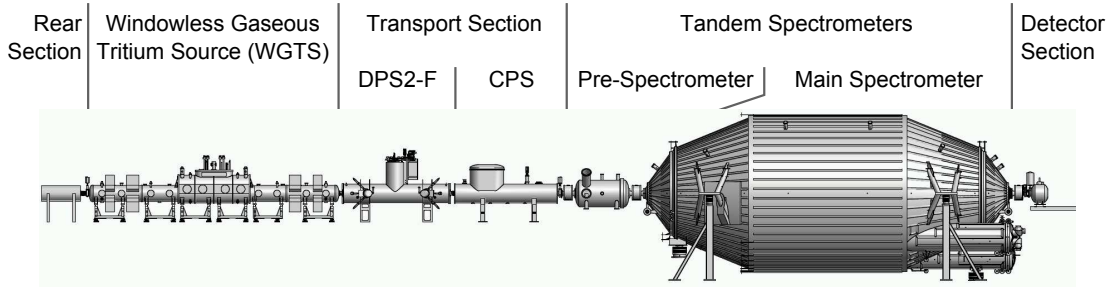


Figure 2.4: The main components of the KATRIN experiment. From left to right: The Rear Section for monitoring and calibration, the Windowless Gaseous Tritium Source (WGTS), the Transport Section consisting of the Differential Pumping Section (DPS2-F) and the Cryogenic Pumping Section (CPS), the Pre-Spectrometer and the Main Spectrometer forming the Tandem Spectrometers and the Detector Section. The KATRIN setup is in total about 70 m long.

2.2.1 The Windowless Gaseous Tritium Source (WGTS)

The windowless gaseous tritium source is a stable gas column of tritium molecules inside an about 10 m long source tube with 9 cm diameter. The tritium molecules are injected in the centre of the source and stream towards the ends of the source tube where they are pumped off by turbo molecular pumps. The β electrons formed in the source, in contrast, are not affected by the pumping because they are adiabatically guided by magnetic field lines towards the end of the source tube which is directly, i.e. *windowless*, connected to the Transport Section.

The number of tritium atoms inside the WGTS is given by

$$N(T_2) = \rho d \cdot A \cdot \varepsilon_T \quad (2.10)$$

where ρd is the column density, A the cross section of the source tube and ε_T the isotopic purity, i.e. the ratio of tritium atoms in the source to the total number of atoms. The column density is the areal density of atoms in the source.

The column density will be set to $\rho d = 5 \cdot 10^{17} \text{ cm}^{-2}$. A higher column density would in fact increase the activity of the source but also enhance the uncertainties due to systematic effects, e.g. scattering of β electrons with the gas in the source. In order to reach a column density of $5 \cdot 10^{17} \text{ cm}^{-2}$ in a tube with open ends, the temperature of the source has to be cooled down to 27-30 K to reduce the conductivity of the tube. A further reduction of the source tube temperature is not favourable since tritium molecules would start to cover the source tube walls and to form clusters. The column density has to be stabilised to 10^{-3} precision to reach the claimed sensitivity of $200 \text{ meV}/c^2$ on the anti-neutrino mass. This will be achieved by

- temperature stabilisation of the source tube to $\pm 30 \text{ mK}$ by the WGTS cryostat,
- a constant tritium injection rate of 1.853 mbar l/s which is achieved by a dedicated injection system, the so-called Inner Loop,
- a constant and high ($>95 \%$) isotopic purity of the tritium gas, also achieved by the Inner Loop and
- a constant tritium pumping rate at the ends of the source tube.

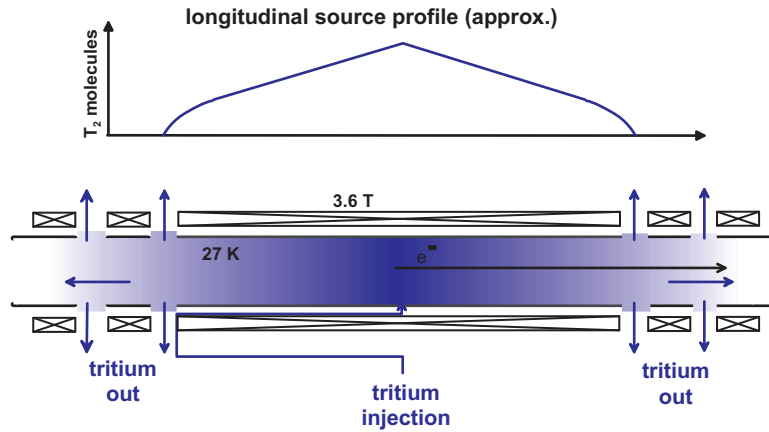


Figure 2.5: Schematic drawing of WGTS and tritium density profile along source tube. *Below:* Top view of cross section of the WGTS. The tritium gas is injected in the middle of the source tube and free streams towards the turbomolecular pumps at both ends. The β electrons are not affected by the pumping since they are guided by strong magnetic field lines towards the transport system on the right side. The positions of the superconducting magnets are indicated by the squares on both sides of the source tube. *Above:* The calculated shape of the density profile of tritium molecules along the source tube. Note that the density profile is not absolutely correct in the centre region and at the pump ports. [KAT05]

The expected gas density profile inside the source tube is shown in figure 2.5. The isotopic purity ε_T of the gas in the source has to be higher than 95 % and stabilised to 0.1 % which will be also achieved by the Inner Loop system. The necessity of a stabilisation and continuous monitoring of ε_T is addressed in section 2.3.

The Inner Loop is an integral part of the WGTS, it ensures the constant injection rate and the isotopic purity of the injection gas. The constant injection rate will be achieved by a pressure and temperature controlled buffer vessel that is connected to the WGTS by a capillary with known conductance (see simplified flow diagram in figure 2.6). The tritium gas that is pumped off at the ends of the WGTS will be cleaned from impurities, e.g. from methane and ^3He which is formed by tritium β decay, by a palladium membrane filter² and then reinserted into the pressure controlled buffer vessel. The tritium throughput in this closed loop system will be 40 g tritium per day. Tritium gas with an isotopic purity > 98 % can be inserted into the Inner Loop from the Isotope Separation System of TLK to compensate the continuous decrease of the isotopic purity due to β decay.

The WGTS cryostat (see figure 2.7) houses the source tube, the superconducting magnets around the source tube and the differential pumping sections at both ends of the source tube. The source tube is temperature stabilised to a precision of 30 mK using a custom made cooling system based on boiling neon [Gro09]. The beam tube, the vacuum and the cooling system were assembled to the so-called “demonstrator” which is used to experimentally verify the feasibility of the cooling concept. After the successful test of the demonstrator, the superconducting magnets and all other missing components will be installed and the demonstrator converted and upgraded to the WGTS cryostat.

²also called PERMCAT

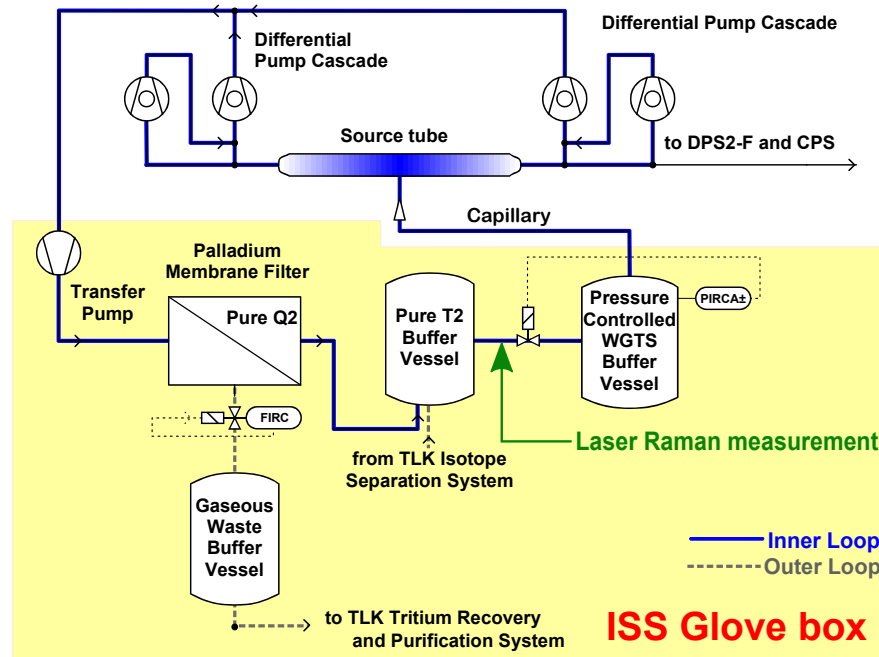


Figure 2.6: Simplified flow diagram of the KATRIN Inner Loop system

The source tube of the WGTS is fed via a capillary with known conductance from a pressure controlled buffer vessel. The pressure and temperature stabilisation of the pressure controlled buffer vessel ensures a constant injection rate of 1.853 mbar l/s tritium into the source. The tritium molecules freely stream towards both ends of the source tube where they are pumped off by turbomolecular pumps. The palladium membrane filter can be only passed by hydrogen isotopologues (H_2 , D_2 , T_2 , HT , DT , HD). The pure T_2 buffer vessel feeds the pressure controlled buffer vessel. The isotopic purity is monitored by a Laser Raman system at a pressure of $p \approx 130$ mbar. Gas that cannot pass the palladium membrane filter is processed by the TLK tritium recovery and purification system. Batches of pure tritium can be injected into the pure T_2 buffer vessel from the TLK isotope separation system (ISS) if necessary. The Inner Loop and all other tritium bearing components are housed in glove boxes for safety reasons. For further details see [Stu10b].

Current status of the WGTS

The demonstrator was delivered to KIT at 2010/04/08 (see figure 2.8) and is currently being commissioned. The Inner Loop system was successfully commissioned with non-radioactive gases in November 2009 and the stabilisation of the injection pressure was proven to be better than 0.02 % [Pri09], i.e. an overachievement of the design requirements by a factor of five. The Inner Loop will not be operated with tritium until it is connected to the WGTS cryostat.

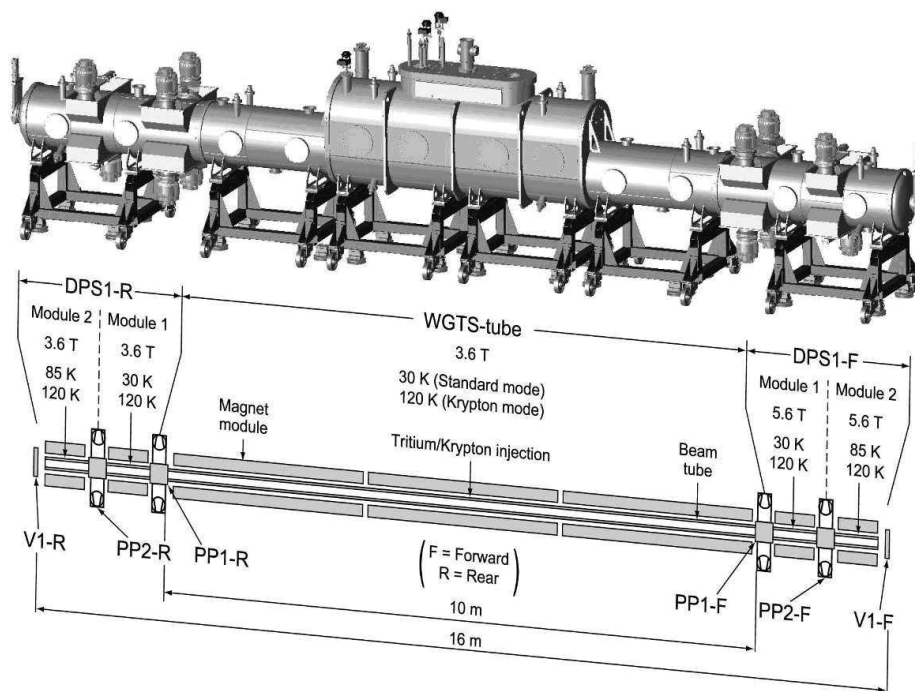


Figure 2.7: 3D model and schematic drawing of WGTS cryostat and source tube. The source tube is surrounded by superconducting magnets. The differential pumping sections DPS1-F and DPS1-R are connected to both ends of the source tube and for a first reduction of the tritium gas flow rate of about a factor of 10^2 . 3D model from company ACCEL



Figure 2.8: Delivery of the demonstrator to KIT. The demonstrator is the first step of the construction of the WGTS and was delivered to KIT at 2010/04/08. It will be used to prove the feasibility of the temperature stabilisation of the source tube to ± 30 mK.

2.2.2 The Transport Section

The transport section consists of the differential pumping section DPS2-F and the cryogenic pumping section CPS. It serves two purposes, (i) it has to adiabatically transport the electrons from the WGTS to the spectrometers by magnetic field lines that connect the WGTS and the Pre-Spectrometer and (ii) it has to reduce the tritium flow rate from the WGTS into the pre-spectrometer from about 1 mbar l/s to a level of less than 10^{-14} mbar l/s. By the suppression of tritium flow by 10^{14} the tritium partial pressure is reduced to 10^{-20} mbar in the main spectrometer to reach the goal of 1 mHz maximum background from tritium β decay in the main spectrometer. The tritium flow reduction is achieved by differential and cryogenic pumping of tritium:

Differential pumping in the DPS-F

In the DPS2-F the tritium flow rate is reduced by differential pumping using four turbomolecular pumps. The beam tube of the DPS2-F is cooled down to 77 K to reduce the conductance of the tube and hence enhance the pumping efficiency. Several bends of 20° in the beam tube (see figure 2.9) prevent neutral particles from flying straight through the DPS2-F. In total the tritium flow rate will be reduced by a factor of 10^5 by the DPS2-F.

Superconducting magnets with 5.6 T maximum field strength are placed around the beam tube and form the magnetic field lines for the adiabatical guiding of the β electrons from the WGTS to the CPS.

Cryogenic pumping in the CPS

After differential pumping the tritium flow rate will be further reduced by a factor of 10^7 to 10^{-14} mbar l/s by cryopumping of tritium molecules inside the CPS. For that purpose, the beam tube in the CPS is cooled down to 3 - 3.5 K and its surface is covered with argon frost for an enlargement of the surface area. The beam tube of the CPS is also bended several times similar to the DPS2-F. Tritium molecules that hit the beam tube walls will be trapped. This concept has been successfully proven by the dedicated test experiment TRAP (Tritium Argon frost Pump) at TLK [Stu07], [Eic08], [Eic09]. After a KATRIN run, the argon frost is removed by warming the beam tube to 100 K and simultaneously flushing with He gas from the spectrometer side towards the WGTS side. After a bake-out of the beam tube, the tube is cooled down to 6 K and a new layer of argon frost is deposited on the tube walls. In a final step the beam tube is cooled down to its operation temperature of 3 - 3.5 K.

Current status of the Transport Section

The DPS2-F was delivered to KIT on 2009/07/15 (see figure 2.9) and is beeing currently commissioned. The tests of the reduction factor and the transmission properties of the DPS2-F will be done until end of 2010. The CPS is currently being manufactured by ASG³ and shall be delivered in February 2011.

³ASG Superconductors, Genova, Italy

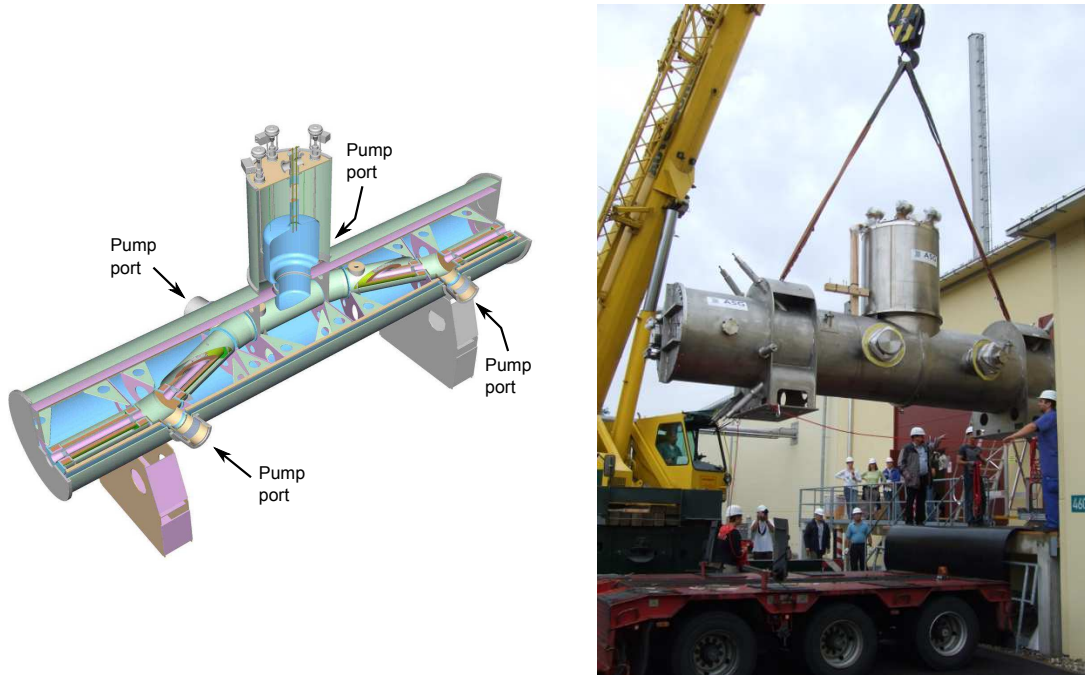


Figure 2.9: 3D drawing of DPS2-F with beam tube and picture from the arrival at KIT. *Left:* The beam tube makes four bends to prevent neutral particles from flying straight through the DPS2-F. The four turbomolecular pumps will be mounted on the pump ports outside of the cryostat. *Right:* The DPS2-F was delivered on 2009/07/15 and lifted into the KATRIN building.

2.2.3 The Tandem Spectrometers

Both spectrometers, the Pre- and the Main Spectrometer, are of MAC-E-type.

The Pre-Spectrometer is placed between the CPS and the Main Spectrometer. The Pre-Spectrometer will be set at a retarding potential of about 300 eV below the endpoint to reduce the electron flow rate into the Main Spectrometer from 10^{10} s^{-1} to 10^4 s^{-1} . The purpose of this reduction is to lower the number of electrons in the Main Spectrometer that contain no information on the neutrino mass. This reduces the background due to interaction of electrons with residual gas in the Main Spectrometer. The Pre-Spectrometer has an energy resolution of $\Delta E \approx 100 \text{ eV}$ which is sufficient for this first step of filtering.

The Main Spectrometer (see figure 2.10) is used for the precise measurement of the endpoint region of the tritium β spectrum. A superconducting solenoid with 4.5 T field strength is placed between main spectrometer and transport section, another with 6 T field strength between main spectrometer and detector system. The magnetic field strength decreases down to 0.3 mT in the centre of the spectrometer but the magnetic flux tube expands to 9 m diameter due to the conservation of magnetic flux. The energy resolution of the Main Spectrometer is $\Delta E = 0.93 \text{ eV}$ according to (2.5) for an electrostatic potential of $E \approx 18.6 \text{ keV}$ of the Main Spectrometer. The size of the Main Spectrometer is large (10 m diameter, 23.3 m length) to completely contain the expanding flux tube. The electrostatic retarding potential is formed by the inner electrode system [Hug08] [Zac09] [Pra10], that consists of two layers of wire electrodes which are mounted on the inner walls of the spectrometer. Two additional air coil



Figure 2.10: The Main Spectrometer surrounded by the support structure for the external air coil systems. The Pre-Spectrometer and the CPS will be installed directly in front of the Main Spectrometer.

systems are mounted around the main spectrometer: The Earth's Magnetic Field Compensation System (EMCS) is installed to compensate the earth magnetic field which cannot be neglected in the centre region of the main spectrometer [Rei09b]. The Low Field Correction System (LFCS) is used for fine tuning of the magnetic flux tube in the Main Spectrometer [Wan09].

Current status of the Tandem Spectrometers

The Pre-Spectrometer has been tested and used as a stand-alone prototype for the development and detailed understanding of the Main Spectrometer and the electron detector [Wue10] and will be moved to its final position in autumn 2010. The vessel of the Main Spectrometer was delivered to KIT in 2006 and the installation of the inner electrode system in the Main Spectrometer is currently ongoing.

2.2.4 The Detector Section

Electrons with high enough longitudinal energy can pass the retarding electrostatic barriers of the spectrometers and are afterwards guided by the magnetic field lines to the detector system. The detector is placed in a $B=3$ T superconducting magnet that reduces the diameter of the magnetic flux tube from 9 m (in the analysis plane of the main spectrometer) to about 9 cm. The detector itself is a segmented PIN-diode array. The position information provided by the detector segmentation can be used to study inhomogeneities and asymmetries in the transport section and in the spectrometers. During normal tritium runs, the expected count rate varies from a few

to several hundred mHz depending on the retarding voltage of the main spectrometer. The detector background is reduced below 1 mHz by passive and active shielding of the detector. The time precision of the detector $\delta t < 500$ ns is short enough to handle also high count rates up to 1 MHz during measurements with the electron gun of the rear section.

Current status of the Detector Section

The detector system is currently being commissioned at the University of Washington and will be shipped to KIT in summer 2010.

2.2.5 The Rear Section

The Rear Section is located at the rear side of the Wand is used for calibration and monitoring purposes:

- A rear wall closes the WGTS and is used to define the electrostatic potential of the WGTS relative to the spectrometers.
- A continuous monitoring of the source activity can be accomplished by a measurement of the β electron rate on the rear wall. A second alternative measurement technique was investigated [Mau09] to monitor the source activity by the detection of bremsstrahlung which is produced by β electrons in the rear wall.
- The column density can be monitored periodically by the measurement of the energy loss spectrum of monoenergetic electrons ($\delta E < 0.2$ eV at 18.6 keV [Leb10]). The electrons are emitted by an electron source in the Rear Section, enter the WGTS through a hole in the rear wall, pass the Transport Section and are analysed by the spectrometers and the detector. The electron source can be also used for further characterisation measurements of KATRIN.

Current status of the Rear Section

A technical design based on the above mentioned tasks is currently being developed.

2.3 Necessity of Laser Raman measurements for KATRIN

The β activity dN/dt of the source is proportional to the total number of tritium atoms in the source given by (2.10), and hence proportional to the column density ϱd and the tritium purity ε_T .

$$dN/dt \propto \varrho d \cdot \varepsilon_T \quad (2.11)$$

The parameters ϱd and ε_T have to be stabilised and monitored since any fluctuation of dN/dt would directly affect the count rate of the detector system and thus the β spectrum.

A Laser Raman system was developed to monitor the composition of the tritium gas and therefore also the parameter ε_T just before entering the WGTS. The measurement of the gas composition by the Laser Raman system will be also used to estimate the

influence of other effects on the β spectrum, namely the Doppler effect, the nuclear recoil and the elastic e^- - T_2 scattering which will be briefly discussed now.

Doppler Broadening

The energy of the β electrons is smeared due to the statistical motion of the tritium molecules and has to be taken into account in the analysis of the β spectrum. The energy smearing ΔE is given by

$$\Delta E \approx m \cdot v_e \cdot v_{\text{mol}} \quad (2.12)$$

[KAT05] where m and v_e are the the mass and the speed of the β electron and v_{mol} the velocity component of the decaying molecule in the direction of the emitted electron. The velocity v_{mol} is in first order given by the Maxwell-Boltzmann distribution and hence by the temperature of the gas and the mass of the molecule. For $T=30$ K, $m = 9.11 \cdot 10^{-31}$ kg and $v_e = 8 \cdot 10^7$ m/s the smearing ΔE for T_2 (DT) is 148 meV (162 meV).

Elastic e^- - T_2 scattering

Electrons can scatter also elastically on gas molecules besides the already mentioned inelastic scattering. The energy loss ΔE of an electron with initial energy E and mass m_e due to the elastic scattering is given by

$$\Delta E = 2 \frac{m_e}{m_{\text{mol}}} E (1 - \cos \theta_s). \quad (2.13)$$

ΔE depends on the scattering angle θ_s and on the mass m_{mol} of the involved gas molecule. The scattering is very forward peaked since the mean scattering angle is about 3° , the maximum energy loss is of the order of several eV but the average energy loss is only 16 meV for T_2 [KAT05]. The energy loss due to an elastic scattering with another type of hydrogen isotopologue than T_2 (e.g. HT) increases up to a factor of 6 due to the large relative differences of molecular masses.

Nuclear recoil

In the theoretical treatment of the molecular tritium decay $T_2 \rightarrow ({}^3\text{HeT})^+ + e^- + \bar{\nu}_e$ the recoil of the daughter molecule $({}^3\text{HeT})^+$ cannot be neglected. For electron energies E close to the endpoint, the recoil energy E_{rec} of the daughter molecule with mass m_{mol} is given by [KAT05]

$$E_{\text{rec}} \approx E \cdot \frac{m_e}{m_{\text{mol}}} \quad (2.14)$$

The effect of a non-vanishing recoil energy is a corresponding shift of the endpoint energy of the β spectrum to lower energies. Although T_2 will be the most dominant constituent of the gas in the source also HT and DT molecules will be present at concentrations of a few percent or less. The observed β spectrum of KATRIN will be therefore a superposition of the β spectra of T_2 , HT and DT which have different endpoint energies due to (2.14) and the different masses of the corresponding daughter molecules $({}^3\text{HeH})^+$ and $({}^3\text{HeD})^+$.

The projected total systematic uncertainty of KATRIN on the observable m_ν^2 [KAT05] is

$$\sigma_{\text{syst}} \leq 0.017 \text{ eV}^2/c^4. \quad (2.15)$$

The expected statistical uncertainty on m_ν^2 after tree years of full measurement time

$$\sigma_{\text{stat}} = 0.018 \text{ eV}^2/c^4 \quad (2.16)$$

is comparable to the total systematic uncertainty σ_{syst} . Adding both uncertainties quadratically leads to a total uncertainty of

$$\sigma_{\text{tot}} \leq 0.025 \text{ eV}^2/c^4. \quad (2.17)$$

From this a discovery potential of

$$m_\nu = 0.35 \text{ eV}/c^2 \quad (2.18)$$

can be deduced for a neutrino mass detection with 5σ significance [KAT05]. But if the observed β spectrum is compatible with $m_\nu = 0$ KATRIN will be able to state a new upper limit (90 % C.L.) on m_ν of

$$m_\nu \leq 0.2 \text{ eV}/c^2. \quad (2.19)$$

It has been shown in the beginning of this section that the gas composition in the source has an influence on systematic effects and hence on the sensitivity of the neutrino mass determination by KATRIN. To reach the claimed total systematic uncertainty of $\sigma_{\text{syst}} \leq 0.017 \text{ eV}^2/c^4$ the tritium purity has to be continuously monitored with 10^{-3} precision (1σ). Laser Raman spectroscopy is the method of choice because it is an inline and almost real time measurement technique, i.e. no gas samples have to be taken, and all hydrogen isotopologues can be identified and monitored simultaneously within a period of typically 250 s which will be a typical measurement intervall in KATRIN neutrino mass measurement runs.

In the next chapter the theoretical fundamentals will be presented which are necessary for the understanding of Laser Raman spectroscopy. The experimental setup of a Laser Raman system will be presented in chapter 4 while chapter 5 will address the stability of the Laser Raman system. In chapter 6 a set of measurements will be presented that were conducted to determine molecular constants of tritium and other hydrogen isotopologues which are currently not sufficiently known. These constants are necessary for the prediction of line intensities in Raman spectra and hence for the determination of the gas composition from the Raman spectrum.

Chapter 3

The Raman effect

In this chapter the theoretical background of the Raman effect and Raman spectroscopy will be presented. After a general description of the Raman effect in the introduction of this chapter, the excitation levels of diatomic molecules and typical features of Raman spectra of hydrogen isotopologues are discussed in section 3.1. The line strength function is introduced to account for the influence of the polarisability of molecules on line intensities in Raman spectra. In section 3.2 an overview of the calculations of the polarisability of molecules is given and it is shown that a dedicated measurement of the polarisability of the tritiated hydrogen molecules is necessary for KATRIN. A suitable method is presented in section 3.3.

The Raman effect describes inelastic scattering of a photon on a molecule. The scattering process causes a transition between states of the molecule: The molecule makes a transition from an initial state $|i\rangle$ via a virtual state $|r\rangle$ to the final state $|f\rangle$. Accordingly, the energy of the photon and therefore its wavelength have to change in order to fulfil energy conservation. In case of the so-called Stokes Raman scattering, the wavelength of the scattered light increases and the molecule is excited to a more energetic state. In case of Anti-Stokes Raman scattering, the molecule is already in an excited state and de-excites to a less energetic state. In this case the wavelength of the scattered light is decreased in comparison to the incident light. It is important to note that the energy levels in molecules are in general quantised. Therefore, only certain, molecular specific wavelength shifts of the light are possible during Raman scattering. In figure 3.1 the transitions between molecular states are illustrated for both cases of Raman scattering and additionally for Rayleigh scattering, i.e. elastic scattering of light on molecules. In that case the initial and the final state are identical and the wavelength of the scattered light is not shifted.

Raman spectroscopy is a method to investigate the structure of molecular energy states by the spectrum of the Raman scattered light. For that purpose the sample is irradiated by a monochromatic light source, typically a laser, and the spectrum of the scattered light is measured as shown in figure 3.2. A drawback of Raman spectroscopy is the low intensity of the Raman scattered light due to the small cross-section for Raman scattering which is for gases typically of the order of 10^{-30} cm² [Men07]. Therefore, lasers are used as typical light sources for Raman spectroscopy since they offer high intensities with well defined wavelength. Additionally the scattered light can be collected in a 90° geometry to reduce the collection of the intense laser light.

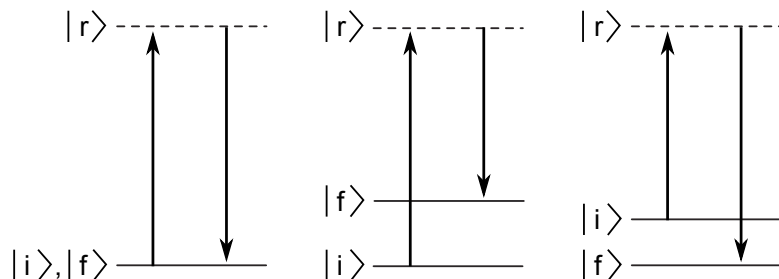


Figure 3.1: Quantum mechanical picture of Rayleigh and non-resonant Raman scattering. In all types of scattering a virtual state $|r\rangle$ is involved. *Left:* Rayleigh scattering. The initial state $|i\rangle$ and final state $|f\rangle$ are identical. In Raman scattering, the initial state $|i\rangle$ and the final state $|f\rangle$ have different energy levels $E_i = \langle i|E|i\rangle$ and $E_f = \langle f|E|f\rangle$. *Middle:* Stokes Raman scattering. $E_i < E_f$. *Right:* Anti-Stokes Raman scattering. The molecule is in an excited state before scattering and $E_i > E_f$. (According to [Lon02])

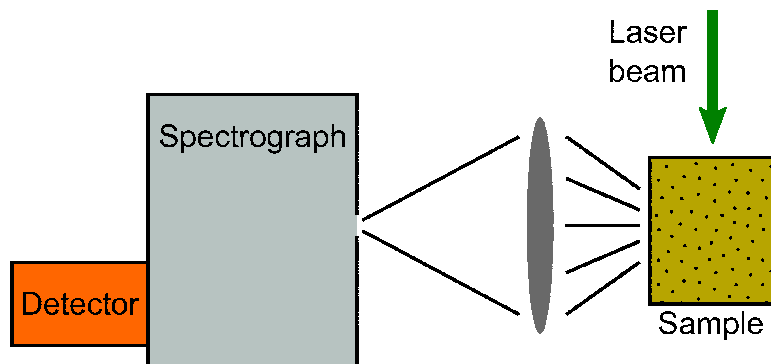


Figure 3.2: Schematic drawing of a setup for Raman spectroscopy. Monochromatic laser light is scattered in the sample and the scattered light is sent to a spectrograph. The spectrograph decomposes the light into spectral lines that are recorded by a light sensitive detector. (According to [Hak06])

In the field of spectroscopy the variable wavenumber $\tilde{\nu}$ is usually used instead of wavelength λ or frequency ν

$$\tilde{\nu} = \frac{1}{\lambda} = \frac{\nu}{c} = \frac{\text{Energy}}{hc} \text{ [cm}^{-1}\text{]} \quad (3.1)$$

where c is the speed of light. Wavenumbers are used to describe wavelength shifts of the light in Raman scattering since this representation allows to directly compare spectra even when they were measured with excitation sources with different wavelengths. Simultaneously, wavenumbers are used to specify spacings in between energy levels of a molecule.

3.1 Excitation of diatomic molecules

In this section the excited states of diatomic molecules will be presented that are relevant for standard Raman spectroscopy, i.e. vibrational and rotational excitations. Electronic excitations will be ignored since they are only relevant for advanced spectroscopic methods like Resonance Raman Spectroscopy. The following treatment of vibrational and rotational excitations is based on [Hak06] and [Lon02].

3.1.1 Rotational excitation

The most simple model for the description of rotations of diatomic molecules around their centre of mass approximates the molecule as a rigid-rotator: Two atoms with fixed separation R and mass m_1 and m_2 respectively (see figure 3.3). The rotational energy of a molecule rotating with angular frequency ω is given by

$$E_{\text{rot}} = \frac{1}{2}I\omega^2 \quad (3.2)$$

where $I = \mu R^2$ is the moment of inertia of the molecule and $\mu = \frac{m_1 m_2}{m_1 + m_2}$ the reduced mass of the molecule. The absolute value of the angular momentum is given by

$$|\mathbf{L}| = L = I\omega \quad (3.3)$$

Hence the rotational energy can be rewritten in terms of L and I

$$E_{\text{rot}} = \frac{L^2}{2I} \quad (3.4)$$

Using the quantisation of angular momentum according to the orbital angular momentum of the hydrogen atom

$$L = \hbar\sqrt{J(J+1)} \quad \text{with } J = 0, 1, 2, \dots \quad (3.5)$$

where J is the rotational quantum number, the rotational energy can be expressed in terms of J and I

$$E_{\text{rot}}(J) = \frac{\hbar^2}{2I}J(J+1) \quad (3.6)$$

In spectroscopy energy levels are normally given in wavenumbers, denoted by

$$F(J) = \frac{E_{\text{rot}}(J)}{hc} = BJ(J+1) \quad (3.7)$$

where

$$B = \frac{h}{8\pi^2 c I} \quad (3.8)$$

is a constant that is characteristic for the type of molecule. The selection rule for rotational excitations in Raman spectra is $\Delta J = \pm 2$ due to its nature as a two photon process. Hence, the wavenumber shift from a transition from an initial state with quantum number J to a state with quantum number $J+2$ is given by

$$F(J+2) - F(J) = B(4J+6). \quad (3.9)$$

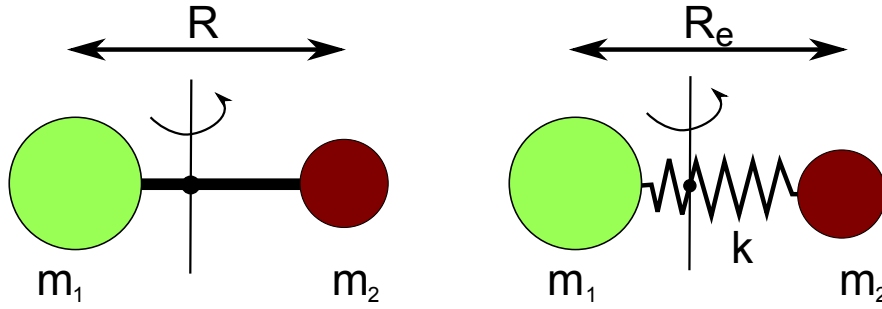


Figure 3.3: Rigid and non-rigid rotator model of a hetero-nuclear molecule with atomic masses m_1 and m_2 . The molecule rotates around its centre of mass. *Left:* The internuclear distance R is fixed in the rigid rotator model. *Right:* In the non-rigid rotator model the atoms are connected by a “spring” with spring constant k and equilibrium distance R_e .

This means that the first rotational line ($J = 0 \rightarrow 2$) has a wavenumber shift of $6B$ from the wavenumber of the initial radiation. All other lines are equally spaced with $4B$ distance.

In Raman spectra with sufficient resolution it can be seen that the rotational lines are not equally separated for higher values of J . This can be described by the non-rigid rotator model which additionally takes into account that the internuclear distance R increases for higher rotational states due to the centrifugal force. In this model, the solid connection between the two atoms is replaced by a spring with spring constant k . The centrifugal force on the atoms is set equal to the force of the “spring”

$$m_r R \omega^2 = k(R - R_e) \quad (3.10)$$

where R_e is the internuclear distance at rest. Assuming small elongations of the spring, i.e. $\frac{R - R_e}{R_e} \ll 1$, and using the same quantisation of the angular momentum as before one gets

$$F(J) = \frac{E_{\text{rot}}(J)}{hc} = BJ(J+1) - DJ^2(J+1)^2 \quad (3.11)$$

with a second molecule specific constant

$$D = \frac{\hbar^3}{4\pi k I^2 R_e^2 c}. \quad (3.12)$$

In case of hydrogen isotopologues the D/B ratio varies from $2 \cdot 10^{-4}$ to $8 \cdot 10^{-4}$ [Edw78]. The effect of the anharmonicity correction $DJ^2(J+1)^2$ is a decreasing separation of the rotational lines for increasing J values. For special applications the expression (3.11) can be further extended to higher order corrections to match high resolution spectra at large J values.

3.1.2 Vibrational excitation

Different models are available for the description of vibrations of molecules. Similar to the models of rotational excitations, the choice of model depends on the desired precision and the resolution of the available experimental spectra. The most simple model is the harmonic approximation that uses the same assumptions as the non-rigid

rotator model: A “spring” with spring constant k connects the two atoms and the potential V due to the spring is given by

$$V = \frac{k}{2}(R - R_e)^2 \quad (3.13)$$

The quantum mechanical calculation of such a harmonic oscillator with reduced mass μ and resonance frequency $\omega = \sqrt{\frac{k}{\mu}}$ can be found in most textbooks of quantum mechanics, e.g. in [Hak04]. The energy levels are given by

$$E_{\text{vib}} = \hbar\omega\left(v + \frac{1}{2}\right) \quad \text{with } v = 0, 1, 2, \dots \quad (3.14)$$

where a new quantum number v was introduced. In wavenumbers the energy states are denoted by

$$G_v = \frac{E_{\text{vib}}}{hc} = \tilde{\nu}_e\left(v + \frac{1}{2}\right) \quad (3.15)$$

with

$$\tilde{\nu}_e = \frac{1}{2\pi c} \sqrt{\frac{k}{\mu}}. \quad (3.16)$$

The selection rule for vibrational Raman transitions is $\Delta v = \pm 1$.¹ The wavenumber shift

$$G_{v+1} - G_v = \tilde{\nu}_e \quad (3.17)$$

is independent of v . The parabolic potential is only the simplest approximation of the molecular potential close to its minimum. A parabolic cannot account for the repulsive behaviour towards $R=0$ and does not correctly describe the dissociation of the molecule at finite energy for $R \rightarrow \infty$. A frequently used model potential is the so-called (empirical) Morse potential

$$V = D_e \left[1 - e^{-a(R-R_e)}\right]^2 \quad (3.18)$$

can be used. D_e is the dissociation energy of the molecule and $a = \tilde{\nu}_e \sqrt{\frac{\mu}{2D_e}}$.

The Morse potential (see figure 3.4) deviates only slightly from the parabolic potential of the harmonic oscillator as long the internuclear distance R is close to its equilibrium value R_e . For $R_e \rightarrow \infty$ the potential converges to the dissociation energy D_e of the molecule. The validity of the model is limited for $R \rightarrow 0$ since the potential rises to infinity without taking short ranged forces into account. Other, more accurate types of potential are used if high-precision (spectroscopic) information is required, and with the advancement of computing capabilities, rather accurate *ab initio* quantum calculations are now feasible for selected molecules.

Solving the Schrödinger equation for $R > R_e$ yields the vibrational energy levels of the molecule

$$E_\nu = \hbar\omega_e \left(v + \frac{1}{2}\right) - x_e \hbar\omega_e \left(v + \frac{1}{2}\right)^2 \quad (3.19)$$

¹Transitions with larger changes of v are also possible due to deviations of the potential from the assumed harmonic potential but are increasingly suppressed. A more realistic potential will be discussed in the next paragraph.

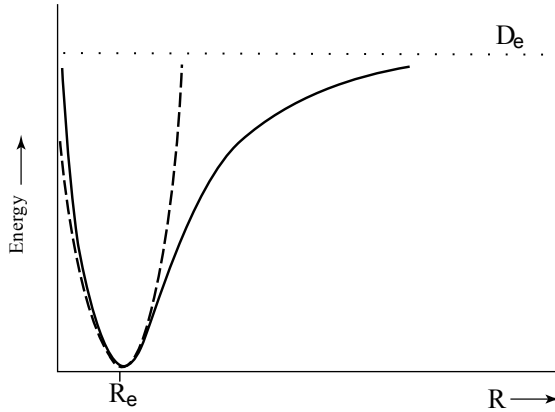


Figure 3.4: Sketch of the Morse potential (solid line) and harmonic potential (dashed line). The dissociation energy D_e of the Morse potential is indicated by the dotted line. (According to [Lon02])

and

$$G_v = \tilde{\nu}_e \left(v + \frac{1}{2} \right) - x_e \tilde{\nu}_e \left(v + \frac{1}{2} \right)^2 \quad (3.20)$$

respectively [Hak06]. The constant x_e defines the anharmonicity of the model and is typically of the order 0.01. The spacing between two neighbored vibrational states decreases with increasing quantum number v

$$G_{v+1} - G_v = \tilde{\nu}_e (1 - 2x_e(v + 1)) \quad (3.21)$$

which is also indicated in figure 3.5. This can explain the mentioned observation of multiple nearby vibrational lines in high resolution spectra. The anharmonicity further causes a weakening of the selection rule $\Delta v = \pm 1$, i.e. also transitions with larger changes of v are also allowed but suppressed in comparison to the main transition $\Delta v = \pm 1$.

Up to now, the rotational and vibrational excitations were considered separately, but it has to be taken into account that both types of excitation influence each other. A vibrational transition changes the mean internuclear distance of the molecule and hence the moment of inertia I which in turn determines the rotational energy levels according to (3.8), (3.11) and (3.12). To include this interaction into the theoretical description, the molecular specific constants B and D of the rotational energy states become a function of the vibrational quantum number v .

$$B \rightarrow B_v \quad (3.22)$$

$$D \rightarrow D_v \quad (3.23)$$

Further details will not be given here but can be found in [Hak06] and [Lew07].

In this section, the wavenumbers of vibrational and rotational transitions in a molecule were calculated using the molecule specific constants B_v , D_v , D_e , $\tilde{\nu}_e$ and x_e . Due to the already mentioned selection rules not all rotational and vibrational transitions are actually allowed and therefore only certain lines can be observed in Raman spectra. For hydrogen isotopologues and diatomic molecules in general, the vibrational quantum number changes by $\Delta v = 0, \pm 1$. The selection rule for rotational transitions

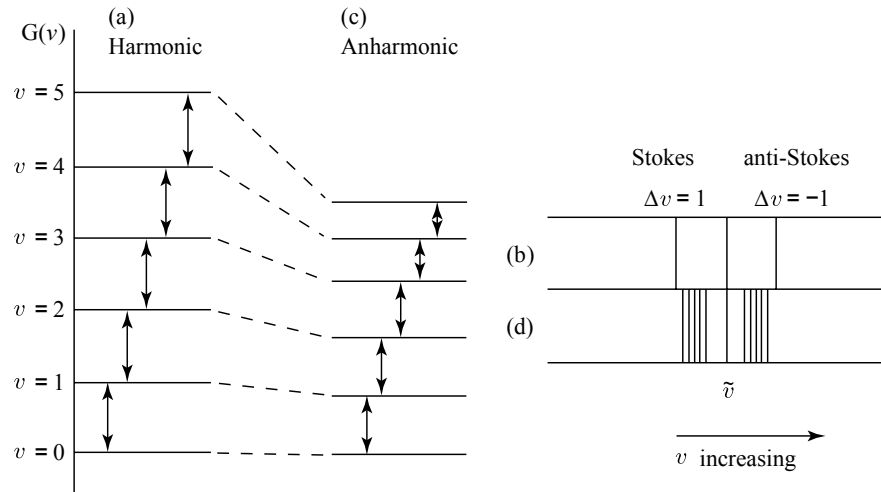


Figure 3.5: Energy levels of the harmonic (a) and anharmonic (c) oscillator. The anharmonic oscillator uses the Morse potential instead of a harmonic potential. (b) Due to the equally spaced energy levels of the harmonic oscillator only one Stokes and one anti-Stokes line is visible in the spectrum besides the line of the incident radiation (wavenumber $\tilde{\nu}$). (d) In case of the anharmonic oscillator, several vibrational lines are visible in the spectrum. The anharmonicity of (c) and (d) is drawn exaggeratedly, i.e. for a positive and large x_e . (According to [Lon02])

is $\Delta J = 0, \pm 2$. Table 3.1 shows a summary of allowed Raman transitions and the nomenclature that is used in this thesis.

The wavenumber shifts of rotational transitions are small in comparison to vibrational transitions. Therefore, the Rayleigh line and every vibrational line in a Raman spectrum is surrounded on both sides by a rotational lines, illustrated in figure 3.6.

The line positions in Raman spectra of all hydrogen isotopologues were calculated by R. Lewis in [Lew07] and are plotted in figure 3.7.

Table 3.1: Classification of transitions by selection rules. The selection rules for vibrational and rotational transitions are in general $\Delta v = 0, \pm 1$ and $\Delta J = 0, \pm 2$. Anti-Stokes Raman with $\Delta v = -1$ is not considered in this table because it is not relevant for this thesis. Each type of transition has a branch name, based on [Lon02] and [Lew07], that consists of a capital letter denoting ΔJ and a subscript number denoting Δv . In the last column, the corresponding wavenumber shifts of the transitions can be found.

Scattering process	Selection rules		Branch name	Raman shift
	Δv	ΔJ		
Rayleigh	0	0	Q_0	-
Stokes Raman (pure rotation)	0	+2	S_0	$\tilde{\nu}_p - \tilde{\nu}_{\text{rot}}$
Stokes Raman (rotation-vibration)	1	-2	O_1	$\tilde{\nu}_p - \tilde{\nu}_{\text{vib}} + \tilde{\nu}_{\text{rot}}$
	1	0	Q_1	$\tilde{\nu}_p - \tilde{\nu}_{\text{vib}}$
	1	+2	S_1	$\tilde{\nu}_p - \tilde{\nu}_{\text{vib}} - \tilde{\nu}_{\text{rot}}$

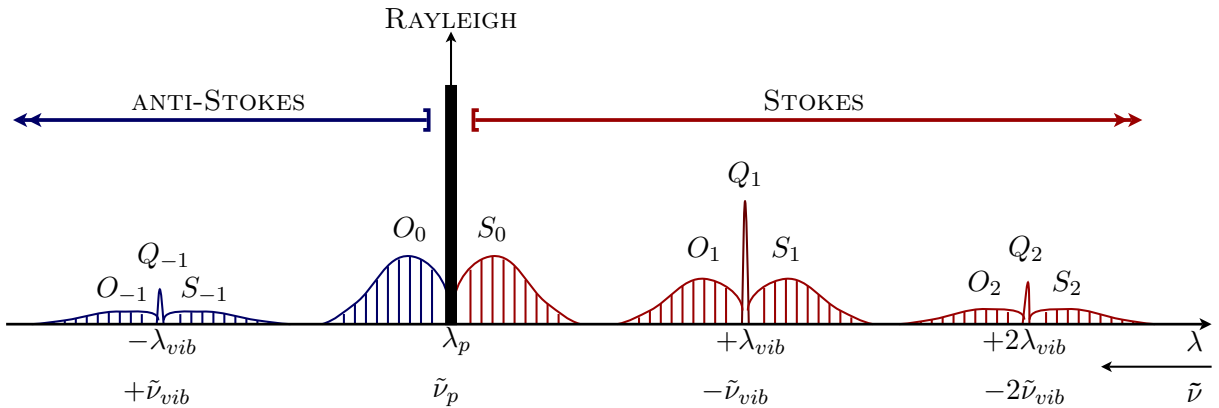


Figure 3.6: Typical Raman-spectrum of a diatomic molecule. The wavelength axis goes from left to right, the equivalent wavenumber axis goes from right to left. The black line indicates the Rayleigh line at the primary (laser) wavenumber $\tilde{\nu}_p$ which is surrounded by pure rotational lines: The S_0 -branch belongs to $\Delta J = +2$, the O_0 -branch to $\Delta J = -2$. The Q branches also contain several nearby lines which cannot be seen in this figure due to the insufficient resolution. Besides the line positions also the line intensities are qualitatively shown in the spectrum. A detailed discussion of line intensities is given in subsection 3.1.3. (According to [Hak06])

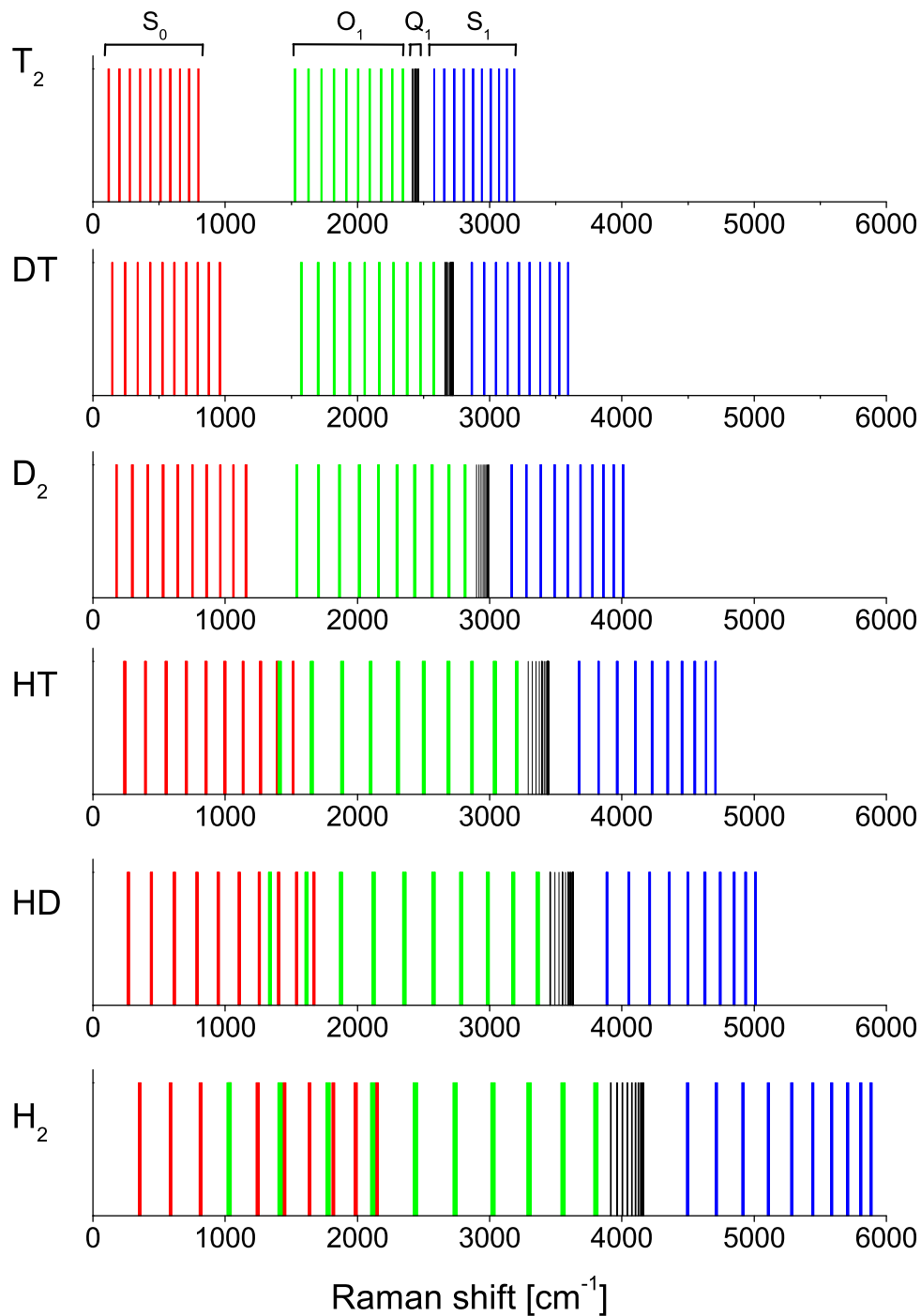


Figure 3.7: Line positions in Stokes part of Raman spectra of all hydrogen isotopologues. The position of the first 10 lines are given in Raman shifts, i.e. wavenumber shifts relative to the wavenumber of the excitation light. Each spectrum consists of 4 branches with increasing Raman shifts: The S_0 branch (red) with $\Delta v = 0$ and $\Delta J = 2$, the O_1 branch (green) with $\Delta v = 1$ and $\Delta J = -2$, the Q_1 branch (black) with $\Delta v = 1$ and $\Delta J = 0$ and the S_1 branch (blue) with $\Delta v = 1$ and $\Delta J = +2$. The separation of the rotational lines becomes larger with decreasing reduced mass which causes overlaps of the different branches. Line positions based on [Lew07].

3.1.3 Line intensities

The up to now presented models can only be used to calculate line positions but not line intensities. The calculation of line intensities is crucial for the KATRIN experiment because the gas composition of the inlet gas will be extracted from the line intensities in the measured Raman spectra. For the calculation of line positions *and* intensities a quantum mechanical model is needed. Before the fundamental equation of this model will be stated in (3.28), a few preliminary notes shall be given to motivate certain terms in it.

The scattering of light on a molecule can be described by an interaction of the incident light with the molecule. The intensity I of the scattered light is connected to the irradiance \mathcal{I} of the incident light by the interaction cross section ϱ .

$$I = \varrho \cdot \mathcal{I} \quad (3.24)$$

Classically, an oscillating electrical dipole moment \vec{p} is induced when the molecule is irradiated by light. The dipole moment is typically approximated by

$$\vec{p} = \boldsymbol{\alpha} \cdot \vec{\mathcal{E}} \quad (3.25)$$

where $\boldsymbol{\alpha}$ is a second rank tensor, called polarisability tensor and $\vec{\mathcal{E}}$ the electric field vector of the incident light. The oscillating dipole moment in turn is a source of radiation and emits light, the scattered light. The intensity I of the scattered light is in good approximation typically proportional to the square of the dipole moment \vec{p} and to the forth power of the wavenumber $\tilde{\nu}_s$ of the scattered light

$$\begin{aligned} I &= k'_{\tilde{\nu}} \tilde{\nu}_s^4 \cdot \vec{p}^2 \sin^2 \theta \\ &= k'_{\tilde{\nu}} \tilde{\nu}_s^4 \cdot (\boldsymbol{\alpha} \cdot \vec{\mathcal{E}})^2 \sin^2 \theta. \end{aligned} \quad (3.26)$$

where

$$k'_{\tilde{\nu}} = \frac{\pi^2 c}{2 \varepsilon_0} \quad (3.27)$$

and θ is the angle between the axis of the dipole and the direction of emittance [Lon02].

It can be expected from (3.24) and (3.26) that (i) the quantum mechanical expression for the intensity of the scattered light has the general structure of (3.24) and (ii) the cross section σ contains the $\tilde{\nu}_s^4$ term and a quantum mechanical equivalent to the polarisability tensor $\boldsymbol{\alpha}$ since the classical and the quantum mechanical description should have an analogue structure.

The quantum mechanical description of Raman scattering that can describe line positions and intensities uses quantum mechanics for the description of the molecular states but treats the light classically². The intensity I of the Raman scattered light with polarisation p^s from a population of diatomic molecules can be expressed by [Lon02]

$$I(\Theta, p^s, p^i) = k_{\tilde{\nu}} \cdot \tilde{\nu}_s^4 \cdot N_i \cdot \mathcal{I} \cdot \Phi(a^2, \gamma^2, \Theta, p^s, p^i). \quad (3.28)$$

$I(\Theta, p^s, p^i)$ depends on the polarization of the incident light denoted by p^i and on the geometry of the scattering process which is described by scattering angles and apertures. These geometrical parameters are represented by the collective variable Θ .

²A complete quantum mechanical description of molecular states and light gives in the end actually the same results [Lon02].

The other variables are:

$\tilde{\nu}_s$ The wavenumber of the scattered light which appears in the forth power.

N_i The number of molecules in the initial state i of the Raman transition. It can be calculated using the Boltzmann statistics

$$N_i = \frac{N g_i e^{-\frac{E_i}{kT}}}{Q} \quad (3.29)$$

where N is the total number of molecules, g_i the statistical weight, E_i the energy of the initial rotational and vibrational state, kT the thermal energy and $Q = \sum_j g_j \exp(-E_j/kT)$ the partition function. Further details are discussed in subsection 3.1.4.

\mathcal{I} The irradiance of the incident light.

$k_{\tilde{\nu}}$ A constant

$$k_{\tilde{\nu}} = \frac{\pi^2}{\varepsilon_0^2} \approx 1.259 \cdot 10^{23} \text{F}^{-2} \text{m}^2 \quad (3.30)$$

which is given in units of m^2 per Farad².

$\Phi(\mathbf{a}^2, \gamma^2, \Theta, \mathbf{p}^s, \mathbf{p}^i)$ The line strength function³ $\Phi(\mathbf{a}^2, \gamma^2, \Theta, \mathbf{p}^s, \mathbf{p}^i)$ contains molecule specific information, given by the parameters \mathbf{a}^2 and γ^2 , which will be discussed in subsection 3.1.5. It also depends on the geometry Θ of the experiment and on the polarisation state of the incident and scattered light.

3.1.4 Population factor for hydrogen isotopologues

In this subsection, the influence of the population factor N_i on equation (3.28) is discussed in detail for the case of hydrogen isotopologues.

The population factor N_i is, according to equation (3.29), a function of temperature and depends on the energy levels E_i of the molecule which can be calculated using the models from subsection 3.1.1 and subsection 3.1.2. The statistical weight g_i is constant for the hetero-nuclear molecules HD, DT and HT. In case of the homo-nuclear molecules the statistical weight varies with the rotational quantum number J due to the nuclear spins of the nuclei and the Pauli exclusion principle. For T_2 and H_2 the statistical weight for odd numbers of J is three times larger than for even numbers of J while the ratio is 1:2 for D_2 [Her39]. The difference is due to the fact that the deuteron has nuclear spin 1 but the hydrogen and tritium atoms have nuclear spin 1/2.

The exponential function in (3.29) has different consequences for the intensity distribution of the vibrational and rotational lines. At room temperature almost exclusively the vibrational ground level is populated due to the large energy difference between the ground state and the first excited vibrational state in comparison to the thermal energy kT . As mentioned before, the rotational energy states are much less separated than

³In earlier works, e.g. [Lew07], [Sch09], the dependence of the line strength function Φ on the polarisation of the incident and scattered light was not explicitly indicated since these parameters were normally fixed. In this work the polarisations play a mayor role and are therefore explicitly indicated.

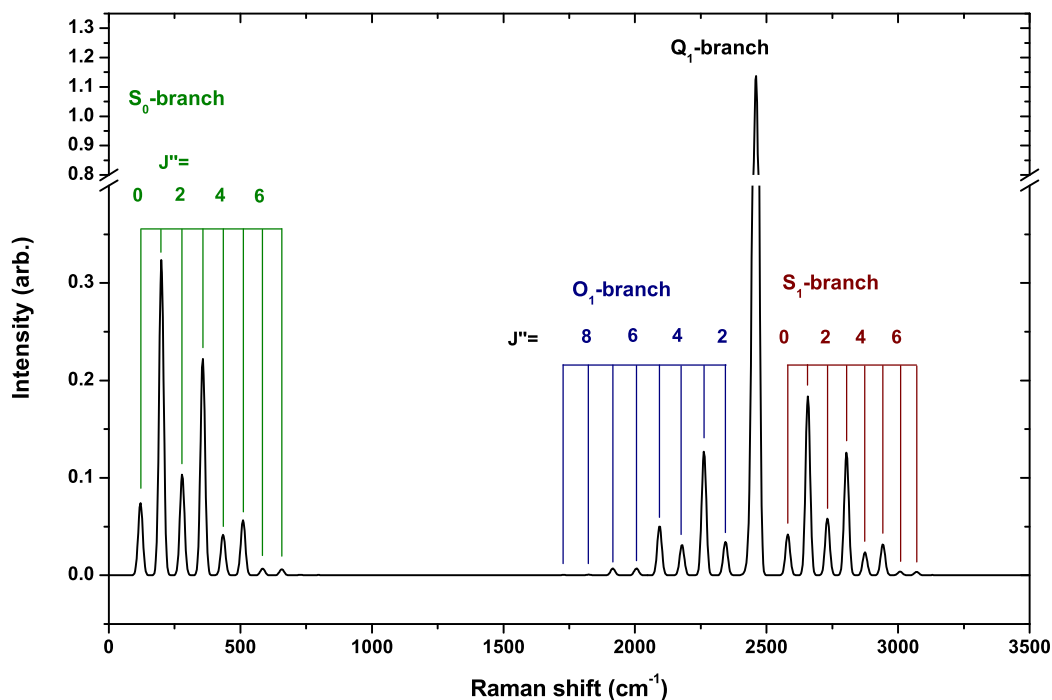


Figure 3.8: Theoretical spectrum of T_2 for a constant line strength function. This spectrum was simulated using the SpecGen package [SPE09]. Input parameters were: 532 nm excitation source, 300 K temperature and a spectral resolution of 8.5 peak width which is comparable to the resolution of the HTS spectrometer at TLK. The line intensities are correct within about 5 % since the line strength function was not considered yet. J'' indicates the initial rotational quantum number of the rotational transition. Please note the scale breaking in the intensity axis. Figure taken from [Sch09].

the vibrational states. Hence, also higher states than the ground state are populated at room temperature: For T_2 (H_2) even the rotational state with $J'' = 10$ ($J'' = 5$) has a relative population of $>10^{-4}$ which is within the range of sensitivity of a typical Raman systems with scientific grade detector.

Before the line strength function is discussed, a theoretical spectrum of T_2 without considering the line strength function is shown in figure 3.8. The line widths are comparable to the experimental achieved resolution in this thesis. 6 to 8 lines are visible within the O_1 and S_1 branches. The alternation within the rotational branches due to the influence of the nuclear spin is clearly visible. In figure 3.9, the theoretical spectra for all 6 hydrogen isotopologues are plotted, again without considering the line strength function. The Q_1 branches dominate the spectrum and can be used to identify the individual isotopologues.

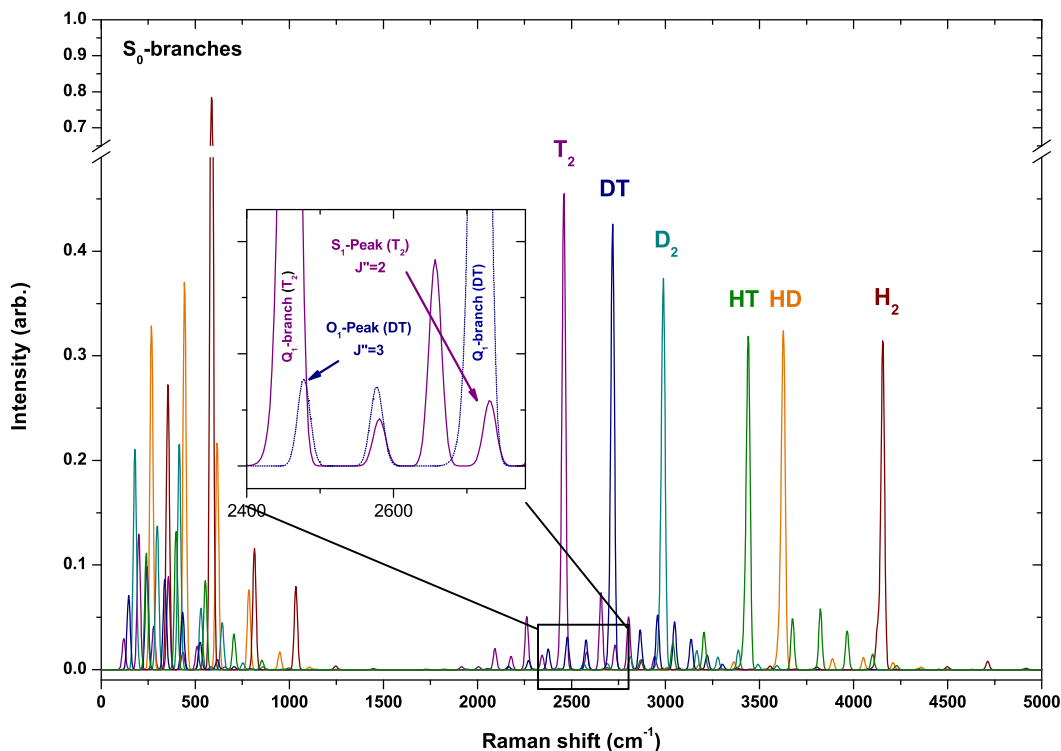


Figure 3.9: Theoretical spectrum of all hydrogen isotopologues for a constant line strength function. The spectra were simulated with the SpecGen [SPE09] package using the same settings as in figure 3.8. The Q₁ branches are the best candidates for the quantitative analysis of the spectra due to their large intensity and clear separation between each other. Minor overlaps of the Q₁ and S₁ branches of T₂ and DT can be identified (shown in the inset figure) which have to be taken into account for quantitative analysis. The line intensities are correct within about 5 % since the line strength function was not considered yet. Figure taken from [Sch09].

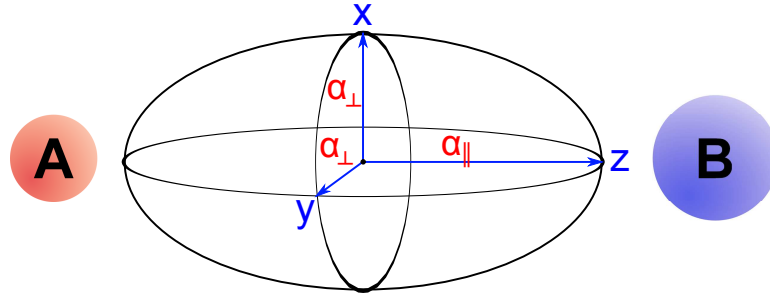


Figure 3.10: Polarisation ellipsoid of a hetero-nuclear molecule AB. The distance of a point p on the surface of the ellipsoid from the origin O is a measure for the polarisability of the molecule in the direction Op . The polarisability is maximal along the molecule axis, the z -axis, and invariant under rotations around the molecular axis due to the cylindrical symmetry of the molecule. Therefore the ellipsoid can be described by two parameters, i.e. the polarisability along the molecule axis α_{\parallel} and perpendicular to the molecule axis α_{\perp} .

3.1.5 Line strength function and polarisability tensor

According to (3.28) the line strength function $\Phi(a^2, \gamma^2, \Theta, p^s, p^i)$ is one of the parameters that determines the absolute peak intensity in Raman spectra. $\Phi(a^2, \gamma^2, \Theta, p^s, p^i)$ depends on the molecular specific constants a^2 and γ^2 that describe the polarisability of the molecules, on the geometry of the setup denoted by the generic variable Θ , and on the polarisation of the incident (p^i) and scattered (p^s) light. In this subsection the relations between a and γ , the quantum mechanical polarisability transition tensor α_{fi} and the line strength function will be motivated. α_{fi} describes the polarisability of a molecule related to a transition of the molecule from an initial state $|i\rangle$ to a final state $|f\rangle$.

For simplicity, the subscript “ fi ” will be omitted in further writing and α_{fi} will be just referred to as the polarisability tensor as long it is consistent with clarity and unambiguity.

The polarisability of a molecule is described by the polarisability tensor α which can be represented by a 3×3 matrix

$$\alpha = \begin{pmatrix} \alpha_{xx} & \alpha_{xy} & \alpha_{xz} \\ \alpha_{yx} & \alpha_{yy} & \alpha_{yz} \\ \alpha_{zx} & \alpha_{zy} & \alpha_{zz} \end{pmatrix} \quad (3.31)$$

that characterises the polarisability ellipsoid of the molecule (see figure 3.10). The explicit form of α depends on the chosen coordinate system. In case of a diatomic molecule, α is given by

$$\alpha = \begin{pmatrix} \alpha_{\perp} & 0 & 0 \\ 0 & \alpha_{\perp} & 0 \\ 0 & 0 & \alpha_{\parallel} \end{pmatrix}. \quad (3.32)$$

in the molecule fix coordinate system, i.e. in a coordinate system with z -axis along the

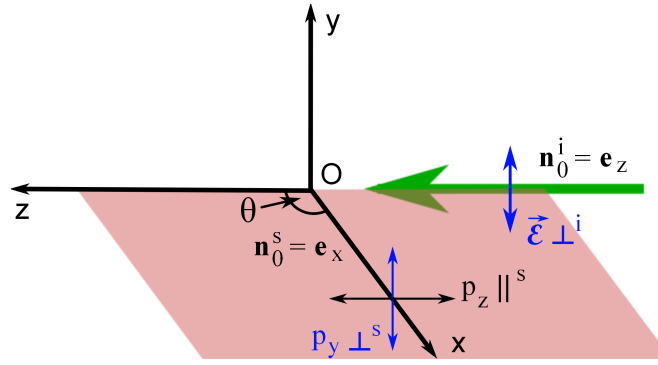


Figure 3.11: Definition of scattering geometry for fixed light collection system in the laboratory fix coordinate system. The scattering region is located in the origin. The x- and z-axes define the scattering plane (coloured area) which is parallel to the breadboard of the optical setup. The incoming laser beam (green) with direction vector n_0^i is vertically polarised, i.e. the electric field vector $\vec{\mathcal{E}} = \mathcal{E}_y \cdot \vec{e}_y$ is perpendicular to the scattering plane (denoted by the symbol \perp^i). The scattered light is collected along the x-axis and has a vertically polarized (symbol \perp^s) and parallel polarized (symbol \parallel^s) component relative to the scattering plane. A more general but consistent definition of the angle θ will be given in figure 3.12.

molecule axis. The average polarisability a and the anisotropy γ

$$a = \frac{1}{3}(\alpha_{\parallel} + 2\alpha_{\perp}) \quad (3.33)$$

$$\gamma = \alpha_{\parallel} - \alpha_{\perp} \quad (3.34)$$

of the diatomic molecule are so-called polarisability invariants, i.e. they are independent of the coordinate system, and hence represent molecular specific properties [Lon02].⁴

The intensity of the scattered light is, according to (3.26), proportional to the square of the dipole moment

$$\vec{p} = \alpha \cdot \vec{\mathcal{E}} \quad (3.35)$$

which is induced by the electrical field vector $\vec{\mathcal{E}}$ of the incident laser radiation.

In the Raman measurements performed for KATRIN the laser light is vertically polarised. In a laboratory fix coordinate system (see figure 3.11) this is expressed by $\mathcal{E}_x = \mathcal{E}_z = 0$ and $\mathcal{E}_y \neq 0$ and denoted by the symbol $p^i = \perp^i$, indicating that the polarisation direction of the incident light is perpendicular to the scattering plane. Considering the scattering of the vertically polarised laser light on a single, arbitrarily rotated molecule reduces the electric dipole moment in (3.35) to

$$p_x = \alpha_{xy} \mathcal{E}_y \quad (3.36)$$

$$p_y = \alpha_{yy} \mathcal{E}_y \quad (3.37)$$

$$p_z = \alpha_{zy} \mathcal{E}_y. \quad (3.38)$$

The light detection system of the Laser Raman setup of KATRIN is placed on the x-axis of the setup ($\theta = \frac{\pi}{2}$) and is insensitive on the polarisation of the scattered light

⁴The anisotropy γ can in principle become negative using this definition. Since always γ^2 will appear in the formulas in the following the sign of γ does not have a physical meaning.

and hence detects the vertical (\perp^s) and the horizontal (\parallel^s) component of the scattered light. This will be denoted in the following by $p^s = \perp^s + \parallel^s$. For simplicity it is assumed in this section that the aperture of the light detection system is very small, i.e. the system collects only the light which is emitted directly along the x-axis. This assumption is not valid in a real experiment since the aperture of the light collection system has to be large to maximise the observed intensity. The necessary corrections due to the finite opening angle of the light collection system will be implemented in this treatment in subsection 6.1.1.

The line strength function $\Phi(a^2, \gamma^2, \Theta, p^s, p^i)$ for this simplified configuration will be deduced in the following steps.

Only the transversal (y- and z-) components of the electric dipole moment relative to the propagation direction of the scattered light have to be considered for the calculation of the line strength function since the in x-direction emitted light is transversally polarised and hence $p_x = 0 \Rightarrow \alpha_{xy} = 0$. The observed intensity due to a single molecule as scattering target is hence given by

$$I = \frac{\pi^2 c}{2\varepsilon_0} \tilde{\nu}_s^4 \cdot (\alpha_{yy}^2 + \alpha_{zy}^2) \cdot \mathcal{E}_y^2 \sin^2 \theta. \quad (3.39)$$

according to (3.26) and (3.37)-(3.38).

In real scattering experiments with gaseous samples, the laser light always scatters on a population of N_i isotropically oriented molecules. Therefore the factor N_i has to be introduced and the involved components of α have to be averaged over all orientations of the molecules. In this averaging process also the $\sin^2 \theta$ term is averaged over all angles θ . The isotropic averages of the components of α are denoted by parentheses, e.g. α_{yy}^2 becomes the isotropic average $\langle \alpha_{yy}^2 \rangle$. The constant factor from the averaging of $\sin^2 \theta$ is also contained in the isotropic averages. The intensity of scattered light therefore becomes

$$I = \frac{\pi^2 c}{2\varepsilon_0} \tilde{\nu}_s^4 \cdot N_i \cdot \left(\langle \alpha_{yy}^2 \rangle + \langle \alpha_{zy}^2 \rangle \right) \cdot \mathcal{E}_y^2. \quad (3.40)$$

In a next step the square of the electric field vector \mathcal{E}_y can be replaced by the intensity $\mathcal{I} = \frac{1}{2} c \varepsilon_0 \mathcal{E}_y^2$ of the incident laser light [Dem02].

$$I = \frac{\pi^2}{\varepsilon_0^2} \tilde{\nu}_s^4 \cdot N_i \cdot \mathcal{I} \cdot \left(\langle \alpha_{yy}^2 \rangle + \langle \alpha_{zy}^2 \rangle \right). \quad (3.41)$$

The isotropic averages of the components of α can, in turn, be expressed by the polarisability invariants a and γ

$$\langle \alpha_{yy}^2 \rangle = \frac{45a^2 + 4\gamma^2}{45} \quad (3.42)$$

$$\langle \alpha_{zy}^2 \rangle = \frac{\gamma^2}{15} \quad (3.43)$$

[Lon02] which finally leads to

$$\begin{aligned} I &= \frac{\pi^2}{\varepsilon_0^2} \cdot \tilde{\nu}_s^4 \cdot N_i \cdot \mathcal{I} \cdot \left(\frac{45a^2 + 4\gamma^2}{45} + \frac{\gamma^2}{15} \right) \\ &= k_{\tilde{\nu}} \cdot \tilde{\nu}_s^4 \cdot N_i \cdot \mathcal{I} \cdot \left(\frac{45a^2 + 7\gamma^2}{45} \right) \end{aligned} \quad (3.44)$$

where $k_{\bar{\nu}}$ was introduced according to (3.30).

By comparing (3.44) with (3.26) the line strength function $\Phi(a^2, \gamma^2, \Theta, p^i, p^s)$ can be identified for the case of vertically polarised incident (\perp^i) laser light and the detection of the parallel (\parallel^s) and perpendicular (\perp^s) components of the scattered light in a 90° geometry ($\pi/2$) to the initial beam direction.

$$\Phi(a^2, \gamma^2, \frac{\pi}{2}, \perp^s + \parallel^s, \perp^i) = \frac{45a^2 + 7\gamma^2}{45} \quad (3.45)$$

Although the index “ fi ” of the polarisability (transition) tensor was omitted for the calculation of the line strength function it is important to keep in mind that the calculation was done for an arbitrary but fixed Raman transition from initial state $|i\rangle$ to final state $|f\rangle$. The initial state is thereby essentially defined by the initial rotational quantum number v_i and vibrational quantum number J_i while the final state is characterised accordingly by v_f and J_f . Therefore the molecule specific parameters a and γ and hence the line strength function will in general depend on the initial and final state which implies that every line in a Raman spectrum is characterised by an individual set of a and γ values.

The gas composition of the source gas of KATRIN will be determined by the measurement of the line intensity in Raman spectra and a comparison to theoretically calculated spectra. For the accurate calculation of the theoretical spectra the knowledge of the average polarisability a and the anisotropy γ for several dozen of transitions $|i\rangle \rightarrow |f\rangle$ is necessary since it has been shown in subsection 3.1.4 that rotational lines with up to $J'' = 10$ are expected to contribute to the branches in experimentally measured spectra. The accuracy of the available data on a and γ has an impact on the calculation of theoretical Raman spectra and hence on the measurement of the source gas composition of KATRIN. Therefore the status of calculations and measurements of the a and γ values for hydrogen isotopologues will be addressed in the next section.

3.2 Overview and status of calculations of polarisability

In this section a brief historical overview of the calculation of a and γ will be given, followed by a short discussion whether the currently available set of data is sufficient for KATRIN.

The a and γ values of transitions of all hydrogen isotopologues can be calculated in *ab initio* calculations since the hydrogen isotopologues are the most simple molecules with two nuclei and two electrons. The calculations go back to the 1930s when the first attempts were made by B. Mrowaka [Mro32]. A significant improvement was reached in 1952 when Ishiguro et al. applied a new calculation method, the variation-perturbation method [Ish52]. This approach is based on the Born-Oppenheimer approximation because of the slow movement of the heavy nuclei in comparison to the fast movement of the light electrons. In addition, further corrections are necessary for the treatment of hydrogen isotopologues, namely the radiative [Bis69], adiabatic [Wol83] and nonadiabatic [Wol83] [Bun77a] [Bun77b] corrections.

The result of the variation-perturbation method is a set of numerical molecular wave functions which can be used to calculate expectation values of physical variables, e.g. the energy of excited states and hence the line positions and the parameters a and

γ . This method was improved by Kolos et al. but only applied on the non-tritiated isotopologues H_2 , HD and D_2 [Kol64] [Kol86]. Furthermore, the polarisability was only calculated for excitation wavelengths $\lambda \rightarrow \infty$. The wavelength dependence of the polarisability was taken into account for the first time by J. Rychlewski [Ryc83] but again only for the non-tritiated species. In 1984 the tritiated species were considered the first time by Hunt et al. but again for the limit of infinite laser wavelength and with a simplified nuclei potential [Hun84]. Schwartz and LeRoy calculated in 1987 the polarisabilities of the non-tritiated hydrogen isotopologues for $\lambda = 488 \text{ nm}$ and $\lambda \rightarrow \infty$ using an advanced nuclei potential [Sch87]. The calculated molecular energy states of the non-tritiated species were compared to available experimental results [Vei87]. The energies of molecular states of the tritiated species were additionally obtained by a scaling procedure. In 2004 the polarisabilities of HD, HT and DT were recalculated by B. Rao et al. [Bak04].

Experimental data on a and γ are only available for the non-tritiated isotopologues [Gol62] presumably due to the enhanced experimental challenges that arise from the handling of the radioactive tritium gas. The measurements were based on the determination of the dielectric constant [Her65], depolarisation measurements [Bri66] [Row71] and absolute measurements [Car72]. Therefore, the theoretical calculations were only verified for the non-tritiated isotopologues while the experimental verification of the theoretical data of the tritiated species is currently still pending.

An experimental verification of the theoretical data on polarisabilities of the tritiated hydrogen isotopologues is necessary to check the reliability of the theoretical data before they can be applied for KATRIN. The TLK offers the necessary tritium infrastructure to perform these measurements.

3.3 Experimental determination of a/γ ratios

In this section a method is proposed that allows a measurement of the ratio of the mean polarisability a and the anisotropy γ and hence makes a comparison of theoretical and experimental data possible. The more favourable measurement of both individual parameters a and γ would require the measurement of the absolute cross section of Raman scattering. For this measurement an absolute intensity calibration of the LARA setup and hence tremendous experimental efforts would be necessary. Therefore the measurement of the a/γ ratios is currently preferred since it allows a first comparison between theory and experiment without too many experimental efforts.

In the previous section the line strength function

$$\Phi(a^2, \gamma^2, \frac{\pi}{2}, \perp^s + \parallel^s, \perp^i) = \frac{45a^2 + 7\gamma^2}{45} \quad (3.46)$$

was calculated for the standard setup of the KATRIN Raman setup, i.e. for a fixed detector system and vertically polarised incident light.

Up to now the influence of the rotational states was not fully considered in the line strength function. Depending on the symmetry of the rotational states, the anisotropy part of the polarisability tensor is suppressed. The Placzek-Teller factors $b_{J', J''}^{(2)}$ allow to account for this effect [Pla33] and are inserted as a multiplicative factor in front of

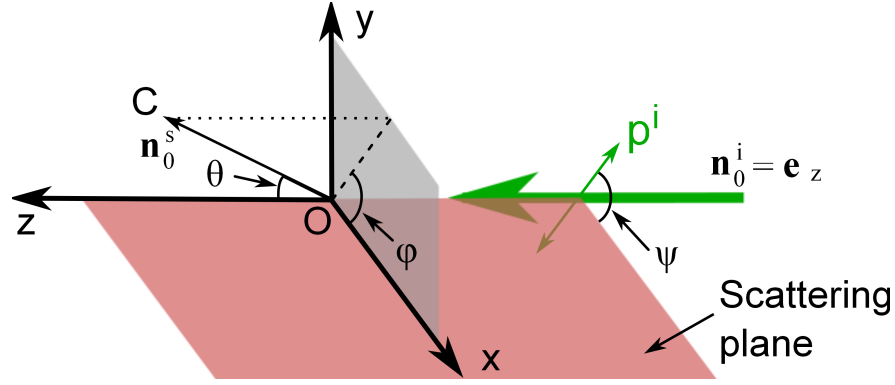


Figure 3.12: Definition of scattering geometry with variable direction of scattered light and variable polarisation direction of the incident light. A laboratory fix coordinate system is used to describe the geometry of the scattering process. The scattering plane (coloured area) is defined by the x- and z-axis. The incident light (green) enters the scattering region, located in the origin O, in z-direction. The polarisation p^i of the incident light is given by the polarisation angle ψ . The direction OC of the scattered light is determined by two angles: The angle θ between the z-axis and OC and the angle φ between the x-axis and the projection of OC on the xy-plane.

each γ^2 term in the line strength function.

$$\Phi(a^2, \gamma^2, \frac{\pi}{2}, \perp^s + \parallel^s, \perp^i) = \frac{45a^2 + 7 b_{J',J''}^{(2)} \gamma^2}{45} \quad (3.47)$$

For pure vibrational transitions, i.e. $\Delta J = 0$ and $J'' = J' = J$, the Placzek-Teller factor is given by

$$b_{J,J}^{(2)} = \frac{J(J+1)}{(2J-1)(2J+3)} \quad (3.48)$$

[Lon02], for Stokes Raman, i.e. $\Delta J = +2$ and $J' = J'' + 2$ by

$$b_{J''+2,J''}^{(2)} = \frac{3(J+1)(J+2)}{2(2J+1)(2J+3)}. \quad (3.49)$$

For an arbitrary detector position and polarisation angle of the incident light, described by the angles θ , φ and ψ (see figure 3.12), the line strength function is given by

$$\begin{aligned} \Phi(a^2, \gamma^2, \varphi, \theta, \perp^s + \parallel^s, \psi) = & \\ \frac{b_{J',J''}^{(2)} \gamma^2}{15} + \left[\left(a^2 + \frac{b_{J',J''}^{(2)} \gamma^2}{45} \right) \cdot \cos^2 \theta + \frac{b_{J',J''}^{(2)} \gamma^2}{15} \right] \cdot \cos^2(\varphi - \psi) + & \\ \left(a^2 + \frac{4}{45} b_{J',J''}^{(2)} \gamma^2 \right) \cdot \sin^2(\varphi - \psi) & \end{aligned} \quad (3.50)$$

[Lon02]. This general formula of the line strength function can be used to calculate the expected variation of the peak intensity as a function of the polarisation angle ψ of the incident light. For simplicity and clearness, the approximation of an infinite small

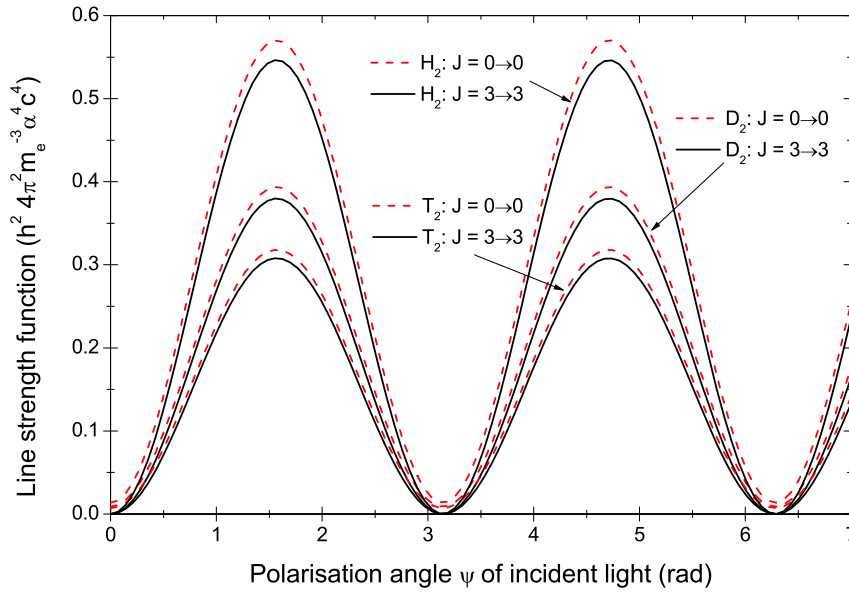


Figure 3.13: Variation of line strength function as a function polarisation angle of incident light for standard geometry, i.e. $\varphi=0$ and $\theta=\frac{\pi}{2}$. The line strength function is plotted for the three homo-nuclear isotopologues and for the transitions $v=0 \rightarrow 1$, $J=0 \rightarrow 0$ (black, solid line) and $v=0 \rightarrow 1$, $J=3 \rightarrow 3$ (red, dashed line). The deviations of the line strength function between the two transitions but within every isotopologue are small in comparison to the deviations between different isotopologues. The line intensities of the $J=3 \rightarrow 3$ transitions decrease down to zero. The unit of the line strength function contains the fine-structure constant $\alpha \approx 1/137$, the electron mass m_e and Planck's constant $h=6.626 \cdot 10^{-34}$ Js. The calculation of the line strength function is based on theoretical values for a and γ from [Hun84].

aperture of the collection optics is used in this section which will again simplify equation (3.50). The full φ , θ and ψ dependence of (3.50) will be used in subsection 6.1.1 where the finite solid angle of the collection optics is taken into account. In the approximation of a detector at standard position, i.e. $\varphi=0$ and $\theta=\frac{\pi}{2}$, with an infinite small aperture the line strength function (3.50) reduces to

$$\Phi\left(0, \frac{\pi}{2}, \perp^s + \parallel^s, \psi\right) = \frac{b_{J',J''}^{(2)} \gamma^2}{15} \cdot \left(1 + \cos^2(\psi)\right) + \left(a^2 + \frac{4}{45} b_{J',J''}^{(2)} \gamma^2\right) \cdot \sin^2(\psi). \quad (3.51)$$

The line strength function is plotted in figure 3.13 for the transition $v=0 \rightarrow 1$, $J=0 \rightarrow 0$ and $v=0 \rightarrow 1$, $J=3 \rightarrow 3$ for each of the three homo-nuclear isotopologues H_2 , D_2 and T_2 using the theoretical values of a and γ from [Hun84]. It can be seen that a significant variation of the line strength function and hence of the observed intensity of the scattered light is present when the polarisation angle of the incident light is varied.

Using the variation of the observed intensity of scattered light according to figure 3.13, the a/γ ratios can be experimentally determined in 3 steps:

- The line intensity of all peaks of interest in the Raman spectra⁵ are measured as a function of the polarisation angle ψ of the incident light. The spectral resolution of the spectrograph and the CCD has to be sufficient to resolve all peaks individually since every peak is characterised by an individual set of a and γ values.
- The theoretically expected line strength function, given by equation (3.51), multiplied by an overall scaling factor κ is fitted on the experimentally measured intensity variation of the individual peaks using $\kappa \cdot a^2$ and $\kappa \cdot \gamma^2$ as fit parameters. The overall scaling factor contains according to (3.28) the irradiance \mathcal{I} , the population factor N_i and the $\tilde{\nu}_s^4$ factor and is assumed to be independent of the polarisation angle of the incident light. The goodness of the fit is a measure for possible unaccounted experimental effects in the setup.
- The a/γ ratio is determined by the division of the the two fit parameters, i.e.

$$\frac{a}{\gamma} = \sqrt{\frac{\kappa \cdot a^2}{\kappa \cdot \gamma^2}} \quad (3.52)$$

The individual values for a and γ cannot be extracted from this measurement since κ is not quantified. A determination of κ in order to extract the individual values for a and γ from the data would correspond to the measurement of the absolute cross section of Raman scattering and would require the full characterisation of all effects in the setup which are related to transmission or loss of light.

In the following the method described in this section is called depolarisation measurement a and γ determine the ratio of the intensities of the parallel and horizontal polarisation components of the scattered light⁶.

The depolarisation measurements are based on the assumption that the irradiance \mathcal{I} , the laser frequency $\tilde{\nu}_s$ and the population factor N_i are constant during the measurement. Changes of N_i can be neglected as long the temperature is kept constant. Changes of the laser frequency depend on the stability of the laser itself and cannot currently be excluded completely since the temperature of the laser is currently not stabilised.

After a description of the experimental setup in the next chapter it will be shown in chapter 5 that fluctuations and drifts of the laser power are currently the most dominant issue in the setup. In order to cope with varying laser powers during the depolarisation measurements, the measured intensity can be normalized on the laser power. The accuracy of the determination of the a/γ ratios can be enhanced by increasing the number of independent measurements, i.e. by decreasing the step size of the polarisation angle of the incident light. The first depolarisation measurements with tritium which were performed at TLK for the determination of the a/γ ratios will be described chapter 6.

⁵Currently the peaks of the Q₁ branches are the most important since the current analysis bases on the intensity of these. In the future also the O₁ and S₁ branches will be taken into account. Therefore also the a/γ ratios of these have to be measured and verified.

⁶In typical depolarisation measurements the individual polarisation components of the scattered light are measured as a function of the polarisation angle of the incident light. Although this is not the case in this work, since both polarisation components are detected simultaneously, the measurements will be called depolarisation measurements.

Chapter 4

Description of the experimental setup LARA2

Raman spectroscopy always deals with the detection of low light intensities because of the small cross section of the spontaneous Raman effect which is typically of the order 10^{-30} cm² [Men07]. By comparison, Rayleigh scattering has a much higher cross section of the order 10^{-28} cm² [Sut04]. The low particle density in a gaseous sample further reduces the intensity of the scattered light compared to Raman spectroscopy at liquid or solid samples. For Raman spectroscopy of tritium additional requirements are imposed on the experimental setup due to safety reasons since tritium is a radioactive gas.

Currently no commercial system is available that fulfils all requirements for Raman spectroscopy on gaseous tritium within the KATRIN project, i.e. the measurement of the hydrogen isotopic composition with 10^{-3} (1σ) precision for tritium over a periode of 60 days. Therefore a custom-made Raman setup was successfully developed by R. Lewis in 2005-2007 [Lew07] in the Tritium Laboratory Karlsruhe. Within the scope of this thesis a second Raman setup based on the same design was build, commissioned and tested. In order to avoid confusion the already existing system will be called “LARA1” in this thesis and the new setup “LARA2”.

The motivation for a second LARA setup in the Tritium Laboratory Karlsruhe is stated in section 4.1. A general description of LARA2 is given in section 4.2. Finally the components of LARA2 are presented in detail in section 4.3.

4.1 Motivation for second Laser Raman setup at TLK

The existing setup for Raman spectroscopy on tritium at the TLK was extensively studied by M. Schlösser [Sch09]. It has been shown that the setup is suitable to monitor all six hydrogen isotopologues simultaneously [Stu10a] and sources of systematic influences on the measurement were identified. The research and development of Raman setups for tritium will be further intensified at TLK within the next years. Several reasons given below show the need for a second Raman setup.

- The Inner Loop system of KATRIN and a test loop system, called LOOPINO (described in section 4.3), were successfully commissioned in November 2009 [Stu10b]

[Pri09]. The Inner Loop is only operated with non-tritiated gases until the WGTS is installed and connected to the Inner Loop. The test loop system LOOPINO allowed to run first long term Raman measurements of circulating tritium in LOOPINO over periods of several weeks. Besides the long term measurements at LOOPINO, also investigations on systematic effects, e.g. due to fluctuations of the laser, will be performed. Therefore a second Raman system is necessary that can be used in parallel to the long term measurements at LOOPINO.

- An accurate theoretical calculation of Raman spectra is necessary for the determination of the hydrogen isotopologue composition in the inlet gas of the WGTS. Not all quantum mechanical input parameters of the theoretical model are currently known with sufficient precision and therefore have to be measured. For this measurement, described in chapter 6, the beam path has to be aligned very accurately which is currently not possible in the existing LARA1 setup. Therefore a second setup was needed that allows the alignment of the laser path relative to the LARA cell using two or even more mirrors.
- The second setup can be used as a backup of the first one. In case of a fault of the LARA system during KATRIN neutrino mass measurements, the downtime of the experiment can be reduced when a second LARA system is available on site. Even if the second system does not reach the same sensitivity level as the first one the measurement can be continued with reduced precision.
- Systematic effects induced by the hardware components of the KATRIN Raman setup might be detected by repeating measurements with an independent experimental setup that is e.g. made of different components. The origin of the effects can be identified by a successive exchange of components among the different setups.

4.2 General description of LARA2

A typical scheme of a Raman setup was already shown in figure 3.2. It consists of three major components:

- An intense and monochromatic **light source**, typically a laser.
- A **probe chamber** containing the gas of interest, here tritium.
- A system consisting of a **spectrograph and a light sensitive detector**, e.g. a CCD¹, for analysis of the scattered light.

Figure 4.1 shows a schematic drawing of the standard LARA2 setup. A laser beam with 532 nm wavelength and 2 W power is emitted by a diode pumped solid state laser. The beam is guided by two mirrors (M1, M2) to the probe chamber, which is called LARA cell. A Glan-Taylor-Polariser (GTP) is placed into the beam path to remove any remaining vertical polarization component from the horizontally polarised laser light: The horizontally polarised component can pass the GTP while the vertical component is split off and dumped. A focus lens (L1) with 250 mm focal length focuses

¹Charge coupled device

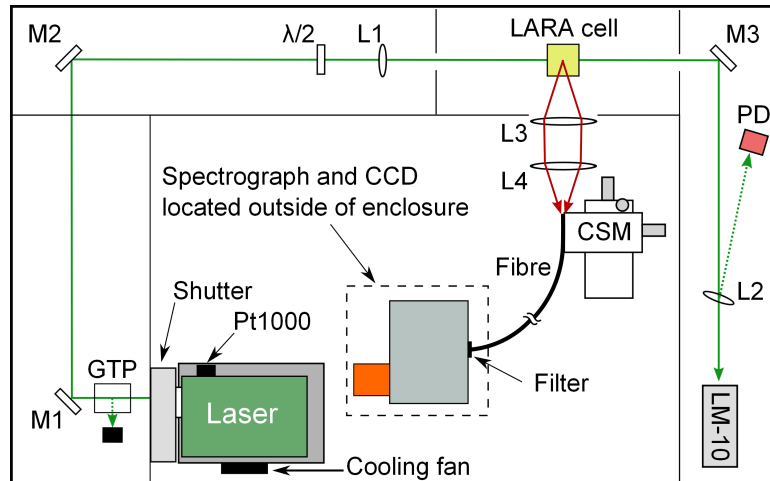


Figure 4.1: Schematic drawing of LARA2 setup. The laser beam is guided by the mirrors (M1, M2) to turn the LARA cell which is placed in the focal plane of the focus lens (L1). The $\lambda/2$ wave plate is used to turn the polarisation of the light from horizontal to vertical direction. The scattered light leaves the LARA cell through a side window and is imaged by collection optics (L3, L4) onto a fibre that guides the light to the spectrograph which is located outside the enclosure of LARA2. A razor edge filter for the suppression of the initial laser wavelength is placed between the fibre and the entrance slit of the spectrograph. The fibre can be aligned by the collection side mount (CSM). The laser power is measured by two devices: A photo diode (PD) that monitors the reflection of the laser beam on the sampling lens L2 and by the thermopile sensor LM-10. All components are mounted on a breadboard. For further information see text.

the beam directly on the centre position of the cell. A $\lambda/2$ wave plate is used to turn the polarisation of the light from horizontal to vertical direction². The scattered light is collected by two lenses (L3, L4) and is imaged onto a optical fibre that guides the light to a razor edge filter which suppresses the laser line. Two images of the focus and collection optics can be found in figure 4.2. Afterwards the light is sent to a spectrograph that decomposes the scattered light into its different wavelengths. The CCD is placed into the focal plane of the spectrograph and acquires the spectrum. The exposure time of a typical acquisition is 250 s due to the low intensity of the Raman scattered light. After an acquisition, software correction routines are applied on the image taken by the CCD to correct for several disturbing effects before the position and intensities of the spectral lines are used to obtain the Raman spectrum.

After passing through the LARA cell the laser beam is sent to the LM-10 sensor that measures the beam power and position and also acts as a beam dump. A reflection of the sampling lens (L2) is monitored by a photo diode (PD) for a second laser power measurement. A remote controlled shutter is placed in front of the laser. The heat sink of the laser is cooled by a fan and its temperature is monitored by a thermal sensor (Pt1000).

The optical setup is installed on a breadboard which is covered by a light tight enclosure for two reasons: It avoids that ambient stray light can disturb the measurement and it protects people in the lab from possible exposure to laser light. The razor edge

²This is done to align the direction in which the most of the scattered scattered light is emitted towards the collection optics

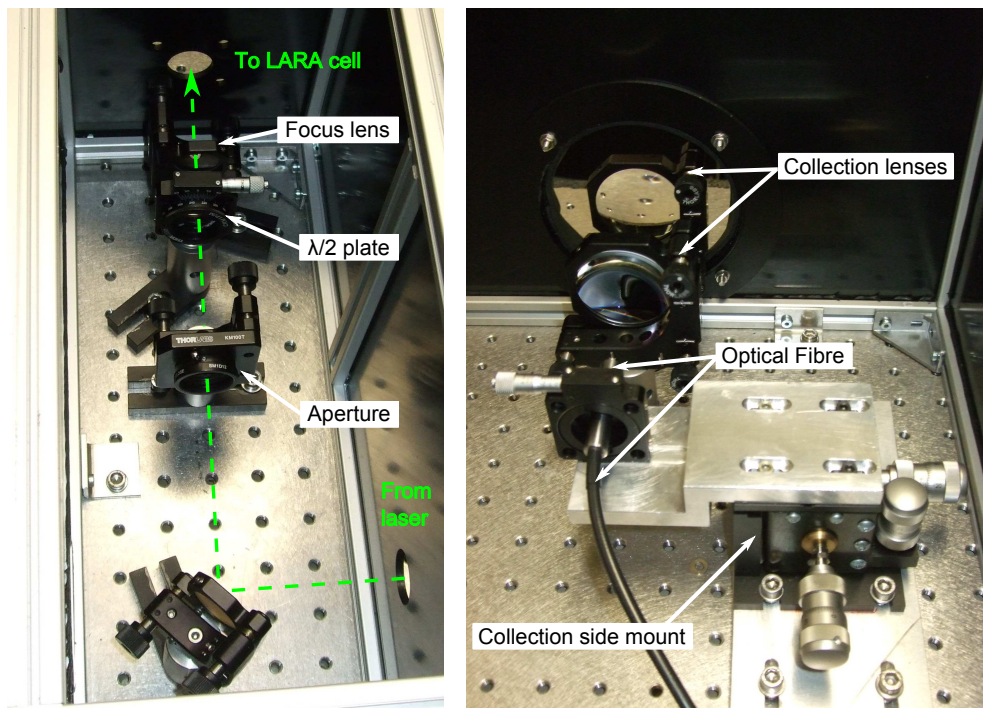


Figure 4.2: Optics of LARA2. *Left:* Top view on the optics between laser and LARA cell. The beam path is indicated by the green dashed line. The aperture is used for alignment of the beam, the $\lambda/2$ plate turns the polarisation direction into vertical direction, the focus lens focuses the beam on the centre position of the LARA cell (not shown). *Right:* Collection optics of LARA2. Two 2" lenses collect the scattered light from the LARA cell (not shown) and focus it on the optical fibres. The position of the fibres can be adjusted in all dimensions by the collection side mount and by a rotational mount that holds the fibres.

filter, the spectrograph and the CCD are placed in a separate enclosure underneath the breadboard due to the limited dimensions of the LARA2 setup.

4.3 The components of LARA2

In this section the components of LARA2 are discussed in detail. Due to the low intensity of Raman scattered light the components have to be optimised for high light throughput (collection optics, spectrometer) and high sensitivity (CCD).

4.3.1 The breadboard

The optical setup of LARA2 is mounted on a breadboard and covered by an enclosure. The breadboard is 90×75 cm in size and hence significantly smaller than the dimensions of LARA1 (120×75 cm). This allows to easily transfer the setup in the laboratory for measurements at various places. The spectrograph and CCD are placed inside an additional box underneath (called spectrograph box in figure 4.3) the breadboard to gain more space for the optical setup in the enclosure. Large spectrographs like the SP500, that is presented in subsection 4.3.6, do not fit in the spectrograph box.

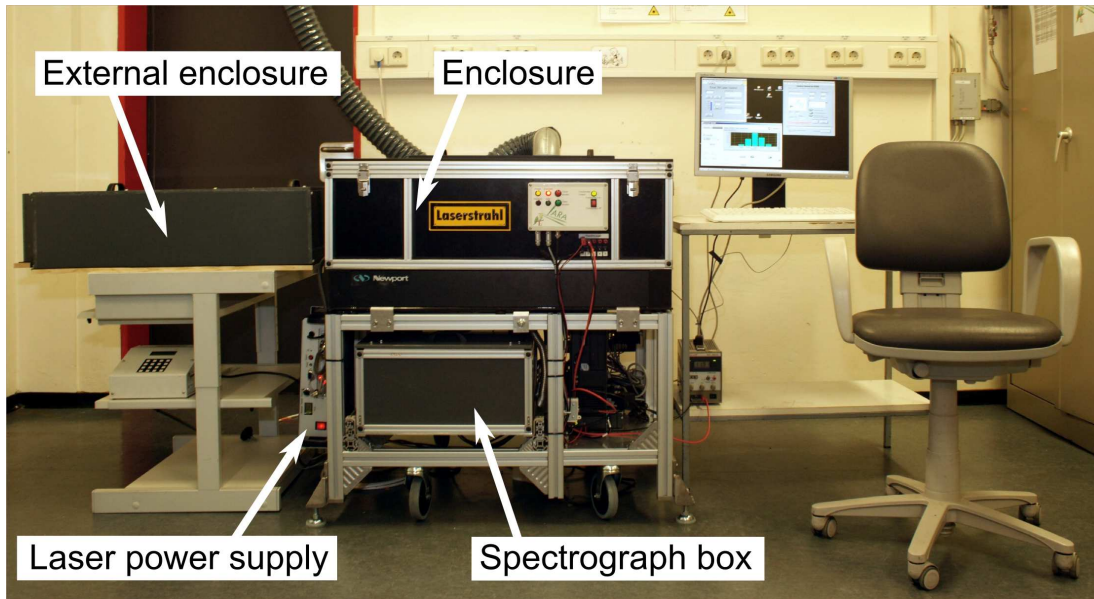


Figure 4.3: Side view of LARA2 setup. The optical setup is installed inside the enclosure. The spectrograph and CCD are normally placed inside the spectrograph box under the breadboard. The PC of the LARA2 setup is also installed in the base frame. The power supply of the laser is attached to the left side of the base frame. Larger spectrographs can be placed into the external enclosure and connected via the optical fibre.

They can be placed inside an external enclosure and connected to the fibre, as well. The LARA2 setup and its different enclosures can be seen in figure 4.3.

4.3.2 The Excel 2 W laser

The LARA2 setup uses the diode-pumped-solid-state³ laser Excel from Laser Quantum⁴ with 532 nm wavelength and 2 W nominal output power. The laser has a neodymium-doped yttrium aluminium garnet (Nd:YAG) crystal as gain medium which is pumped by laser diodes. The fundamental wavelength of the Nd:YAG crystal is 1064 nm [Eic06] which is frequency doubled using an optical crystal to the output wavelength of 532 nm. Despite its high output power, the laser head is very small in size (158 x 104 x 47 mm³). In table 4.1 the relevant specifications of the Excel laser are listed. The laser wavelength was also experimentally determined to 532.204 ± 0.002 nm by a characterisation measurement done at the University of Swansea, Wales [Als09].

The laser is mounted on a heat sink made of aluminium which is actively cooled by fan with 80 mm diameter (figure 4.4). For the first test measurements outside of the enclosure of LARA2 the laser was operated without active cooling of the heat sink without any problem. During the first operations of the laser inside the enclosure an overheating of the laser was observed and therefore a cooling fan installed. The overheating of the laser will be discussed in more detail in section 5.3. The laser can be controlled manually via the power supply or via a serial connection which is realized by a LabView program.

³DPSS

⁴Laser Quantum , Cheshire, UK

Table 4.1: Specifications of Excel laser according to [Exc06]

Property	Data
Power	2 W
Wavelength	532 nm
Beam size ($1/e^2$)	1.8 mm
Spatial Mode	TEM ₀₀ (Gaussian)
Power stability (within 8 hours)	< 3.0 % rms
RMS noise	3.0 %
Polarization direction	Horizontal (100:1)
Warm-up time	10 min

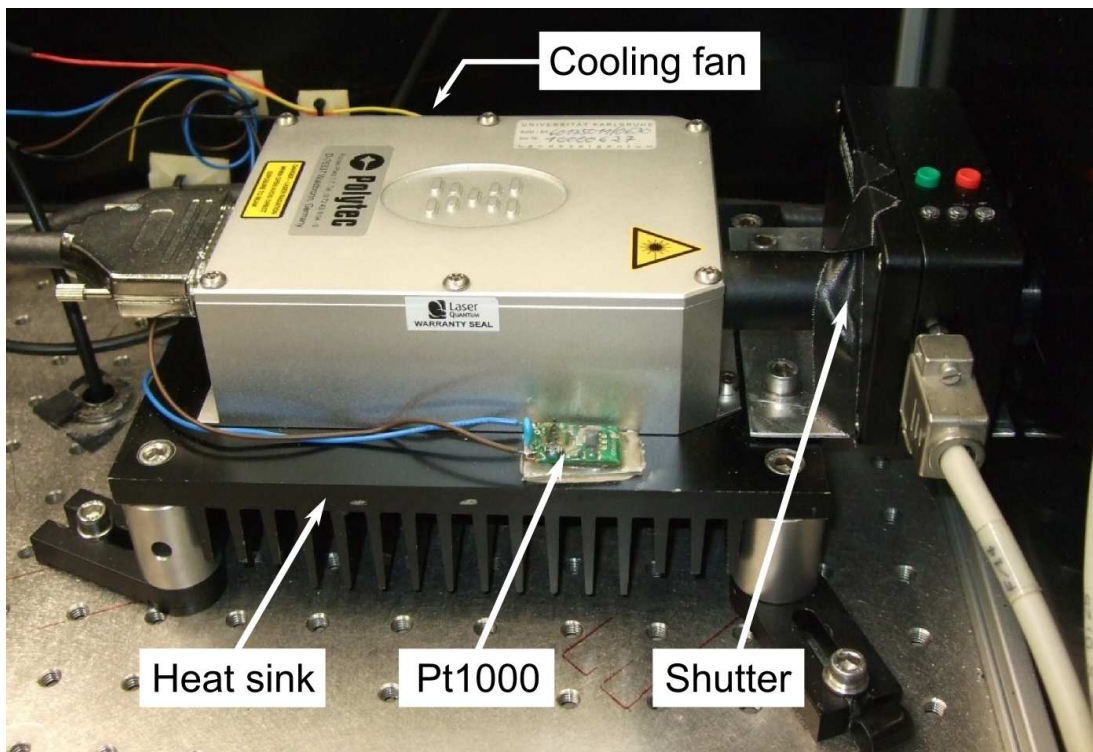


Figure 4.4: Excel laser mounted on heat sink. The cooling fan (not visible) is mounted on the back side of the heat sink and generates an air stream along the fins of the heat sink. The thermal sensor (Pt1000) is placed in front of the laser and measures the heat sink temperature. The shutter is mounted in front of the laser aperture to block the laser beam.

4.3.3 Laser beam path

The laser beam is guided by two 1" high-reflectivity mirrors to a lens with 250 mm focal length which focuses the beam in the centre of the LARA cell. The $\lambda/2$ wave plate is a birefringent crystal which is cut such that the extraordinary axis is parallel to the surface of the plate. If the wave plate is turned by an arbitrary angle ψ the polarisation angle of the light will be turned by 2ψ . Two wave plates were used within this thesis. The first is 0.2 mm thick and made of mica. It is placed between glass plates since mica is too brittle that it can be used without stabilisation. In total the wave plate and the glass plates are 2 mm thick. A second wave plate was installed in the LARA2 setup when it was realised that a non-acceptable beam displacement is induced by the glass plates (see Appendix C). The second wave plate is made of crystalline quartz which does not need an additional glass plates for stabilisation. Therefore the second wave plate is only about 0.2 mm thick and hence is called "thin" wave plate within this work while the first is called "thick" wave plate.

The small size of the laser head allows to place additional steering mirrors and optical components in the beam path between laser and LARA cell. This flexibility of the beam path was used in the measurements described in chapter 5 and chapter 6. Mirrors and focus lens are housed in ultra-stable KS1 mounts from Thorlabs⁵.

4.3.4 The LARA cell

The LARA cell contains the tritium gas and therefore has to fulfil certain requirements based on [TLA09], e.g. ultra vacuum leak-tightness (maximum leak rate below $10^{-9} \frac{\text{mbar}\cdot\text{l}}{\text{s}}$) and a full metal construction of the cell body and all seals. The laser beam enters and leaves the LARA cell through anti-reflection coated laser windows. A broadband anti-reflection coated window is used to send the scattered light out of the LARA cell. The optical windows of the cell have to fulfil optical requirements in addition to the requirements of tritium compatibility: Absorption losses in the windows below 0.01 %, low thermal effects and minimum fluorescence. This can be reached by windows made of fused silica. A procedure for the manufacturing of such windows in the LARA cell [Eng92] and a suitable design [Tay01] for the LARA cell itself were already developed in the former Forschungszentrum Karlsruhe and the TLK.

The LARA cell can be operated in two different ways:

Outside of glove box

The cell contains a static gas sample and is placed directly on the breadboard (figure 4.5). The volume around the cell is connected to the ventilation system of the TLK. In this configuration the cell is allowed to contain an activity up to 10^{10} Bq which corresponds to about 13 mbar partial pressure of T_2 .

Inside of glove box

In order to be allowed to perform Raman spectroscopy measurements on gas samples with activities above 10^{10} Bq, all tritium containing components have to be surrounded by a second containment, i.e. a glove box. Inside a glove box, the cell can be filled with gas samples with arbitrary tritium concentration and a total pressure of up to 800 mbar. This corresponds to a maximum activity inside the cell of about $6 \cdot 10^{11}$ Bq.

⁵Thorlabs, Dachau/Munich Germany

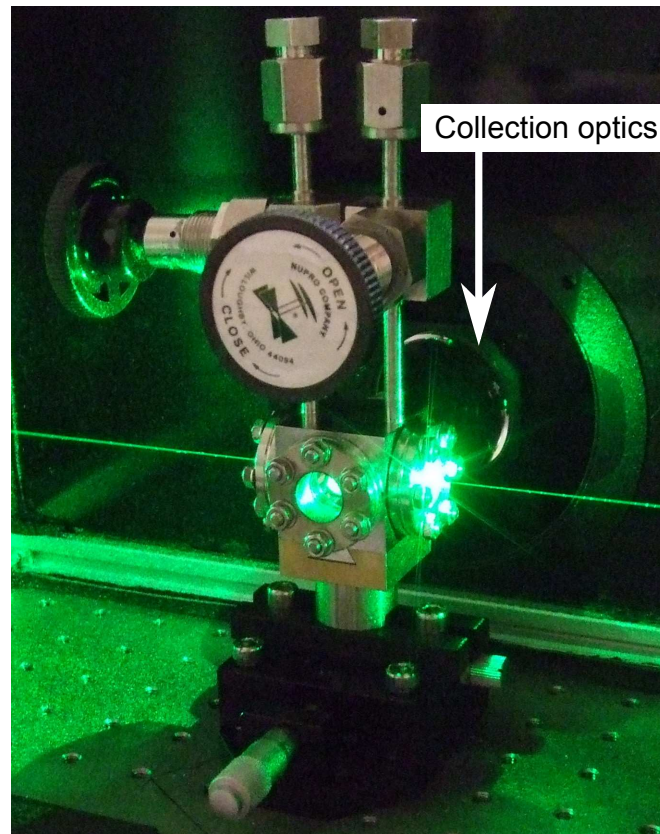


Figure 4.5: LARA cell outside of glove box. The LARA cell is placed outside of a glove box, not connected to a loop and filled with a static gas sample with maximum activity of 10^{10} Bq. The laser passes through the cell from right to left. The scattered light leaves the cell through the side window on the back side of the cell and is collected by the first lens of the collection optics (visible behind the LARA cell).

Besides high tritium concentrations it is also favourable to test the LARA system on flowing tritium gas similar to its final application in the Inner Loop system of KATRIN.

The Inner Loop system of KATRIN will not be operated with tritium until it is connected to the WGTS. Therefore the test loop system LOOPINO [Stu10b] was set up to perform Laser Raman measurements with flowing and high concentrated tritium (T_2 purity $> 90\%$ at about 100-200 mbar total pressure) until LARA can be operated at the Inner Loop system. LOOPINO is in comparison to the Inner Loop a simplified but similar loop system (see figure 4.6).

The LARA cell and LOOPINO are located, next to the Inner Loop system, inside the ISS glove box that serves as a second containment. The connection between the LARA cell and the LARA setup which is outside of the glove box is done by a custom-made interface, the so-called appendix (figure 4.7).

LOOPINO was operated the first time with tritium in November 2009 [Stu10b]. Most of the Laser Raman measurements that are described in chapter 5 and chapter 6 were performed at LOOPINO.

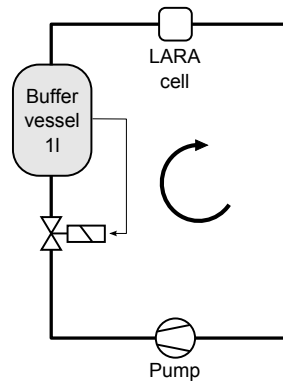


Figure 4.6: Simplified flow diagram of LOOPINO. The tritium is circulated by a pump from the buffer vessel through the LARA cell. The pressure stabilisation in the buffer vessel is obtained by the automatic valve. A total pressure of about 220 mbar and a tritium purity of $>90\%$ can be achieved in the system. For further details see [Stu10b].

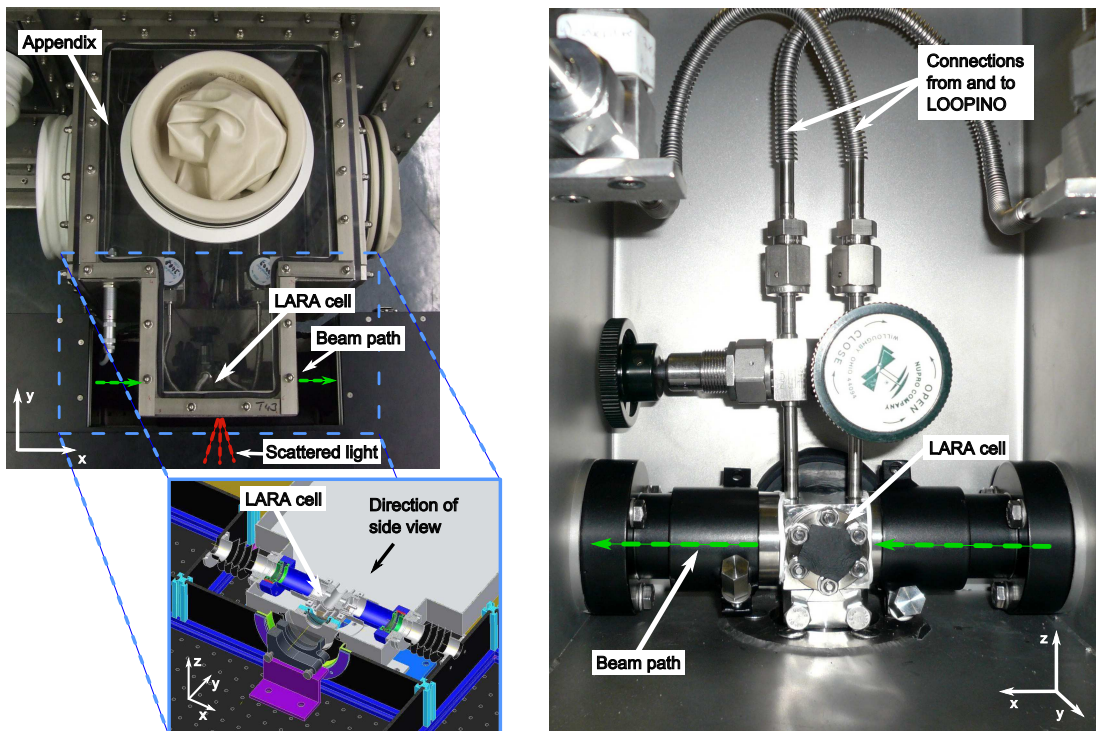


Figure 4.7: LARA cell inside appendix. *Left:* Top view of the LARA setup located in the appendix. The laser beam and the scattered light (both indicated by green and red dashed lines) enter and leave the appendix through optical windows. The connection of the appendix to the LARA setup is also shown in detail in the 3D drawing. All optical paths are covered with tubes for laser safety reasons. Inside the appendix the LARA cell can contain tritium samples with a maximum activity of about $6 \cdot 10^{11}$ Bq. *Right:* Side view of the LARA cell taken from the inside of the appendix. Note the coordinate axis for the orientation of the image. The laser beam (indicated by the green dashed line) passes from right to left through the LARA cell while the scattered light leaves the LARA cell and the appendix through windows on the backside of the LARA cell. The LARA cell is connected to LOOPINO and can be operated with circulated tritium. The window of the LARA cell which is on the opposite side of the collection optics is currently not used and hence masked to minimize stray light.

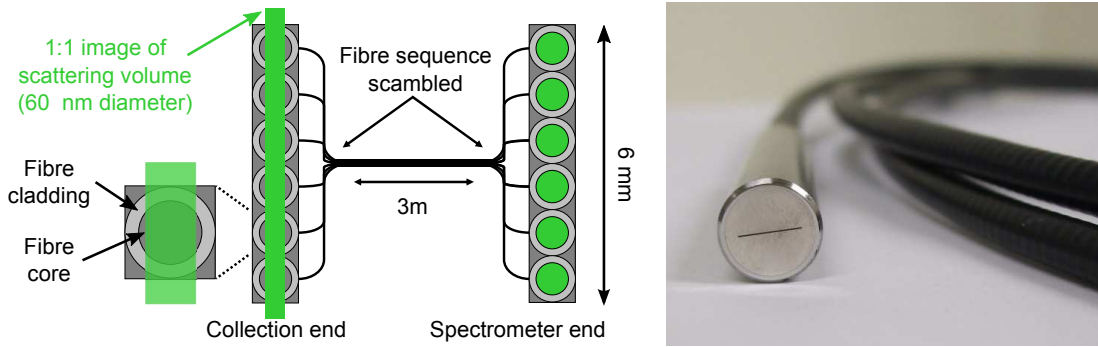


Figure 4.8: Optical fibres. The 48 optical fibres are aligned at both ends along a line. The core of each individual optical fibre is $100\ \mu\text{m}$ in diameter and surrounded by a cladding that increases the total diameter to $125\ \mu\text{m}$. *Left:* Schematic drawing of fibres and projection of scattering region on fibres. The scattering region is imaged 1:1 on the fibres. (According to [Lew07]). *Right:* Front view of fibres which are mounted in a cylindrical sleeve.

4.3.5 The collection optics

The collection optics consist of two planoconvex lenses (75 mm focal length and 2" = 50.8 mm diameter) and the optical fibre (shown in figure 4.2). 2" optics were chosen instead of normal 1" in order to increase the amount of collected light. The first lens is focused on the centre position of the cell for maximum light collection. The second lens is used to focus the scattered light on the 48 optical fibres which are aligned along a horizontal line (figure 4.8). In doing so an about 6 mm long part of the beam path inside the LARA cell is imaged one-to-one on the fibres. The fibres are aligned along a line on the output side as well.

4.3.6 The spectrographs: Spectra Pro 500i and HTS

Several spectrographs can be used within the LARA2 setup for wavelength analysis of the scattered light: The SpectraPro 500i (Princeton Instruments⁶), the HTS lens spectrograph (Princeton Instruments) and the Triax320 (Horiba⁷). The SpectraPro 500i and the Triax320 are Czerny-Turner spectrographs, i.e. they use curved mirrors for guidance and focusing of the light. The HTS uses lenses for focusing. A typical design of both types of spectrographs is shown in figure 4.9. The specifications of the spectrographs at TLK are summarised in table 4.2.

⁶Princeton Instruments, New Jersey, US

⁷Horiba, Kyoto, Japan

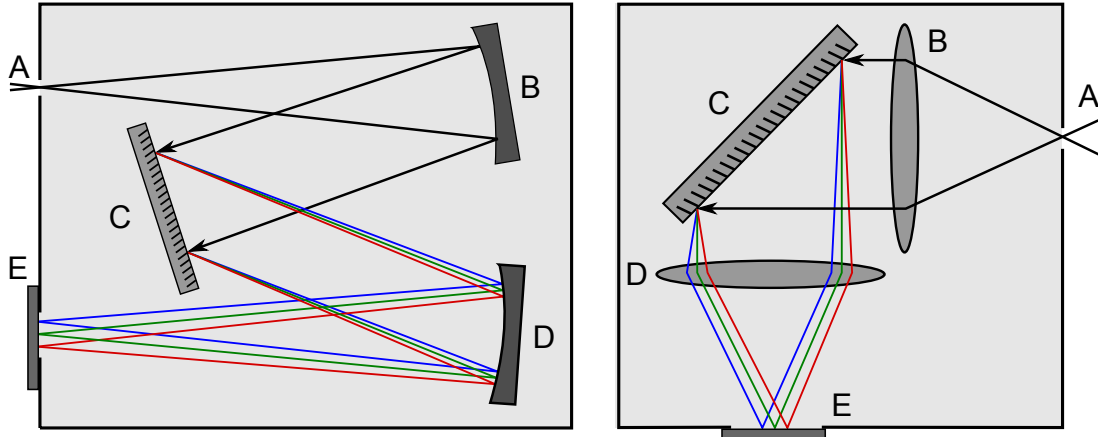


Figure 4.9: Top view of Czerny-Turner spectrograph (left) and transmitting spectrograph (right). Both types of spectrograph have a vertical entrance slit (A), an diffraction grating (C) and a focal plane (E) where the camera sensor is placed. The optics for bundling the light (B) and for focusing (D) differ for the two types: The Czerny-Turner uses mirrors, the transmitting spectrograph uses lenses. Both types of spectrographs decompose the incident light along the horizontal axis of the focal plane.

Table 4.2: Specifications of available spectrographs at TLK based on [Spe00], [Tri02], [ACT05].

Property	SP500	Triax320	HTS
Spectrograph type	Imaging Czerny-Turner		Transmitting optics
Focal length [mm]	500	320	85
f-number	6.5	4.1	1.8
Optical gratings [grooves/mm]	150, 600, 2400	300, 600, 1800	600

The SpectraPro 500i (commonly called SP500) was used as the standard spectrograph for LARA2 since the HTS is usually used in the LARA1 setup and a distortion of one of the internal mirrors of the Triax320 was recognized during test measurements. Its major differences to the HTS are the higher f-number and the variety of optical gratings.

- The f-number $f/\#$ which is a measure for the solid acceptance angle Ω

$$\Omega = \left(\frac{1}{f/\#} \right)^2 \quad (4.1)$$

indicates the amount of light collected by the spectrograph. Hence the light strength of the SP500 ($f/\#=6.5$) is about 8 % compared to the HTS ($f/\#=1.8$). This yields to significant lower signal-to-noise ratio (SNR) within the same acquisition time or accordingly longer acquisition times in order to reach the same

SNR. Nevertheless, this is no mayor concern, since systematic studies of the setup can also be performed with a reduced light yield. If high SNRs are required the acquisition time can be extended.

- The HTS has a fixed optical grating with 600 grooves/mm, the SP500 as has three gratings (150, 600 and 2400 grooves/mm) mounted on an automatically rotatable turret. This turret allows the fast and easy change of gratings and setting of the centre wavelength of the recorded Raman spectrum.

The SP500 has a vertical entrance slit with variable slit width. For normal operation the slit width is set to 100-125 μm as compromise between spectral resolution and light throughput. For wavelength calibration a smaller slit can be used to increase the resolution of the spectrometer. In front of the entrance slit a Semrock RazorEdge filter is placed for suppression of the laser line by $10^8 - 10^9$. Without such a filter, the intense laser line would cause disturbing reflections inside the spectrometer and hence increase the background level in the Raman spectra.

4.3.7 The CCD detectors: PIXIS:400B and PIXIS:2kB

Two CCDs are available at TLK and can be installed in the LARA2 setup for the detection of the scattered light: The PIXIS:400B and the PIXIS:2kB which belong to the same series of scientific grade CCD detectors from Princeton Instruments. The PIXIS:400B is the standard CCD of the LARA2 setup while the PIXIS:2kB is usually used in the LARA1 setup and was already described in detail in [Sch09]. Both CCDs are cooled down to $-75\text{ }^\circ\text{C}$ via Peltier elements to reduce dark noise. The maximum of the quantum efficiency of the CCDs, i.e. the probability that an incoming photon produces an electron in the CCD, fits well to the Raman spectra of hydrogen isotopologues (see figure 4.10). The properties of the PIXIS:2kB are in general better than the PIXIS:400B when taking the larger number of pixels into account (see figure 4.3). The PIXIS400B was chosen for the LARA2 setup because it still easily fulfils the requirements for the tasks stated in section 4.1 but costs significantly less than the PIXIS:2kB.

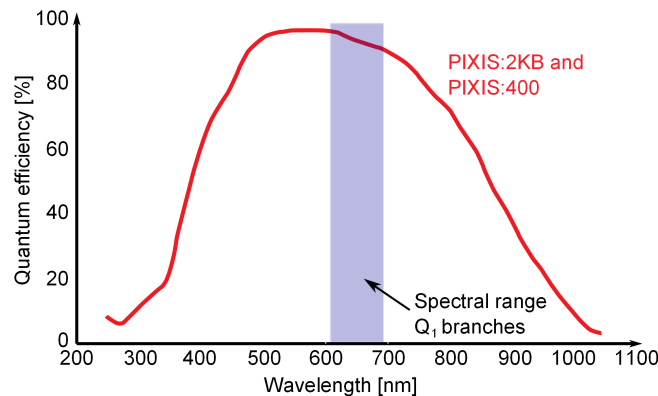


Figure 4.10: Quantum efficiency of PIXIS cameras. Plot of the quantum efficiency of the PIXIS CCDs as function of wavelength. Both CCDs have the same quantum efficiency which peaks around 550 nm with a maximum quantum efficiency of about 95%. This fits very well to the spectral range of the Q_1 branches of the hydrogen isotopologues. (According to [PIX07a] and [PIX07b])

Table 4.3: Specifications of PIXIS cameras according to [PIX07a] and [PIX07b].

Property	PIXIS:400B	PIXIS:2kB
CCD type	back-illuminated	
CCD size [pixel]	1340 × 400	2048 × 512
CCD size [mm × mm]	26.8 × 8.0	27.6 × 6.9
Pixel size [$\mu m \times \mu m$]	20 × 20	13.5 × 13.5
Minimum temperature [°C]	-75	
Dark current [e ⁻ / pixel / second]	0.005 - 0.01 (@ -75 °C)	0.001 - 0.006 (@ -70 °C)
Read out noise @ 100 kHz readout [e ⁻ rms]	3.5 - 5	3.5 - 6

4.3.8 Monitoring tools

Several auxiliary components are used for monitoring of parameters of the LARA2 setup, namely laser power, laser position and temperature of the laser head.

PowerMax-USB LM-10 sensor (Coherent⁸)

This component serves three purposes: (i) it is used to safely dump the laser at the end of the beam path, (ii) it measures the laser power within a range of 10 mW to 10 W using a segmented quadrant thermopile detector. The resolution of the power measurement is 1 mW [Pow07]. (iii) the LM-10 sensor can measure the beam position by weighting the power readings of the different quadrant segments. A conservative estimate of the spatial resolution is 0.1 mm although it can be lower depending on the beam profile and size [Reb09]. The experimentally determined resolution of the beam position measurement in vertical and horizontal direction is $\Delta x = \Delta y = 0.015$ mm and thus is better than the stated value of 0.1 mm. The power reading is currently only read out with 10 mW resolution.

The active sensor area is 16 mm in diameter which makes the laser power measurement relatively robust under changes of the laser direction in the order of a few millimetres, so called beam walks. Due to its design as a thermopile sensor the response time of the sensor is of the order of 1-2 seconds which makes it insensitive to faster changes of the laser power.

Photo diode (Thorlabs)

The photo diode is used for a second independent laser power measurement by monitoring the reflection of the laser on a sampling lens (L2) in figure 4.1. The active area of the photo diode is 10 mm in diameter and hence much smaller than the active area of the LM-10 sensor. Therefore this power measurement is more affected by potential beam walks than the measurement using the LM-10 sensor. On the other hand, this sensor has a response time of 45 ns [Pho06] which makes it suitable to track laser

⁸Coherent, Dieburg, Germany

variations with frequencies above 1 Hz. A glass diffuser plate is placed in front of the photo diode to remove interference patterns of the reflected light on the active area of the photo diode that might influence the power measurement.

Platinum resistance thermometer Pt1000

This sensor is used to measure temperatures, e.g. on the laser heat sink, based on the measurement of the temperature dependent electrical resistance of platinum.

Webcam monitor

A standard webcam (Logitech⁹ QuickCam E5300) was modified for beam position monitoring and beam profiling. It is not installed during normal operation of the LARA2 setup but can be used for beam position monitoring. It is used in Appendix C to characterise the beam walk which is induced by the rotation of the wave plates.

The standard optics in front of the optical sensor of the webcam were removed and the beam is directly focused on the sensor area which has 640×480 pixels. The pixel size is stated to be $2.2 \times 2.2 \mu\text{m}$ [Log10], the interspace between two pixels is not known but estimated to about $2 - 3 \mu\text{m}$ to agree with the total size of the sensor area. Therefore an effective pixel size of about $5 \pm 1 \mu\text{m}$ is assumed in the following. The webcam is easily saturated and therefore the deposited power has to be reduced to about 10 pW, e.g. by operation of the laser at 20mW, monitoring of a reflection of the beam and further reduction by neutral density (ND) filters placed in front of the webcam. The webcam is read out via USB by a LabView program which can store the recorded pictures and fit gaussian profiles to the intensity distribution of the laser spot to determine the beam position in vertical and horizontal direction. The webcam monitor is used in appendix C to measure the displacement of the beam due to the rotation of both $\lambda/2$ wave plates.

4.3.9 Interlock system and data acquisition

The electronics of the LARA2 setup are housed in a box at the front side of the setup which contains an interlock system, a pre-amplifier for the photo diode signal and the shutter control. The interlock system closes the laser shutter if the enclosure of the LARA2 setup is accidentally opened during laser operation or if the photo diode signal drops below a threshold which could indicate the damage a component of the beam path. Detailed information about the interlock system can be found in [Sch09].

An analogue-to-digital converter from NI¹⁰ is used to record the photo diode voltage, the output voltage of the Pt1000 and two further input channels which can be connected, if needed, to additional sensors.

4.3.10 Acquisition and processing software

The LARA2 setup is controlled by a LabView program developed by M. Schlösser [Sch09] that allows automated acquisition and post-processing of Raman spectra which is necessary for continuous operation during later KATRIN neutrino mass measurements. Besides the CCD image the readings of the monitoring tools are stored: Photo diode voltage, laser power and beam position measured by LM-10 and temperature of

⁹Logitech, Apples, Switzerland

¹⁰National Instruments, Austin, Texas, USA

the laser head. Currently, the LM-10 sensor is read-out with 2 decimal digits which reduces the sensor resolution from 1 mW to 10 mW.

The post-processing procedures are split into several subroutines based on the RSK¹¹ toolkit. For detailed information see [RSK10] and [Sch09]:

Astigmatism correction

The spectral lines recorded by the CCD are parabolically bent due to aberration of the optics of the spectrometers. This behaviour is called astigmatism and most pronounced for spectrometers with short focal length like the HTS. The aberration has to be characterised after each change of the settings of the spectrograph. An algorithm based on this characterisation then applies an inverse distortion on the image to get an undisturbed image.

Wavelength calibration

The wavelength calibration of the horizontal axis of the CCD image is done by a reference spectrum with known line positions which has to be measured as well after each change of the settings of the spectrograph. Typically mercury, neon or other hollow cathode lamps are used as reference depending on the region of interest.

Cosmic ray removal

Cosmic rays that pass through the sensor chip of the CCD deposit charge in the pixels nearby. The intensity, i.e. the brightness, of such a pixel can be easily one order of magnitude higher than for a pixel belonging to a dominant spectral line of the Raman spectrum. Therefore these pixels have to be detected and corrected before binning of the CCD image. An algorithm detects these pixels by differentiating along the pixel columns and replaces them by the harmonic mean value of the non-disturbed pixels along the corresponding column.

Binning

Finally, the image is binned i.e. it is averaged along the vertical axis and the Raman spectrum is obtained.

The LARA1 setup was already intensively tested and several systematic effects that influence the measurements were identified [Sch09]. The LARA2 setup can be used to confirm these results and check if the effects are caused by the design of the setup in general or by a specific component. Currently, the laser seems to have a significant but yet not sufficiently characterised influence on the stability of the system due to drifts and fluctuations of the laser power and the pointing direction. The advanced monitoring tools of LARA2 allow a more detailed investigation of laser stability effects than it was possible before in the LARA1 setup.

The next chapter focuses on measurements concerning the stability of the Excel laser and its influence on the precision of the Raman measurement whereas the chapter 6 is dedicated to first measurements of the molecule specific a and γ factors which are necessary for a precise calculation of line intensities in theoretical spectra.

¹¹Raman spectroscopy for KATRIN

Chapter 5

Investigations of laser stability

The aim of Laser Raman spectroscopy for KATRIN is the continuous monitoring of the gas composition in the WGTS during the 60 days long KATRIN neutrino mass measurement runs. The required precision, i.e. the reproducibility, of the LARA measurement of $\Delta I = 10^{-3}$ shall be achieved within sampling intervals of less than 300 s.

The precision

$$\Delta I = \frac{\sigma}{I_{\text{aver.}}} \quad (5.1)$$

is thereby defined by the temporal fluctuation of the measured intensity I , given by the standard deviation σ of the fluctuation, around an average value $I_{\text{aver.}}$.

In order to fulfil these challenging requirements, disturbing influences on the LARA system have to be identified and eliminated or - if an elimination is not possible - well understood and the data corrected for afterwards.

The LARA1 setup was already intensively tested, a method of quantitative analysis was developed and sources of systematic effects have been identified [Sch09]. The major results of [Sch09], that are relevant for this thesis, are:

- It has been shown that a basic quantitative analysis of Raman spectra should be based on the Q_1 branches due to their large intensity and only small overlaps with other lines. The peak intensities can be determined more precisely by the evaluation of the peak area than of the peak height.

An advanced analysis procedure, the so-called Indirect Hard Modelling (IHM), was suggested and tested as well and shall be used for the actual LARA measurements for KATRIN. This method simultaneously fits theoretically calculated Raman spectra of all hydrogen isotopologues on the measured spectra and determines the composition by the weighting parameters of the fit. It is expected that this method allows to increase the precision of the measurement because it takes the whole spectrum into account.

Since the IHM analysis is still under development, the basic analysis, based on the evaluation of the peak areas of the Q_1 branches, is used for quantitative analysis of Raman spectra in this thesis.

- Variations of the laser power were observed but can be taken into account by using relative peak intensities instead of absolute peak intensities. The relative peak intensity is calculated by normalising the absolute peak intensity on the sum of all absolute peak intensities in the composition. A variation of the laser power affects all absolute peak intensities equally and hence will be less present in the relative intensities.

Nevertheless, the laser power should be kept stable on a high level since the signal-to-noise ratios of the peaks in a Raman spectrum increase with increasing laser power.

- Instabilities of the laser pointing were suggested to explain an observed drop of the absolute peak intensities of 22 % [Sch09]. The LARA setup is very sensitive to vertical movements of the beam in the LARA cell due to the narrow region from which the scattered light is collected by the collection optics (see figure 4.8).

5.1 Importance of laser stability for KATRIN

The stability of the laser is one of the key parameters to achieve 0.1 % precision with the KATRIN LARA setup. Although many influences in the LARA setup have been already identified, the laser stability is currently not sufficiently characterised. A study of the influence of beam pointing instabilities on the relative intensities should be performed since first indications for pointing instabilities were found in [Sch09]. The lasers in both LARA setups belong to the class of diode pumped solid state (DPSS) lasers. An influence of temperature variations of the LARA2 setup on the laser parameters can be expected since temperature variations cause thermal drifts of the optical components of the laser cavity and hence influence the laser. The impact on the precision in long term measurements should be characterised.

The operation of the LARA systems at the appendix of the ISS glove box also induces further possible sources of disturbances due to the large number of active components, e.g. pumps, magnetic valves, in and around the ISS glove box.

A series of measurements with LARA2 were performed within the scope of this thesis addressing the mentioned possible sources of disturbances on the laser system. Although the lasers of the two LARA systems are not identical, most of the findings from the measurements with LARA2 should be also valid in general for the laser of LARA1 due to its similar design.

The aim of the measurements was to investigate the stability of the LARA setup and in particular the laser under conditions which are comparable to later KATRIN neutrino mass measurement runs. The stability of the laser was investigated concerning power stability and pointing stability. The frequency stability of the laser was not considered within this thesis. The emphasis was put on studies of thermal influences on the LARA system and their impact on the precision of the gas composition measurement and the search for sources of laser instabilities. An overview of the performed measurements will be given in section 5.2 before the measurements are discussed in detail in the sections 5.3 - 5.5. The influence of temperature variations on the precision of the measurement is shown in section 5.6. The findings of the measurements will be summarised and the impact on the measurements for KATRIN will be discussed in section 5.7.

5.2 Overview of measurements performed

Three major measurement runs of LARA2 were performed that address the laser stability of the system. In all measurements the LARA cell contained a static gas sample to minimise variations of the gas composition. Observed variations of the Raman signals during the measurements were therefore mainly caused by an effect in the LARA setup itself.

Run#1:

In this run the laser was operated for several hours inside the enclosure of the LARA2 setup. A drop of the Laser power was observed which was caused by an overheating of the laser due to insufficient cooling of the laser base plate. After this measurement a cooling fan was installed at the laser base plate.

Run#2:

A H₂:HD:D₂ mixture in a static LARA cell with about 200 mbar total pressure was continuously monitored for about 8 days in this first long term measurement with LARA2. A periodic variation of the temperature of the laser base plate due to the ventilation system of the laboratory was observed. The temperature variation caused a drift of the vertical beam pointing of the laser. After 8 days of measurement, an optical component in the beam path was destroyed, probably by the disintegration of dust on its surface by the laser beam.

Run#3:

The LARA2 setup was operated at LOOPINO which allowed to monitor a gas sample with 217 mbar total pressure and about 90 % T₂ concentration for about 15 days. Besides the impact of temperature variations of the laboratory on the LARA2 setup a periodic disturbance of the laser beam was observed. It can be shown that this disturbance is perfectly correlated in time with an automatic flushing of the glove box atmosphere with gaseous nitrogen¹.

5.3 Run#1: Operation without active base plate cooling

5.3.1 Experimental setup

A schematic drawing of the experimental setup is shown in figure 5.1 and the parameters of the main components are stated in table 5.1. The differences to the standard design of LARA2 (shown in figure 4.1) are the additional mirrors M4 and M5, the position of the photo diode (PD) and the not yet installed cooling fan. The high resolution grating with 2400 grooves/mm at a centre wavelength of 632.8 nm is used to monitor the individual Q₁ branches of D₂.

The H₂:HD:T₂ gas mixture is non-equilibrated, i.e. it is not in thermodynamical equilibrium and the concentrations of the three isotopologues hence deviate from the expected 1:2:1 distribution.

¹The glove box atmosphere is filled with nitrogen to prevent the formation of a flammable gas mixture. The glove box atmosphere is flushed with fresh nitrogen gas when the oxygen concentration reaches 3 %.

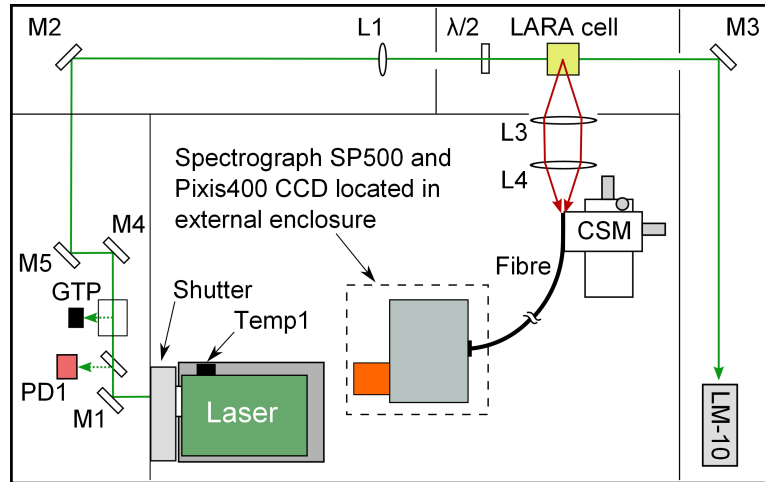


Figure 5.1: Experimental setup of LARA2 of Run#1. The LARA cell is placed directly on the breadboard and not connected to a loop. A Glan-Taylor-Polariser (GTP) is placed at the beginning of the beam path to remove any vertical polarization component from the laser light: The horizontally polarised component can pass the GTP while the vertical component is split off and dumped. The $\lambda/2$ wave plate is used to turn the polarisation direction from horizontal to vertical direction. The temperature of the laser base plate (Temp1) is monitored with the Pt1000 sensor. The scattered light is analysed with the SP500 spectrometer and the Pixis400 camera that are placed in the external enclosure.

Table 5.1: Parameters of Run#1

Location	Room 174 “Warmes Labor 1”
Gas mixture, operation mode	H ₂ :HD:T ₂ (non-equilibrated) with about 200 mbar total pressure, static cell outside of glove box.
Spectrometer (slit width, grating, central wavelength)	SP500, 125 μm , 2400 grooves/mm, 632.8 nm
CCD (Temperature, read-out speed, gain)	Pixis 400B, -72.5°C, 100 kHz, gain 3
Acquisition time per spectrum	600 s
Laser:	Power set point 2 W, laser warmed up for 30 min with open enclosure

5.3.2 Measurement and analysis procedure

After a 30 minutes long warm-up of the laser with open enclosure of LARA2, the enclosure was closed and the measurement started. The system was operated for about 10 hours until an overheating of the laser was observed, indicated by a flashing LED in the laser power supply.

The Raman spectra were not evaluated further due to the large instabilities of the Excel laser. The laser parameters during the overheating are discussed in the next subsection.

5.3.3 Discussion of Results

The laser parameters (base plate temperature, beam position and laser power) are plotted in figure 5.2 and indicate a rise of the base plate temperature up to 47 °C in the first 4 hours of operation. The laser power measured by the photo diode and the LM-10 decreases by 26 % and 9 % respectively. The beam position varies in horizontal (x-) direction by about 0.4 mm while the vertical (y-) position exhibits no significant change.

When the base plate temperature reaches 47 °C the laser power is automatically reduced by the power supply to avoid a further heating up and possible damage of the laser. At the same time the beam jumps about 0.6 mm upwards and afterwards starts to move slowly towards its initial position. The horizontal beam position is not explicitly affected by the reduction of the laser power and follows its long term trend.

This measurement shows that the laser can not be operated in the enclosure of LARA2 without an active cooling of the laser base plate. Therefore a cooling fan was mounted at the laser base plate after this measurement. The decreasing of the laser power during the first 4 hours could be caused by the continuous heating up of the laser base plate but is not proven. The about three times stronger decrease of the photo diode voltage compared to the power reading of the LM-10 sensor has to be further investigated. An offset in one of the sensor readings could explain the different strength of decrease but is improbable due to the shown linearity of photo diode voltage and laser power and the absolute power calibration of the LM-10 sensor. A more probable hypothesis is a small movement of the reflection of the beam on the active area of the photo diode (9 mm diameter) during the 0.4 mm drift of the horizontal beam position. If the sensitivity of the photo diode slightly varies over its surface this could cause a different laser power reading.

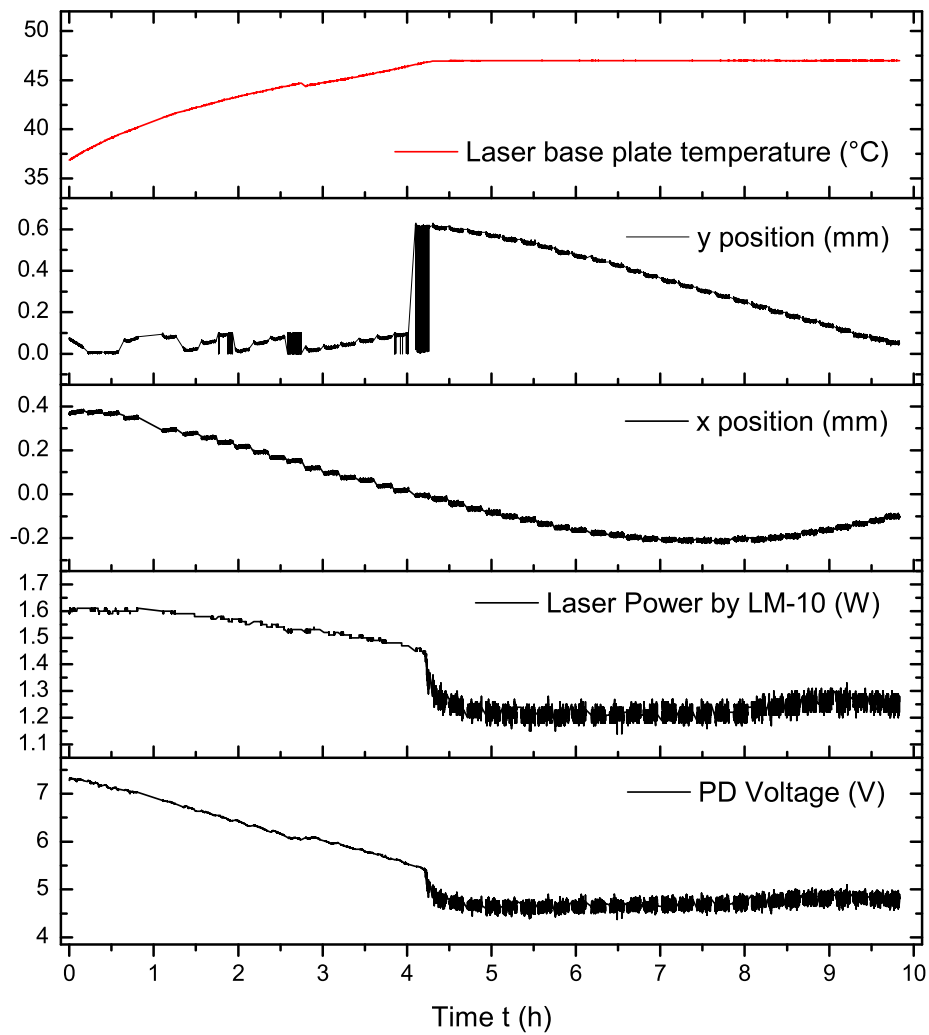


Figure 5.2: Run#1: Overheating of laser due to insufficient base plate cooling. The laser power, measured by photo diode and LM-10 sensor, is automatically reduced by the laser power supply when the laser base plate temperature reaches 47 °C.

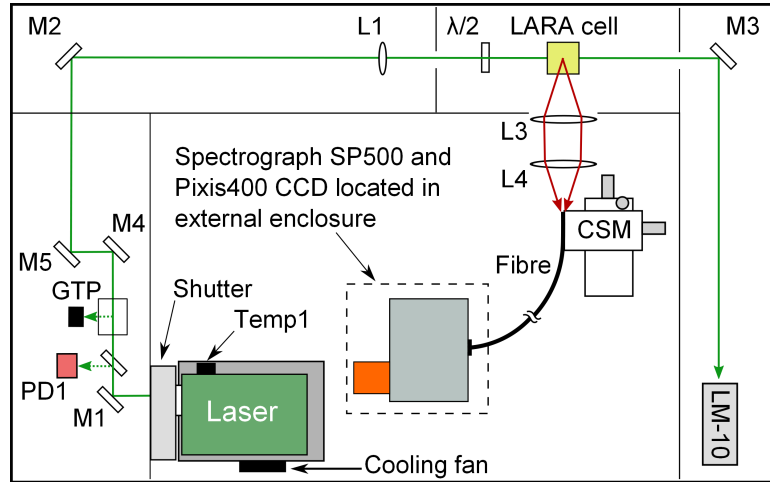


Figure 5.3: Experimental setup of LARA2 of Run#2. In addition to the setup of Run#1 (see figure 5.1), a cooling fan is mounted to the laser base plate.

Table 5.2: Parameters of Run#2

Location	Room 174 “Warmes Labor 1”
Gas mixture, operation mode	H ₂ :HD:D ₂ (non-equilibrated) with about 200 mbar total pressure, partial pressures unknown, static cell outside of glove box.
Spectrometer (slit width, grating, central wavelength)	SP500, 125 μm, 150 grooves/mm, 650 nm
CCD (Temperature, read-out speed, gain)	Pixis 400B, -72.5°C, 100 kHz, gain 3
Acquisition time per spectrum	250 s
Laser:	Power set point 2 W, laser warmed up for 10 min

5.4 Run#2: Long term measurement of H₂, HD and D₂

5.4.1 Experimental setup

The experimental setup of run#2, shown in figure 5.3, is in general identical to the setup of run#1, apart from the now installed cooling fan. The measurement parameters, shown in Table 5.2, were changed: The 150 grooves/mm grating has been used at a centre wavelength of 650 nm to simultaneously monitor the S₀, O₁, Q₁ and S₁ branches of H₂, HD and D₂. The acquisition time was reduced to 250 s which is comparable to typical acquisition times in final KATRIN measurements. The angular position of the λ/2 wave plate was set to transpose the horizontally polarised light into vertically polarised light, in order to maximise the intensity of scattered light towards the collection optics.

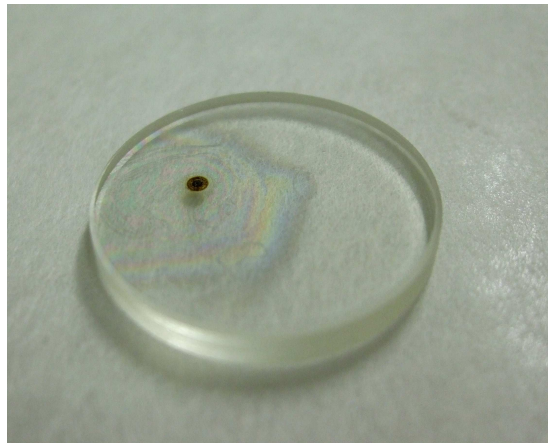


Figure 5.4: Run#2: Wave plate after damage. A spot was burned into the wave plate by the laser beam and the coating was extensively damaged around the spot. The damage is assumed to be triggered by a dust particle on the wave plate that increased the absorption of the intense laser light.

5.4.2 Measurement and analysis procedure

The measurement was started after a 10 minutes long warm-up of the laser. After about 8 days the measurement was aborted due to a damage of the wave plate (see figure 5.4). It is assumed that the damage of the wave plate was triggered by the disintegration of a dust particle on the wave plate by the laser light.

A disturbance in the vertical beam position reading of the LM-10 sensor was observed during the measurement. The sign of the vertical beam position reading was at first occasionally and later more and more often changed until all vertical beam position readings were negative. The disturbance does not seem to correspond to an actual change of the beam position but rather to a malfunction in the electronic systems of the sensor. This feature is discussed in detail in appendix A where it is also shown that the actual vertical beam position can be reconstructed from the data by taking the absolute value of the vertical beam position reading.

5.4.3 Discussion of Results

A representative Raman spectrum of run#2 is shown in figure 5.5. The absolute and relative intensities of the Q_1 branches of H_2 , HD and D_2 are shown in figure 5.6 as a function of time. The absolute intensities decrease by 5-10 % in the first 7 days of measurement. Within the last 12 hours before the damage of the wave plate, i.e. in the period $t \approx 7.5 - 8.05$ d, the absolute intensities decrease by more than 20 %. The relative intensities are constant within 0.5 percentage points during first 7.9 days. Only in the last 4 hours before the damage a change of the relative intensities by about 1 percentage point can be observed.

The laser parameters of run#2 are plotted in figure 5.7. The readings of the photo diode and the LM-10 sensor decrease over the full measuring period of about 8 days by 17 % and 14 % respectively. This indication for a drop of the laser power can qualitatively explain the mentioned decrease of the absolute peak intensities although the magnitudes of the decreases differ by a factor of 2-3. In contrast to the absolute

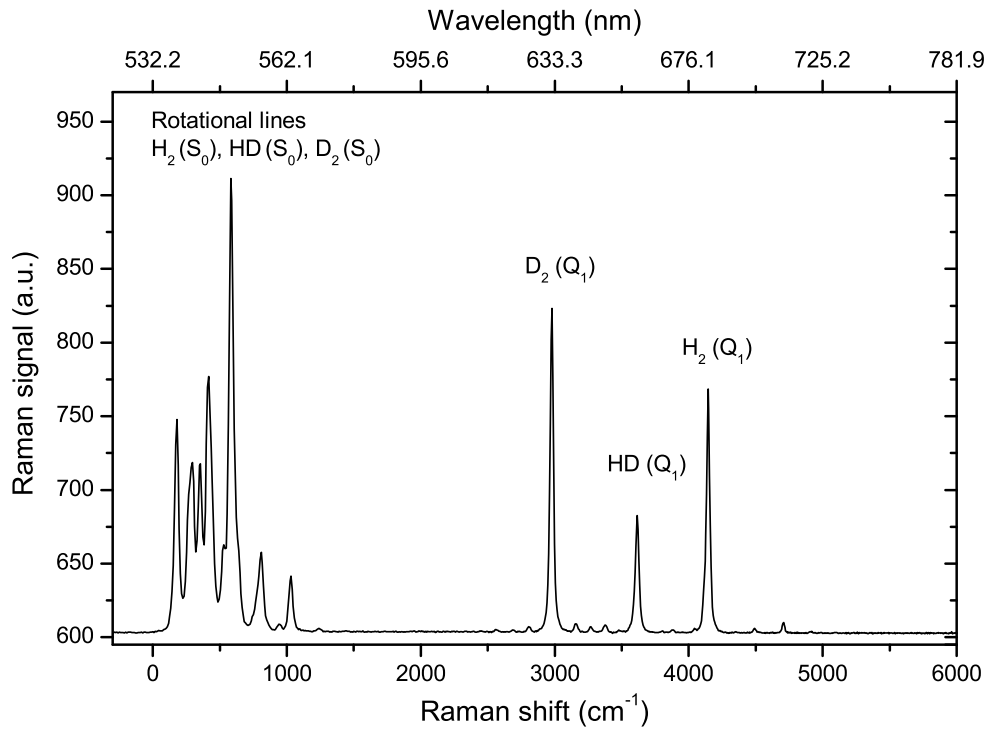


Figure 5.5: Run#2: Spectrum of H₂, HD and D₂. The rotational (S₀) lines of H₂, HD, D₂, located in the first 1500 cm⁻¹ of the spectrum, are strongly overlapping each other. The pure vibrational (Q₁) branches can be nicely identified.

and relative peak intensities, the laser power reading of the LM-10 sensor shows no indication for damage of the wave plate before the moment of the actual damage at $t=8.05$ d when a sudden drop of the laser power was observed.

Combining the early indications of the damage seen in the absolute intensities and the observed sudden drop of the laser power yields to the hypothesis that a dust particle has been stuck to the wave plate at least 12 hours before the actual damage of the wave plate. The dust particle acted as a nuclei for an increasing absorption and scattering of laser light which caused a decreasing of the laser intensity in the centre region of the LARA cell and hence a drop of the absolute peak intensities. The absorption due to the dust particle and the disintegration of the wave plate material increased until the wave plate was damaged by an abrupt runaway reaction.

After the discussion of the destruction of the wave plate, the period $t = 0 - 7.5$ d will be investigated now in detail. The continuing rise of the laser base plate temperature in the first 4 hours of run#2 indicates that a much longer warm-up time is needed for LARA2 than the “typical” warm-up time of 10 minutes stated in table 4.1. The beam pointing in vertical direction is strongly affected by the rise of the base plate temperature during the warm-up: The beam drifts by 0.2 mm downwards on the LM-10 sensor due to a temperature rise of about 4 K. In horizontal (x-) direction a small but steady drift of the laser beam by 0.1 mm in total is present. The impact of the temperature variations on the horizontal beam position is negligible.

In addition to the warm-up process, the temperature of the laser base plate is also affected by the different modes of the ventilation system of the laboratory. In day mode the whole TLK ventilation system has an air throughput of about 65,000 m³ per

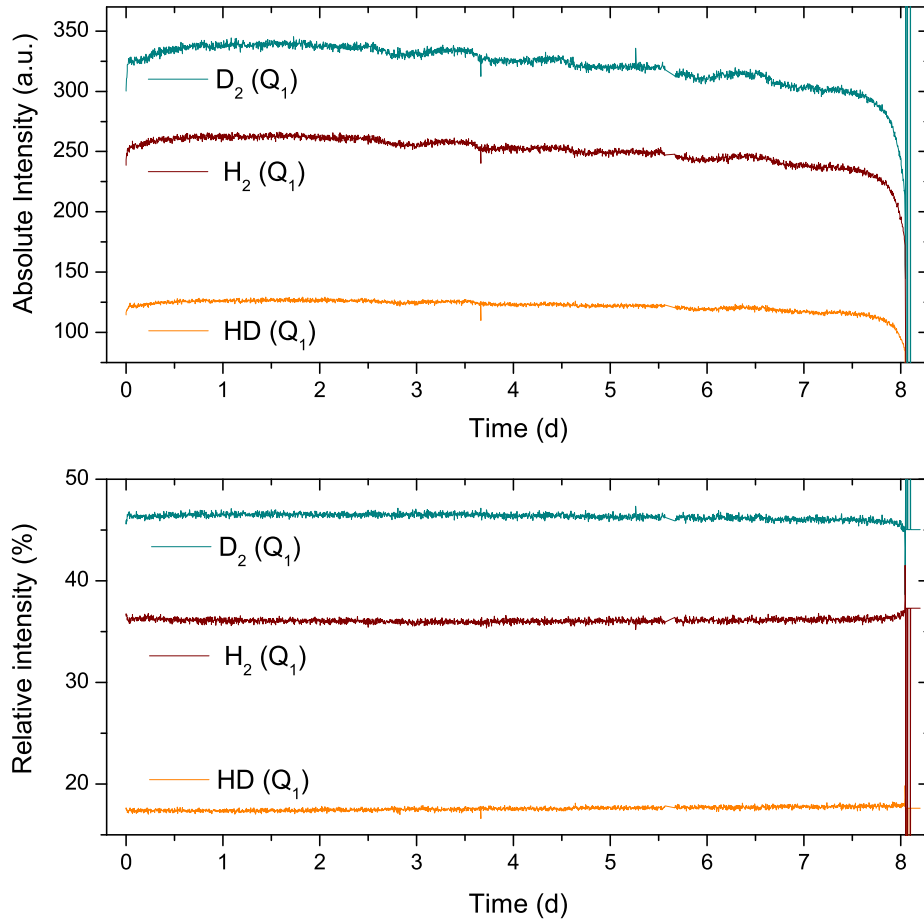


Figure 5.6: Absolute and relative intensities of Run#2. The absolute intensities drop significantly in the last 12 hours before the damage of the wave plate at $t = 8.05$ d while the relative intensities are only affected in the last 4 hours before the damage.

hour and in night mode only of about $35,000 \text{ m}^3$. The transition from night to day mode gradually occurs from 7:00 to 7:30 and the transition from day to night mode from 18:00 to 18:30. The ventilation system stays in night mode from Friday evening to Monday morning. The correlation of the transition phases and the periodic variations of the laser base plate temperature is shown in figure 5.7. The periodic temperature variations due to the ventilation system are of the order $\pm 0.5 \text{ K}$ and cause a drift of the vertical beam position on the LM-10 sensor of typically $\pm 0.05 \text{ mm}$.

The temperature of the laser base plate never reaches $30 \text{ }^\circ\text{C}$ in run#2. This shows that the cooling fan is sufficient to cool the laser base plate. After solving the issue of overheating the impact of the ventilation system of the laboratory on the laser base plate becomes the most prominent disturbance on the LARA measurements. In section 5.6 the precision achieved in periods of large temperature variations will be compared with periods with vanishing temperature fluctuations.

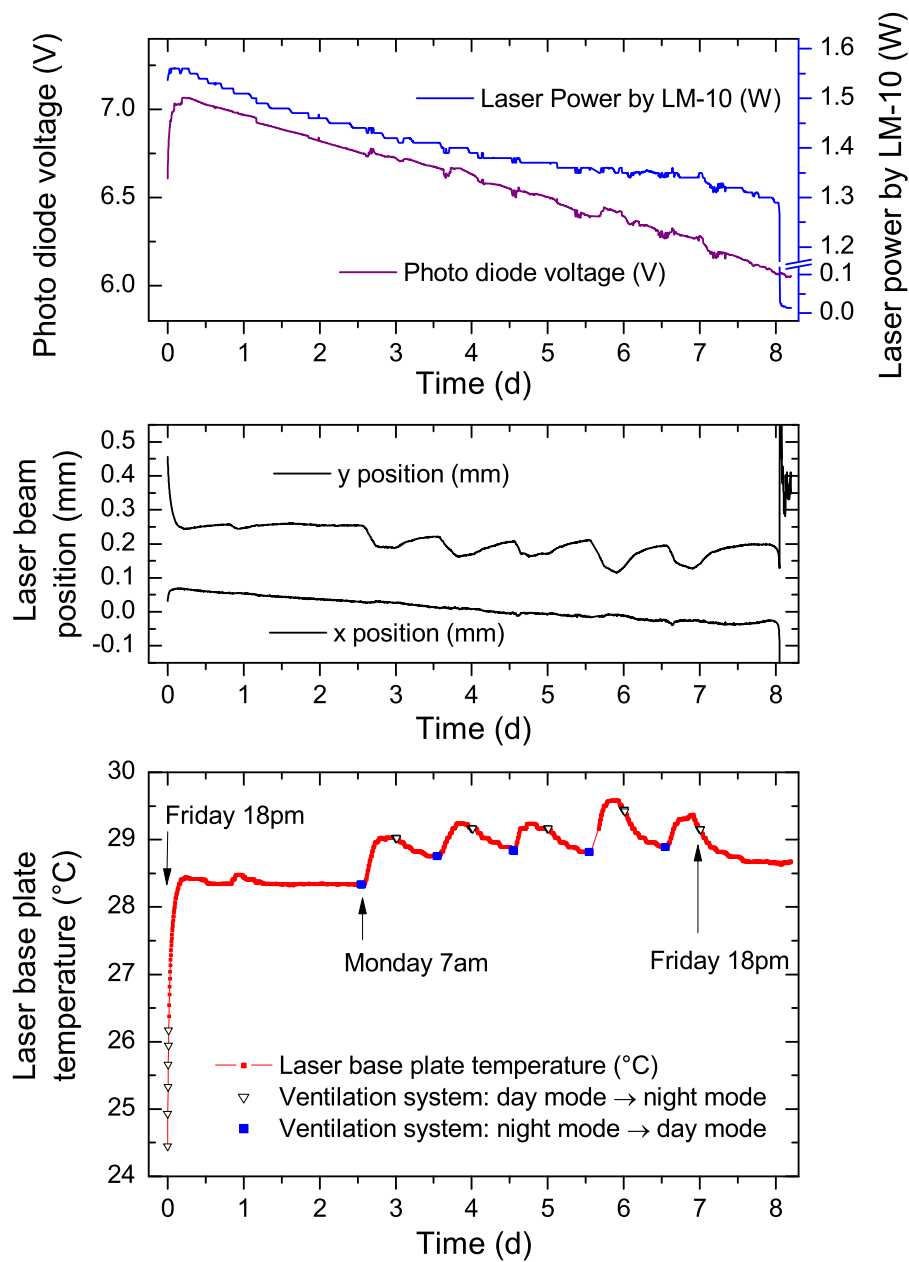


Figure 5.7: Run#2: Laser power, beam position and laser base plate temperature. *Top:* Both laser power readings decrease by comparable amounts but with different temporal behaviour. The photo diode was placed before the wave plate and hence was unaffected of its damage at $t=8.05$ d. The reading of the LM-10 sensor immediately drops after the damage of the wave plate. *Middle and bottom:* The vertical beam position is strongly affected by temperature variations of the laser base plate, e.g. by the initial warm-up of the system ($t = 0 - 0.25$ d) and by the temperature variations due to the different modes of the laboratory ventilation system. The temperature influence on the horizontal beam position is negligible. The transition phases between the day mode of the ventilation system (high air throughput in the laboratory) and night mode (low throughput) are indicated by triangles and squares. During the weekend the ventilation system is set to night mode. The uncertainties of the power measurements (Photo diodes: about 30 mV, LM-10: 10 mW), the beam position measurements (about 0.015 mm) and of the temperature measurement (below 0.5 K) are much lower than the observed trends and therefore not indicated.

Table 5.3: Parameters of Run#3

Location	Operation at LOOPINO
Gas mixture, operation mode	T ₂ gas with 217 mbar total pressure and more than 85 % T ₂ concentration. The other gas constituents are HT, DT and tritiated methanes. The gas has been already circulated for more than 4 weeks in LOOPINO before the valves before and after the LARA cell were closed for the monitoring of a static gas sample.
Spectrometer (slit width, grating, central wavelength)	HTS, 100 μ m, 600 grooves/mm, 659 nm
CCD (Temperature, read-out speed, gain)	Pixis2kB, -75°C, 100 kHz, gain 3
Acquisition time per spectrum	250 s
Laser:	Power set point 2 W

5.5 Run#3: Long term measurement of T₂ at LOOPINO

5.5.1 Experimental setup

Run#3 was done at LOOPINO where a static T₂ sample with 217 mbar total pressure and T₂ concentration of more than 85 % was monitored for 15 days. The remaining gas components were found to be DT, HT and tritiated methanes. The gas has been situated in LOOPINO for about 4 weeks before the start of run#3. An additional photo diode was installed in the optical chain (see figure 5.3) to monitor the laser intensity in front and behind the LARA cell. The pre-amplifier of LARA1 was used to amplify the additional photo diode voltage before digitalisation. The “thick” wave plate, made of mica, was replaced by the “thin” wave plate made of crystalline quartz since it was realised that the “thick” wave plate caused a non-acceptable beam walk when it is rotated. The beam walk caused by both wave plates is characterised in section 6.2 where it is shown that the beam walk due to the “thin” wave plate is negligible. In addition to the thermal sensor on the laser base plate two further temperatures were monitored during the measurement: The temperature of the LARA cell inside the appendix using a second Pt1000 sensor and the laboratory temperature using an uncalibrated thermal sensor in the exhaust air system. The HTS spectrograph was used in combination with the Pixis2kB CCD camera due to the better light yield in comparison to the SP500. The acquisition time was set to 250 s which is comparable to typical acquisition times in later KATRIN measurements. The detailed measurement parameters of run#3 can be found in table 5.3.

The mounting of LARA2 to the appendix and the alignment of the setup took about one day which is significantly more than the typical time needed for setting up the system with a free standing LARA cell.

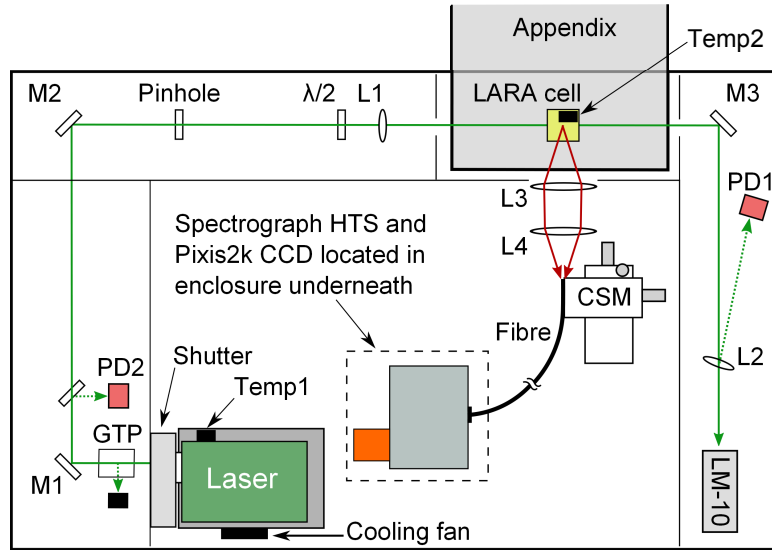


Figure 5.8: Experimental setup of LARA2 of Run#3 The LARA cell is connected to LOOPINO inside the appendix. The laser power is measured by two photo diodes (PD1, PD2) and by the LM-10 sensor. The pinhole is used as reference for alignment purposes but is fully opened during measurements. The temperature of the laser base plate (Temp1) and of the LARA cell inside the appendix (Temp2) are monitored with Pt1000 sensors. The scattered light is analysed with the HTS spectrometer and the Pixis2k camera that are placed in the enclosure underneath the breadboard.

5.5.2 Measurement procedure and analysis

The measurement was started without warming up of the laser. Note that the laser shutter was closed during 4 subsequent acquisitions ($t = 4.08 - 4.10$ d) because the setup had to be opened due to technical reasons. The acquisitions associated with this period of interruption were excluded from the data evaluation procedure.

5.5.3 Discussion of Results

A typical spectrum acquired during run#3 is shown in figure 5.9. The Q_1 and O_1 and S_1 branches of T_2 and the Q_1 branches of HT and DT can be identified although the overlap of the Q_1 branch of DT with the S_1 ($J''=2$) branch of T_2 has to be considered. The line position of the T_2 (S_1) $J''=5$ line deviates by 9 cm^{-1} from theoretical data [Lew07] while all other lines agree within 5 cm^{-1} . This discrepancy will be further investigated. The achieved spectral resolution, given by the full width half maximum (FWHM) of the T_2 (Q_1) line, is better than 1 cm^{-1} .

Several strongly overlapping lines can be found between 1500 and 2000 wave numbers. It is assumed that these lines belong to deuterated and tritiated species of methane, i.e. CT_4 , CDT_3 , CD_2T_2 , etc., that were formed by the interaction of tritium with the stainless steel tube walls of LOOPINO. The formation of deuterated and tritiated methane species in the presence of stainless steel is a known process [Mor77] and can be expected for this gas mixture due to the more than 4 weeks long storage period of the tritium gas in LOOPINO. An unambiguous identification of the lines by comparison with known line positions of deuterated and tritiated methane species [Eng92] was not possible since the individual lines cannot be resolved with the used combination of

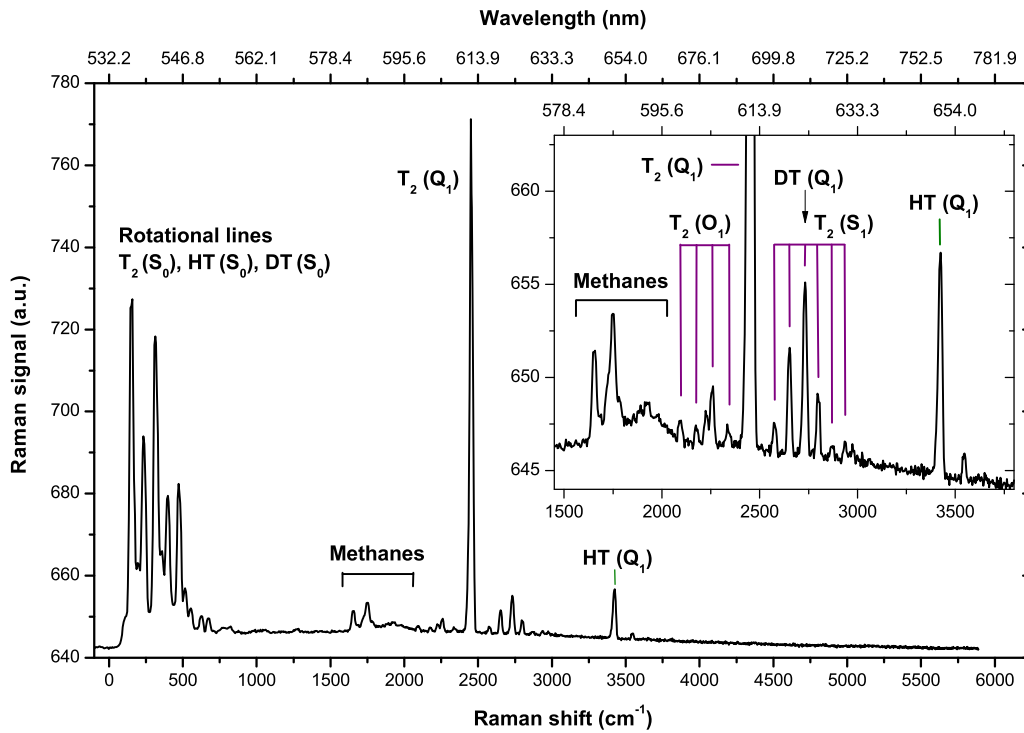


Figure 5.9: Run#3: Spectrum of T₂, DT and HT taken at LOOPINO. The Q₁ branch of T₂ dominates the spectrum due to the high T₂ concentration of about 90 %. Several O₁ and S₁ lines of T₂ can be identified, the line positions typically agree with the theoretical data [Lew07] within 5 cm⁻¹. The Q₁ branch of DT overlaps with the S₁ (J^{''}=2) branch of T₂ as already shown in figure 3.9. The lines between 1500 and 2000 cm⁻¹ probably belong to tritiated methanes, e.g. CT₄, CDT₃. A definite identification is not possible with the chosen optical grating due to the narrow spacing of the lines and large overlaps in the spectrum. The tritiated methanes were formed by interactions of the tritium gas with the stainless steel tube walls of LOOPINO.

spectrograph and CCD. A dedicated study of tritiated methanes will be performed in the future using the high resolution grating of the SP500 spectrograph.

The absolute and relative intensities of the Q₁ branches of T₂, DT and HT as a function of time are plotted in figure 5.10. It has to be kept in mind that also the S₁ (J^{''}=2) line of T₂ contributes to the absolute and relative intensity of the Q₁ branch of DT. Other hydrogen isotopologues were not considered for the calculation of relative intensities since no contribution in the spectrum could be observed. The lines of the methane species were ignored as well because the strong overlaps prevented a robust peak fit. Although variations of the laser power are compensated by the calculation of relative intensities, a distinct variation of the relative intensities is observed. In addition, pronounced drops of the absolute intensities around t ≈ 8 d and t ≈ 13.2 d are observed. Major changes of the gas composition causing such fluctuations can be excluded since valves of the LARA cell were closed during the measurement.

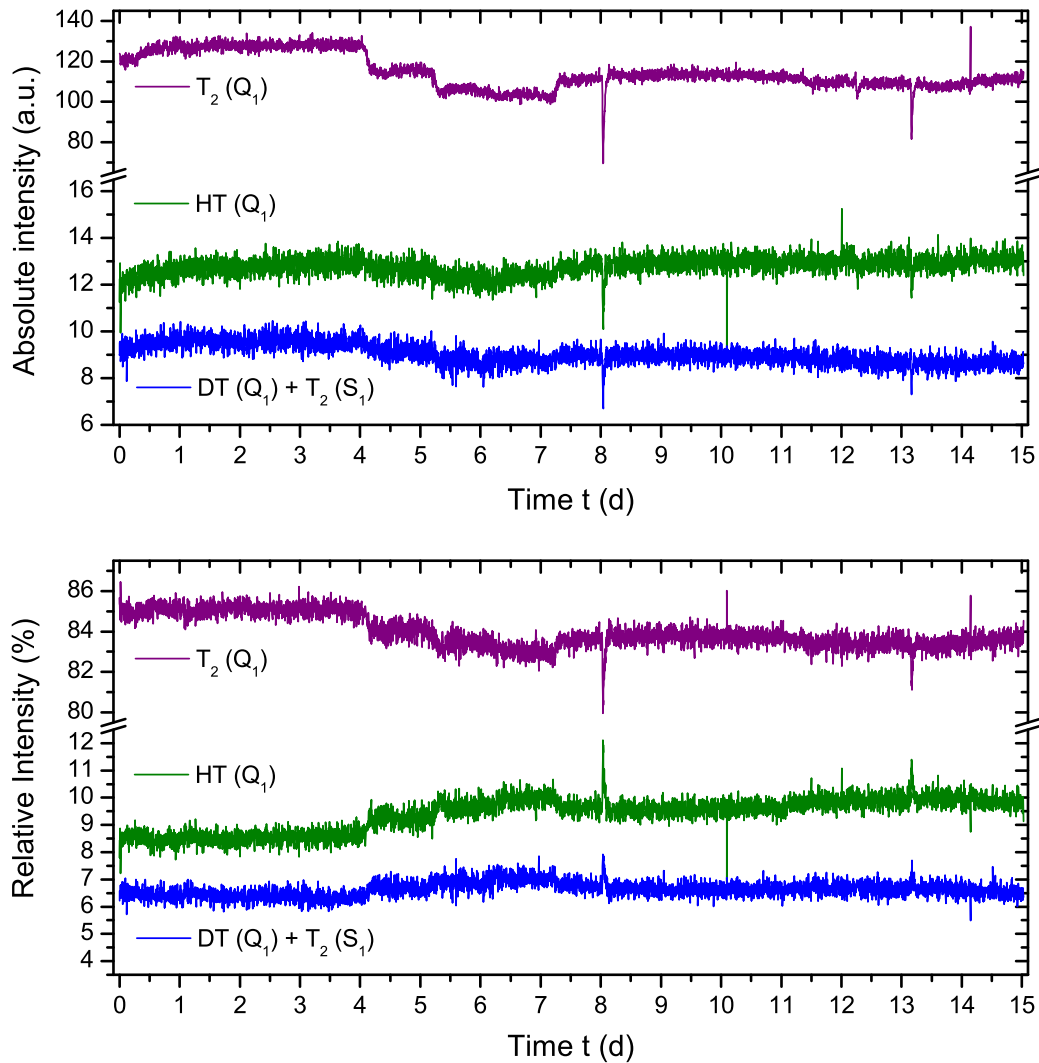


Figure 5.10: Absolute and relative intensities of T_2 , DT and HT. Due to the overlap of the Q_1 branch of DT and the S_1 ($J''=2$) branch of T_2 only the intensity of both can be given. The relative intensities were calculated by normalizing the absolute intensities on the sum of all three intensities. Note the break in the y-axis in both diagrams.

The laser parameters, shown in figure 5.11, reveal several features. An overview is given before the features are discussed in detail in the following subsections.

- **Periodic disturbance of laser power and beam position**

The horizontal beam position reading and the photo diode 1 voltage are disturbed by a periodic, peak like feature on top of their long term trends. About five peaks per day are observed. This type of disturbance was also observed during measurements with the LARA1 setup in December 2009 and January 2010. The disturbance of the laser power and position reading is perfectly correlated in time with the regular flushing of the ISS glove box atmosphere with nitrogen gas. The hardware component that causes this disturbance and the transmission path of the disturbance is currently unknown.

- **Temperature profiles of laser base plate**

The laser base plate needs nearly 0.5 days to reach a stable temperature of about 30 °C. Temperature variations of up to 4 K were detected during run#3. The temperatures of the laser base plate and of the LARA cell are influenced by temperature variations of the laboratory.

- **Correlation of beam position with base plate temperature**

The vertical and the horizontal beam position are correlated with the laser base plate temperature but with different strength. The observed beam-walk in the interval $t = 4$ d to $t = 8$ d is a suitable candidate to explain the variations in the relative intensities. For $t \approx 8$ d an abrupt change of vertical and horizontal beam position occurs that is caused by a corresponding drop in temperature.

- **Contradictory trends of laser power readings and correlation with laser base plate temperature**

All laser power readings exhibit two features: A linear long term drift over the full measuring time and a short term variation with smaller amplitude which is correlated with the laser base plate temperature. The linear long term drift of photo diode 1 is increasing while the long term drifts of photo diode 2 and the LM-10 sensor are decreasing. Two of the laser power readings, i.e. the photo diode 2 voltage and the power reading of the LM-10 sensor, decrease continuously while the photo diode 1 voltage increases.

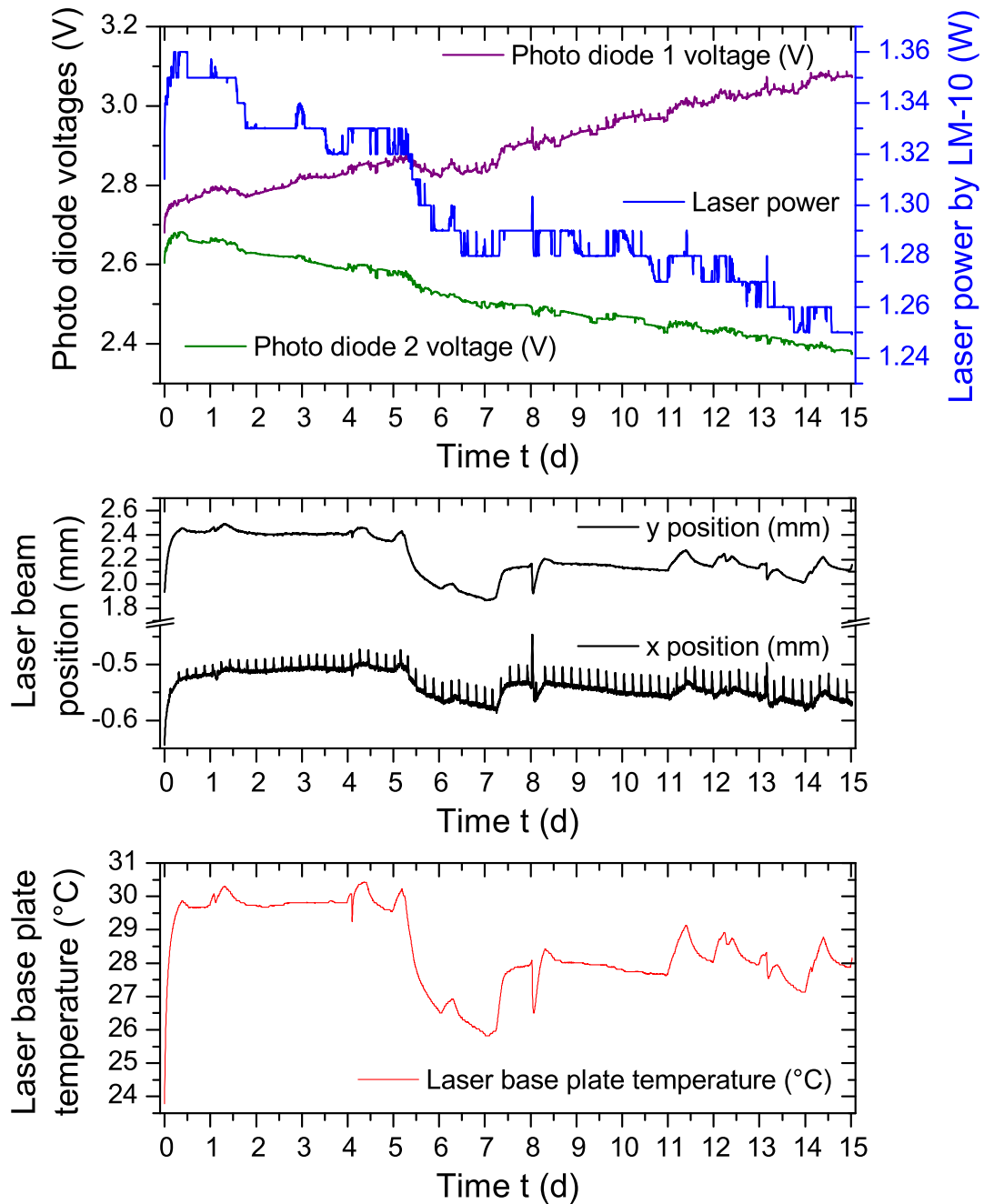


Figure 5.11: Laser power, beam position and laser base plate temperature.

Top: The laser power measured by two photo diodes (in volts) and the LM-10 sensor (in watts). The readings of the LM-10 sensor and the photo diode 2 have a similar declining trend while the reading of the photo diode 1 increases. The reading of photo diode 2 additionally has a periodic disturbance on top of the global trend. *Middle and bottom:* The beam position in horizontal and vertical direction measured by the LM-10 sensor. A significant movement of the beam is visible, especially during the warm up of the laser system in the first 12 hours. Both position readings perfectly correlate with the temperature of the laser base plate, however, the vertical position is more affected by the temperature variations. The horizontal position is also periodically and increasingly distorted.

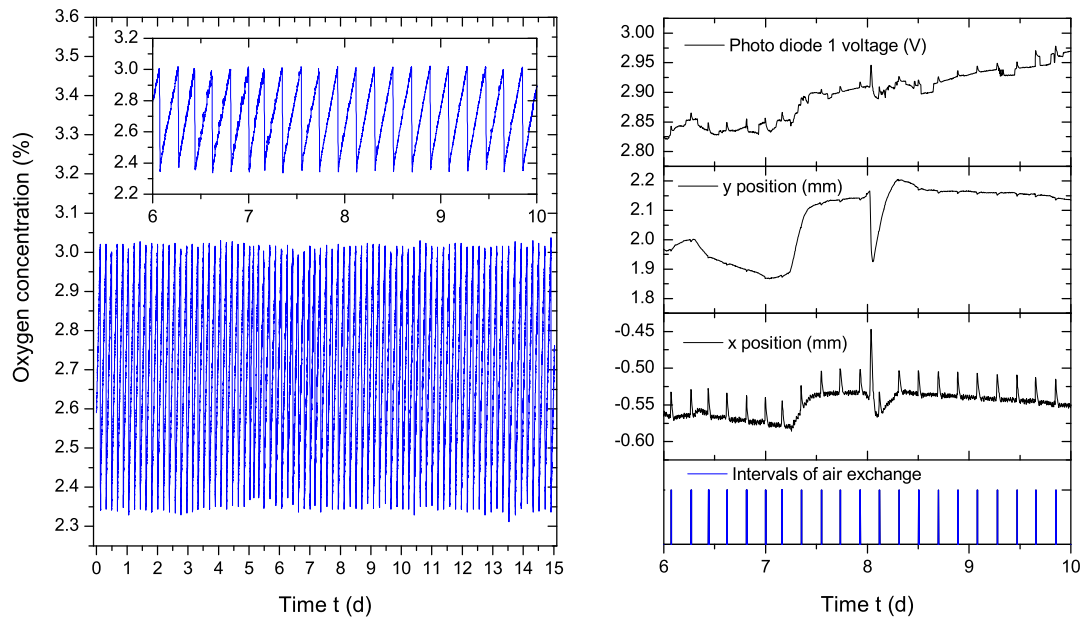


Figure 5.12: Correlation of oxygen concentration in ISS glove box and laser parameters. *Left:* The oxygen concentration in the ISS glove box periodically increases from 2.35 % to 3 % due to minor leaks in the second enclosure. The glove box atmosphere is automatically flushed with nitrogen gas when the concentration reaches 3 % to avoid the formation of a flammable gas mixture. *Right:* The intervals of the exchange of the glove box air perfectly correlate in time with the observed disturbances of the laser parameters, i.e. horizontal beam position and power reading of the photo diode 1. The vertical beam position is also affected but with negligible amplitude.

5.5.3.1 Periodic disturbance of laser power and beam position

Periodic distortions of the photo diode 1 reading the beam position were observed during run#3. A small amount of ambient air continuously enters the ISS glove box due to the about 5 mbar low pressure inside the ISS glove box in comparison to the laboratory and due to the leak rate of the ISS glove box which is below 0.3 Vol.% of the glove box per hour and 1 mbar pressure difference to the laboratory atmosphere². When the oxygen concentration inside the glove box reaches 3 %, the glove box atmosphere is flushed with fresh nitrogen gas to avoid the formation of a flammable gas mixture inside the glove box. The observed periodic disturbances of the laser power reading of photo diode 1 and of the beam position are correlated in time to the regular flushing of the glove box atmosphere with nitrogen gas (see figure 5.12)

Several hardware components of the flushing system, e.g. pumps and magnetic valves, are possible candidates to be the origin of the disturbance. The transmission path of the disturbance is currently also unexplained. A transmission of the disturbance via the power grid can be excluded since no voltage peaks and frequency fluctuations were found in the period of interest. Since the two affected sensors use different measurement principles - the photo diode is a semiconductor device while the LM-10 sensor is a

²Due to its large size, the leak rate of the ISS glove box is allowed to be by a factor of three larger than the maximum leak rate of 0.1 Vol.% per hour and 1 mbar pressure difference of all other glove boxes at TLK.

thermal sensor - a disturbance of the sensors seems improbable and therefore an actual disturbance of the laser is assumed. Further investigations are ongoing to reveal the origin and the transmission path of the disturbance since such kind of disturbance cannot be accepted during KATRIN neutrino mass measurement runs.

5.5.3.2 Temperature profile of laser base plate

The temperature profile of the laser base plate, the LARA cell and the reading of the uncalibrated temperature sensor in the exhaust air system of the laboratory are shown in figure 5.13. The laser base plate is always about 7 K warmer than the LARA cell in the ISS glove box due to the thermal load of the laser. Temperature variations of the laser base plate can be simultaneously seen in the temperature reading of the LARA cell which indicates that the temperature variations are caused by an external parameter which affects both components. Frequent temperature variations are visible from Monday to Friday, when the ventilation system changes 5 times from night to day mode and vice versa.

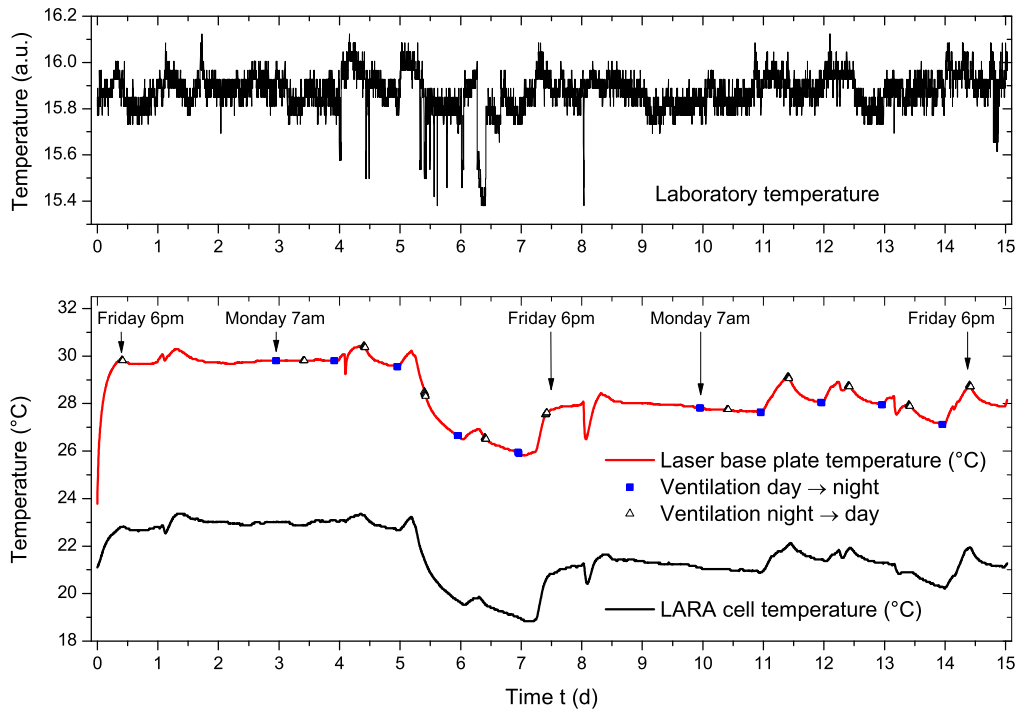


Figure 5.13: Laser baseplate temperature T_{Laser} , LARA cell temperature T_{Cell} and laboratory temperature T_{Lab} . The laser is always about 6 K warmer than the LARA cell inside the ISS glove box due to the thermal load of the laser. The laser needs about 0.5 d to reach a constant base plate temperature. Although the atmosphere inside the ISS glove box is isolated from the outside atmosphere, the trends of T_{Laser} and T_{Cell} are very similar. The two modes of the laboratory ventilation system (the laboratory's air throughput is about 2 times higher in day mode than in night mode) have a significant influence on the laboratory temperature and hence on the laser and the cell. The ventilation system stays in night mode during the weekend. The changes between both modes are indicated for T_{Laser} .

The laser base plate temperature and the temperature of the LARA cell drop by about 4 K during the period $t \approx 5.2 - 7.3$ d. The temperature of the exhaust air strongly fluctuates during the same period. A reason for the temperature drop and fluctuation respectively, e.g. due to the opening of an exterior door of the laboratory or malfunctions of the ventilation system in this period, cannot be found. The temperatures of the laser base plate and the LARA cell are more stable during the weekends when the ventilation system is constantly set to night mode, i.e. low air through put. It will be shown in section 5.6 that the precision of the gas composition measurement significantly decreases in periods with enhanced temperature variations in comparison to periods with stable temperature. A sudden temperature drop at $t \approx 8$ d, which also affected the absolute and relative peak intensities (see figure 5.10), is also present in the reading of the temperature sensor of the exhaust air system indicating a general drop of the temperature in the laboratory. An opening of an exterior door of the laboratory or a sudden drop of the ambient temperature outside of the laboratory, which could explain such a sudden temperature drop, were not found in the corresponding interval.

The ventilation system can be identified as a major influence on the temperature stability of the laser base plate while the origin of the 4 K temperature drop is currently unknown. As it will be shown in the next subsections, the temperature stabilisation of the laser base plate is crucial for the stable and reliable operation of the laser. Therefore further investigations have to be performed to clarify the origin of the temperature variations.

5.5.3.3 Beam position and base plate temperature

A correlation of the beam position with the laser base plate temperature is observed also in this run. The largest variation of beam position occurs in the period $t \approx 4.5 - 7$ d in which also the laser base plate temperature decreases by 4 K: The horizontal beam position changes by about 0.08 mm and the vertical beam position drops about 0.4 mm. In this period also the strongest variations of the absolute and relative peak intensities occur apart from the one-time “event” at $t \approx 8$ d. The impact of the beam pointing instabilities on the precision will be evaluated in detail in section 5.6.

In Appendix B the change of the pointing direction of the laser is estimated which could exclusively explain a beam walk of 0.4 mm. It is shown that laser alone cannot cause such a beam walk under normal circumstances and therefore also the pointing instabilities of other optical components in the beam path, e.g. mirror and lens mounts, have to be considered to explain the observed beam walk. Further investigations on the temperature influence on the stability of the mirror mounts are currently ongoing and indicate that also the mirror mounts are affected by temperature variations.

5.5.3.4 Contradictory trends of laser power readings

All three power readings reveal a linear long term drift over the 15 days of measurement. While the reading of the photo diode 2 (placed at the beginning of the beam path) and the reading of the LM-10 sensor (placed at the very end) decrease by 11 % and 8 % respectively, the reading of the photo diode 1 (placed at the end of the beam path) increases by 12 %. The origin of the linear drifts is currently unknown but does not seem to represent an actual change of the laser power due to the contrary readings. Thermal influences on the read-out electronics, especially on the home-made pre-amplifiers of the photo diodes, could cause a drift of the photo diode voltage. The analogue-to-digital converter which is used to acquire the pre-amplified photo diode voltages can be excluded as the origin of the observed drifts since its precision was experimentally verified on the level of 0.02 %. The test of the stability of the pre-amplifiers is currently ongoing.

On top of the long term linear drifts a smaller, short term variation of the order of 2-3 % is present in each laser power reading which can be easily seen in the plot of the deviations of the fit from the measured data (see figure 5.14). A clear correlation of this short term variation with the laser base plate temperature was found for all three laser power readings indicating that the short term variation is an actual variation of the laser power itself.

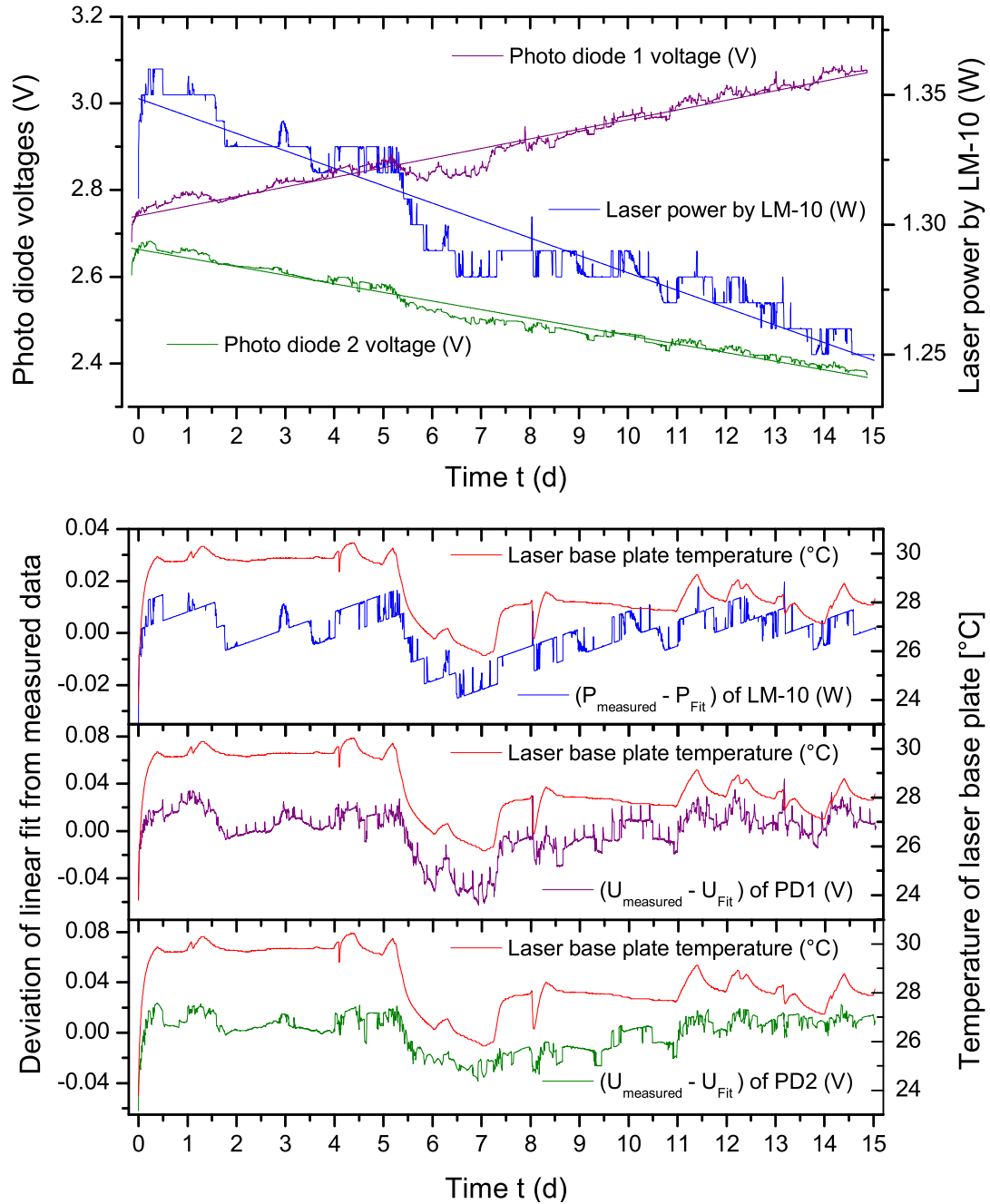


Figure 5.14: Temperature influence on laser power. *Above:* The global trends of all three laser power readings can be approximated by linear functions. *Below:* The deviations of the fits from the measured data are correlated with the of the laser base plate temperature (red). The correlation is the least visible for the laser power reading of the LM-10 sensor due to the limited read-out resolution of the sensor.

Table 5.4: Periods of run#2 and run#3 with specific temperature profile for calculation of precision.

Run	Period	Temperature profile of period
Run#2	I 1.3 - 2.6 d	Stable temperature, $\Delta T \leq 0.06$ K
	II 2.6 - 7.6 d	Temperature fluctuations, $\Delta T = \pm 0.5$ K
Run#3	I 2 - 4 d	Stable temperature, $\Delta T \leq 0.2$ K
	I 4 - 6 d	Temperature drop by $\Delta T = 4$ K
	III 9 - 11 d	Temperature decrease by $\Delta T = 0.3$ K
	IV 11 - 13 d	Temperature fluctuations, $\Delta T = \pm 0.7$ K

5.6 Influence of laser stability on precision in long term measurements

After the detailed discussion of the measurements, the impact of temperature instabilities on the precision of the relative peak intensities will be evaluated for run#2 and run#3. For that purpose both runs are divided into periods with specific temperature profiles according to table 5.4. The precision of the relative peak intensities is calculated according to equation 5.1 for each period.

Achieved precision in run#2

The histograms of the relative peak intensities for the Q_1 branches of H_2 , D_2 and HD in the two periods of run#2 and the calculated precisions are shown in figure 5.15. The precision vary from $4.3 \cdot 10^{-3}$ (D_2 , period I) to $9.3 \cdot 10^{-3}$ (HD, period II). The precision of the Q_1 branch of HD is in both periods worse than the precisions of the Q_1 branches of the two homo-nuclear isotopologues due to the smaller signal-to-noise ratio of the Q_1 branch of HD in the Raman spectra. In general a worsening of the precision of all relative intensities can be observed from period I to period II which is related to the enhanced temperature variations and hence reduced laser stability in period II.

Achieved precision in run#3

In run#3, the precision of the Q_1 branch of T_2 is evaluated for four different periods (see figure 5.16). The achieved precision varies from $3.5 \cdot 10^{-3}$ (period I) to $6.3 \cdot 10^{-3}$ (period II) indicating again the impact of temperature fluctuations and drops respectively on the precision of the relative peak intensity.

For the comparison of the achieved precisions in both runs, several aspects have to be considered:

- In run#2 the total pressure of the gas sample was about 200 mbar with a H_2 and D_2 concentration of approximately 35-40 %. In run#3 the total pressure of the gas sample was 217 mbar with a T_2 concentration of more than 85 %. Therefore the partial pressure of T_2 in run#3 was at least a factor of 2 higher than the partial pressure of H_2 and D_2 , respectively, in run#2. An enhancement of the

signal-to-noise ratio in the spectra of run#3 by a factor of 2 and a corresponding enhancement of the precision can be expected.

- Run#3 was done with the high aperture ($f/\# = 1.4$) HTS spectrograph while run#2 utilised the low aperture ($f/\# = 6.5$) SP500 spectrograph which has a light yield of about 8 % in comparison to the HTS.
- The acquisition time per spectrum was 600 s in run#2 but 250 s in run#3 which reduced the amount of collected light accordingly.
- The observed intensity of the scattered light strongly depends on the alignment of the LARA cell to the laser beam and to the alignment of the collection optics to the LARA cell and therefore typically changes from alignment to alignment. The alignment of the LARA setup to the appendix is more complex than the alignment of the setup with a LARA cell outside of the glove box due to the limited space for auxiliary tools, e.g. pinholes and targets, which allow to check the alignment. A variation of the peak intensity and hence of the achieved precision by a factor of two or even more due to the alignment of the setup cannot be excluded.
- Additional optical components, i.e. the windows of the appendix, were present in the beam path of run#3. Extra optical losses and reflections due to these windows are possible but also depend on the alignment of LARA2 relative to the appendix and are therefore hard to account for.
- The impact of the periodic disturbance in run#3 due to the flushing of the glove box atmosphere on the precision of the measurement cannot currently be quantified.

Considering only the currently quantitatively assessable aspects, i.e. the first three in the list above, an enhancement of the precision by a factor of $2 \cdot 1/(8\%) \cdot 250/600 \approx 11$ is expected for run#3 relative to run#2. The experimentally observed enhancement factor is $8.6 \cdot 10^{-3} / 7.0 \cdot 10^{-3} \approx 1.2$ when comparing the best precisions of both runs. The theoretical and the experimental enhancement factors disagree by a factor of 10, but it has to be kept in mind that the three unaccounted aspects, i.e. influence of alignment on peak intensity, losses and reflections due to the appendix windows and the periodic disturbance, might cause a probable reduction of the theoretical enhancement factor.

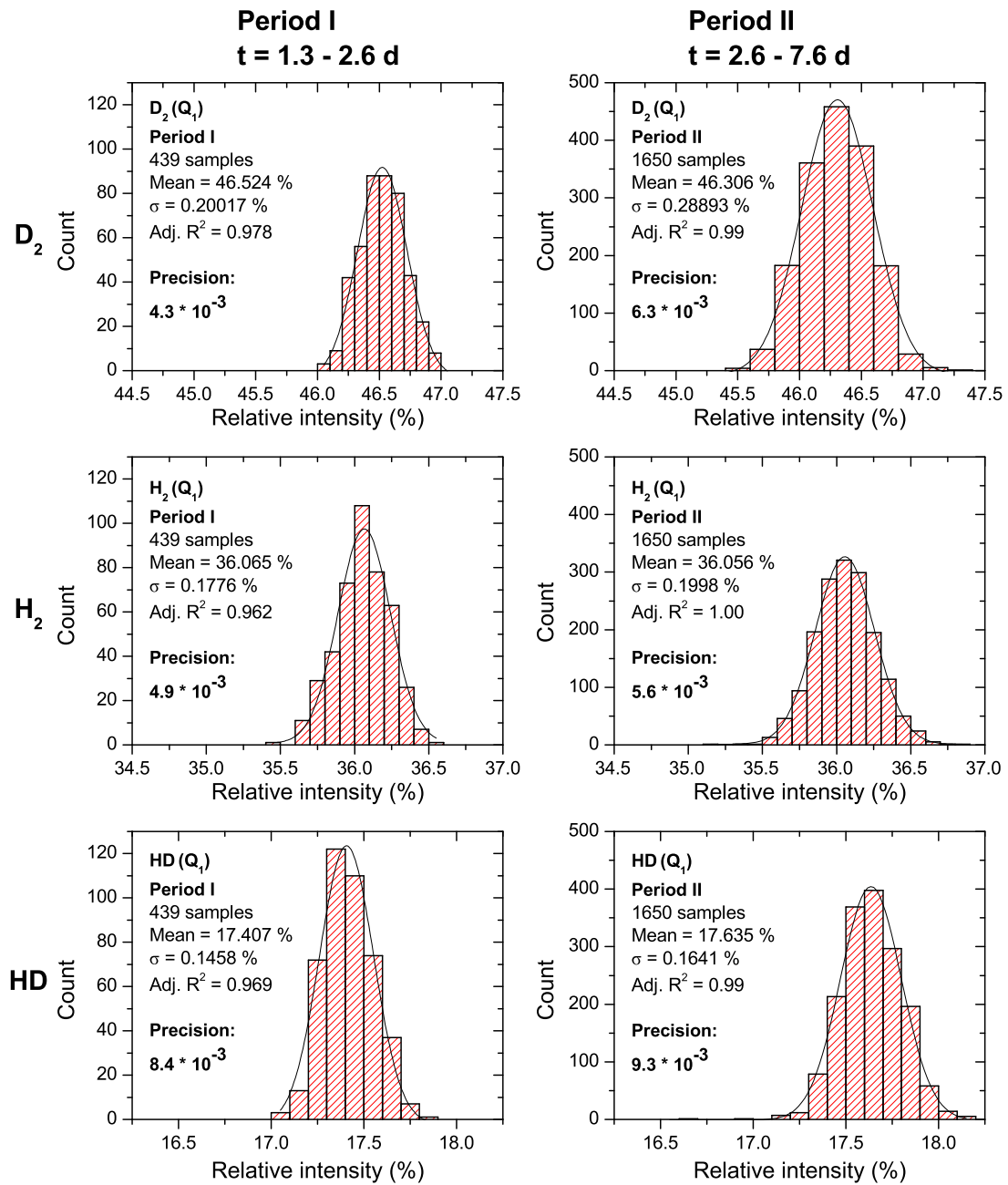


Figure 5.15: Run#2: Achieved precision relative peak intensity of H₂, D₂ and HD. The precisions of the measurements are determined for two periods which have different laser base plate temperature profiles: Constant temperature (period I) and periodic fluctuation of the temperature by about ± 0.5 K (period II). The precision is calculated by dividing the standard deviation σ of the fitted Gaussian by the mean value, i.e. the centre position of the Gaussian. Note that σ is given as absolute value, i.e. in the same units as the mean.

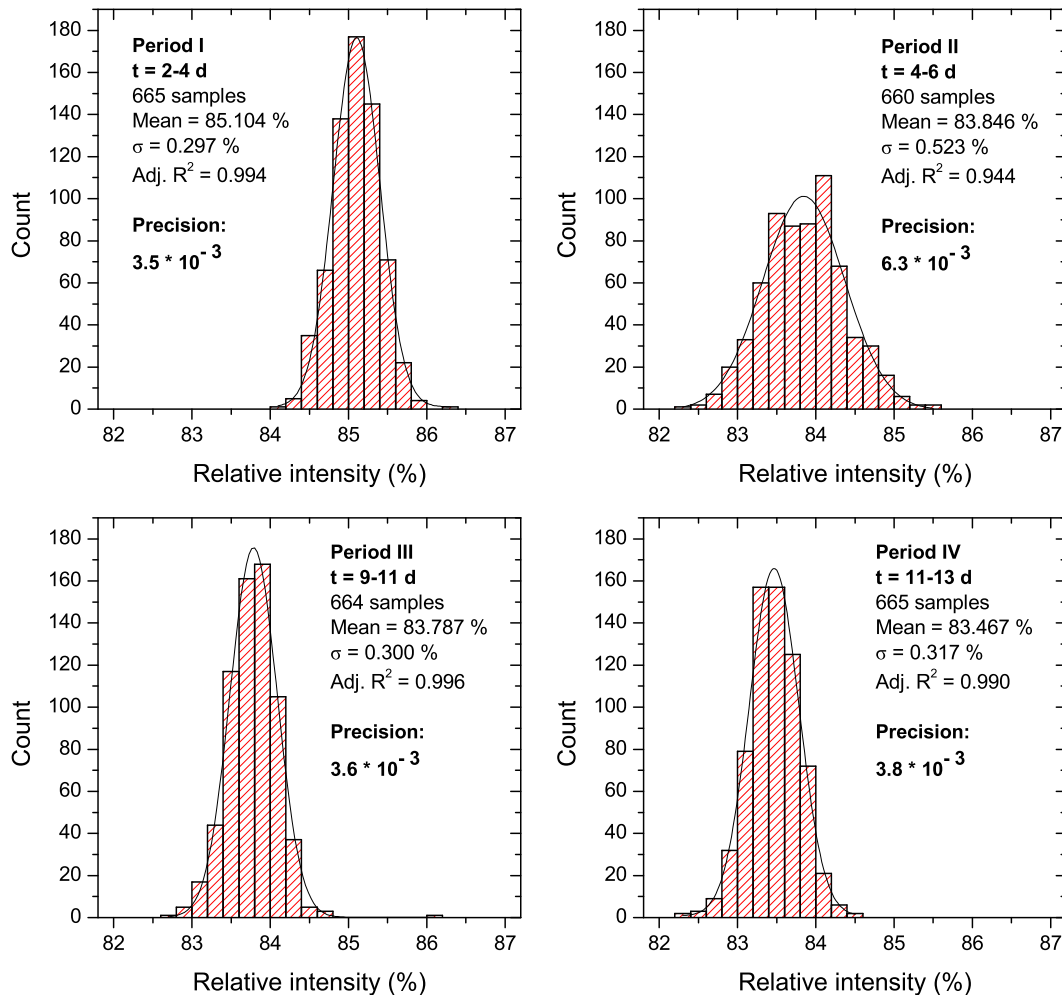


Figure 5.16: Run#3: Achieved precision relative peak intensity of T_2 . The precision $2\sigma/I_{\text{aver}}$, are determined for 4 intervals of run#3 with different laser base plate temperature profiles: Constant temperature (period I) and small temperature drift (period III), a drop of the temperature by 2 K (period II) and fluctuation of the temperature (period IV). The precision is calculated by dividing the standard deviation σ of the fitted Gaussian by the mean value, i.e. the centre position of the Gaussian. Note that σ is given as absolute value, i.e. in the same units as the mean.

5.7 Conclusions and consequences for KATRIN

Several conclusions can be drawn from the measurements described in this chapter. Although only the LARA2 setup was used, most aspects have direct implications on laser Raman measurements for KATRIN in general.

- The overheating of the Excel laser during run#1 showed that it cannot be operated inside the enclosure of LARA2 without active cooling. A standard 80 mm fan, installed on the laser base plate after run#1, was sufficient to keep the laser base plate temperature below 30 °C at 2 W nominal laser power in the subsequent measurements.
- A failure of the system, such as the damage of the wave plate in run#2, can despite of all efforts never be completely excluded. The already implemented interlock system closes the shutter to avoid further damage if the photo diode voltage drops below a threshold which can indicate a failure of the system. For standard operation of the LARA setup during KATRIN neutrino mass measurements a failure of the system has to be recognised immediately. Therefore the interlock system should be upgraded by an alert system that informs the person in charge about the failure of the system.
- The worsening of the relative peak intensities is related to beam pointing instabilities. The vertical beam pointing of the laser is strongly affected by temperature changes of the laser base plate while the effect on the horizontal beam pointing is negligible. During a drop of the laser base plate temperature by 4 K in run#3 a vertical beam walk of 0.5 mm was observed on the LM-10 sensor while the horizontal beam position changed only by 0.08 mm.

The absolute peak intensities and hence also the signal-to-noise ratios of the relative peak intensities are sensitive on vertical movements of the beam due to the narrow region in the LARA cell which is monitored by the collection optics. A vertical beam walk of 0.38 mm at the centre position of the LARA cell causes already a reduction of the absolute peak intensities by 22 % [Sch09]. Therefore vertical beam movements have to be reduced as much as possible to enhance the precision of the relative peak intensities.

- The changes of the laboratory ventilation system between night and day mode cause a temperature variation of the laser base plate by up to 2 K and influence the precision of the relative peak intensities: A worsening of the precision is observed in periods with enhanced thermal fluctuations in comparison to periods with stable laser base plate temperature. In run#2 the precisions were reduced by

$$\begin{aligned} D_2 &: 4.3 \cdot 10^{-3} \rightarrow 6.3 \cdot 10^{-3} \\ H_2 &: 4.9 \cdot 10^{-3} \rightarrow 5.6 \cdot 10^{-3} \\ HD &: 8.4 \cdot 10^{-3} \rightarrow 9.3 \cdot 10^{-3} \end{aligned}$$

and in run#3 by

$$T_2 : 3.5 \cdot 10^{-3} \rightarrow 6.3 \cdot 10^{-3}.$$

- The Excel laser should be temperature stabilised to ± 500 mK or better to reach highest stability in later measurements. The actual Raman measurements during KATRIN neutrino mass measurements will be performed with a more powerful laser, namely the 5 W Verdi laser of LARA1 or an equivalent laser. To reach 0.1 % precision continuously, a temperature stabilisation of the laser base plate to ± 500 mK or better is advisable since beam pointing instabilities also have been seen in the LARA1 setup.

It is shown in a coarse estimate in appendix B that the observed beam walk cannot be completely explained by a pointing instability of the laser. First indications were found that the mounts of the beam steering mirrors are affected by temperature changes and hence also cause a beam walk. Therefore the temperature stability of optical components in the LARA setups, e.g. the steering mirror, should be investigated and the most dominant sources of beam walk be identified. A temperature stabilisation of the most sensitive components could reduce the beam walk in the setup. If necessary, an active beam alignment system, based on a beam position monitoring with a webcam and feedback controlled steering mirrors could be implemented if beam walk cannot be reduced by temperature stabilisation.

- The laser power was monitored by two sensors during run#2 and by 3 sensors in run #3, respectively. All laser power readings were continuously declining apart from a contradictory reading of one photo diode in run#3. A long-term drop of the laser power or instabilities of the electronic read-out systems are possible although instabilities of the electronic read-out system are more probable. Investigations of the stability of the electronic read-out system of the photo diodes, namely the home-made pre-amplifiers, are currently ongoing since a reliable laser power measurement is absolutely necessary for operation during KATRIN neutrino mass measurement runs. A new design for the pre-amplifiers that uses more stable operational amplifiers is currently being designed. The LM-10 sensor is currently read-out with 10 mW resolution although its physical resolution is 1 mW. The 10 mW resolution was too coarse to detect all power variations in the measurements. A modification of the read-out software is therefore recommended.
- A periodic disturbance of the horizontal beam position and of the laser power reading of a photo diode was observed during the operation of LARA at LOOPINO. This type of disturbance was also observed during measurements with the LARA1 setup at LOOPINO in December 2009 and January 2010. A temporal correlation with the flushing process of the glove box atmosphere with fresh nitrogen gas was found. The hardware component causing the disturbance and the transmission path of the disturbance are currently not known. It has to be checked if only the sensors but not the laser itself are affected or if the laser parameters are actually affected. Nevertheless an actual disturbance of the laser seems to be more probable. A transmission via the power grid can be excluded. Further investigations are currently ongoing. The laser setup has to be shielded from this periodic disturbance since it cannot be accepted for KATRIN runs.

These conclusions can be condensed into several work packages that have to be achieved before the LARA hardware setup is fully prepared for standard operation in KATRIN neutrino measurement runs:

- Stabilisation of laser parameters by temperature stabilisation of the laser base plate.
- Investigation of thermal influences on pointing stability of beam steering mirrors and, if necessary, implementation of suitable measures to avoid beam walk.
- Identification of origin and transmission path of the periodic disturbance of laser parameters by the flushing of the glove box atmosphere with nitrogen gas. Removal of origin of disturbance or shielding of LARA setups against disturbance.
- Investigation of stability of pre-amplifiers of photo diodes and redesign of pre-amplifiers with more stable components to achieve higher precision.
- Modification of read-out software to reduce the resolution of LM-10 sensor from 10 mW to 1 mW in order to obtain a absolute laser power measurement with sufficient resolution.
- Implementation of an alarm system, in addition to the already existing interlock system, that informs the person in charge about a failure of the LARA setup.

Chapter 6

First depolarisation measurements with tritium at TLK

First depolarisation measurements with tritium were performed at TLK within the scope of this thesis to show the feasibility of the determination of a/γ ratios of tritiated hydrogen isotopologues with the existing LARA2 setup. The aim of the depolarisation measurements is to verify the theoretical calculations of the quantum mechanical constants a and γ of the tritiated hydrogen isotopologues (see section 3.2) by measurements. As it was already shown in subsection 3.1.5, the knowledge of a and γ is necessary for the calculation of line intensities in Raman spectra, according to equation (3.28) and (3.50), and hence for the determination of the gas composition in the WGTS by comparison of measured and calculated Raman spectra.

It was shown in the foregoing chapter that power and pointing instabilities of the laser are currently not fully understood and have to be further investigated to operate the LARA2 system with maximum achievable stability which is necessary for the depolarisation measurements. Therefore, the measurements described in this chapter have to be rather seen as proof-of-principle measurements which yield preliminary results than accurate measurements of the a/γ ratios.

It will be shown in section 6.1 that the geometry of the real scattering experiment has to be considered before a comparison of the measurements with theoretical predictions is possible. In the performed depolarisation measurements the line intensity, i.e. the area of a peak in the Raman spectrum, is measured as function of the polarisation angle of the incident, linearly polarised, light. The a/γ ratios are determined by a fit of the theoretically calculated curve to the measured data. A detailed description of the experimental setup, the measurement procedure and the data analysis is given in section 6.2 and section 6.3. The preliminary results are discussed in section 6.4 and the next steps which are necessary for the actual determination of a/γ ratios are stated in section 6.5.

6.1 Consideration of scattering geometry

It was shown in section 3.3 that the intensity I of the scattered radiation emitted from a single point into a specific direction (characterised by the angles φ and θ) is given by (3.28) and the line strength function

$$\begin{aligned} \Phi(a^2, \gamma^2, \varphi, \theta, \perp^s + \parallel^s, \psi) = \\ \frac{b_{J', J''}^{(2)} \gamma^2}{15} + \left[\left(a^2 + \frac{b_{J', J''}^{(2)} \gamma^2}{45} \right) \cdot \cos^2 \theta + \frac{b_{J', J''}^{(2)} \gamma^2}{15} \right] \cdot \cos^2(\varphi - \psi) + \\ \left(a^2 + \frac{4}{45} b_{J', J''}^{(2)} \gamma^2 \right) \cdot \sin^2(\varphi - \psi) \end{aligned} \quad (6.1)$$

for a light detection system with “small” aperture. “Small” means that the scattered light is treated as a narrow and collimated beam of radiation that is emitted from a single point. In case of constant temperature and laser intensity are the population factor N_i and the irradiance \mathcal{I} , which both are part of (3.28), constant and the intensity I of the scattered light only depends on the line strength function.

In this section two geometrical effects are discussed that are related to the treatment of the realistic scattering geometry in the LARA2 setup:

1. The non-zero solid angle of the collection optics. This effect will be included in the first analysis.
2. The scattering region in the LARA cell is not point-like but is extended along the laser beam. This effect will not be considered in this first analysis but will be briefly discussed.

The aim of this section is to derive an expression for the observed intensity of scattered light in the LARA2 setup that takes into account the solid angle of the collection optics and to motivate why the extended scattering region also has to be taken into account in later measurements. The expression for I will depend on the polarisation angle ψ of the incident light and on the quantum mechanical parameters a and γ which were both introduced in subsection 3.1.5. All other parameters, e.g. the population factor N_i , the wavenumber $\tilde{\nu}_s$ of the incident laser light and the irradiance \mathcal{I} of the incident light, are assumed to be constant and therefore will be replaced by an overall constant factor¹.

6.1.1 Consideration of solid angle of collection optics

The scattered light leaves the LARA cell through the window and reaches the collection optics. The size of the window is not limiting the light flux but the flange that houses the window and connects it with the LARA cell (see figure 6.1). The angle between light rays that just manage to leave the cell is about 35° and hence not compatible with the assumption of a narrow and collimated beam of scattered light. Therefore the solid angle which is covered by the collection optics has to be considered when calculating the observed intensity I of scattered light.

¹In case of variations of the laser power, i.e. of the irradiance \mathcal{I} , the experimental data can be corrected by normalising the observed line intensity with the laser power

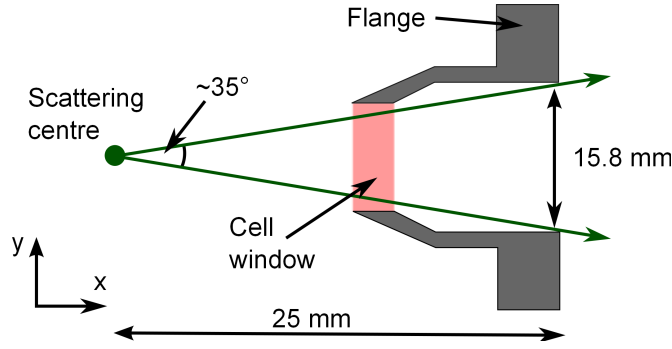


Figure 6.1: Schematic drawing of LARA cell window and flange (Side view). The laser light scatters on gas molecules in the scattering centre. The scattered light leaves the cell through the window towards the collection optics (not shown). The flange that houses the window allows an maximum opening angle of the scattered light of about 35° . The surrounding LARA cell body is not shown in this schematic drawing. Drawing is not to scale.

This can be achieved by integrating equation (3.28) over the solid angle Ω which is defined by the flange of the cell window. Since only the line strength function depends on the angles θ and φ and all other parameters are, according to the discussion before, assumed to be constant, the observed intensity I is given by

$$\begin{aligned} I(a^2, \gamma^2, \perp^s + \parallel^s, \psi) &= \kappa \int_{\Omega} d\Omega \Phi(a^2, \gamma^2, \varphi, \theta, \perp^s + \parallel^s, \psi) \\ &= \kappa \int_{\theta_{\min}}^{\theta_{\max}} \sin \theta \, d\theta \int_{\varphi_{\min}(\theta)}^{\varphi_{\max}(\theta)} d\varphi \Phi(a^2, \gamma^2, \varphi, \theta, \perp^s + \parallel^s, \psi) \end{aligned} \quad (6.2)$$

where κ is a constant and the $\sin \theta$ term was introduced in the second step due to integration using spherical coordinates. The limits of the integration over φ and θ have to be set such that only the solid angle Ω is covered in the integration. Since the integration over φ will be performed before the integration over θ the limits $\varphi_{\min}(\theta)$ and $\varphi_{\max}(\theta)$ of the integration over φ will depend on θ in order to describe the aperture that limits the solid angle. In the next steps the integration limits of both integrations will be deduced based on the nomenclature introduced by figure 6.2.

Every point P on the edge of the aperture fulfils

$$r^2 = r_y^2 + r_z^2 \quad (6.3)$$

where r is the radius of the aperture and r_y and r_z are the vertical and horizontal distance of P relative to the centre M of the aperture. r_y can be expressed by d and φ

$$\tan \varphi = \frac{r_y}{d} \quad \Leftrightarrow \quad r_y = d \tan \varphi \quad (6.4)$$

using the right-angled triangle $OP'M$. r_z is in a first step expressed by θ and d''

$$\cos \theta = \frac{r_z}{d''} \quad \Leftrightarrow \quad r_z = d'' \cos \theta \quad (6.5)$$

in the right-angled triangle OPP' . d'' can be expressed by $d''^2 = d^2 + r^2$ which allows to rewrite equation (6.5) to

$$r_z = \sqrt{d^2 + r^2} \cdot \cos \theta. \quad (6.6)$$

Replacing r_y and r_z in equation (6.3) by these expressions and solving for φ yields to

$$\begin{aligned}\varphi_0(\theta) \equiv \varphi &= \arctan \sqrt{\frac{r^2}{d^2} \cdot (1 - \cos^2 \theta) - \cos^2 \theta} \\ &= \arctan \sqrt{\frac{r^2}{d^2} \cdot \sin^2 \theta - \cos^2 \theta}\end{aligned}\quad (6.7)$$

which allows to calculate the φ angle of an arbitrary point P on the edge of the aperture, with radius r and distance d to the scattering centre, for a given angle θ . Hence the integration limits of the φ -integration are for a given angle θ

$$\begin{aligned}\varphi_{\min}(\theta) &= -\varphi_0(\theta) \\ \varphi_{\max}(\theta) &= \varphi_0(\theta).\end{aligned}\quad (6.8)$$

The integration limits for the θ -integration are given by

$$\begin{aligned}\theta_{\min} &= \arctan \frac{d}{r} \\ \theta_{\max} &= \pi - \arctan \frac{d}{r}\end{aligned}\quad (6.9)$$

which can be seen when the intersection points of the aperture and the xz -plane are considered. The intensity $I(a^2, \gamma^2, \perp^s + ||^s, \psi)$ of the scattered light, defined in equation (6.2), is now fully determined and can be used to determine a and γ by evaluating the integrals and fitting the result to measured data.

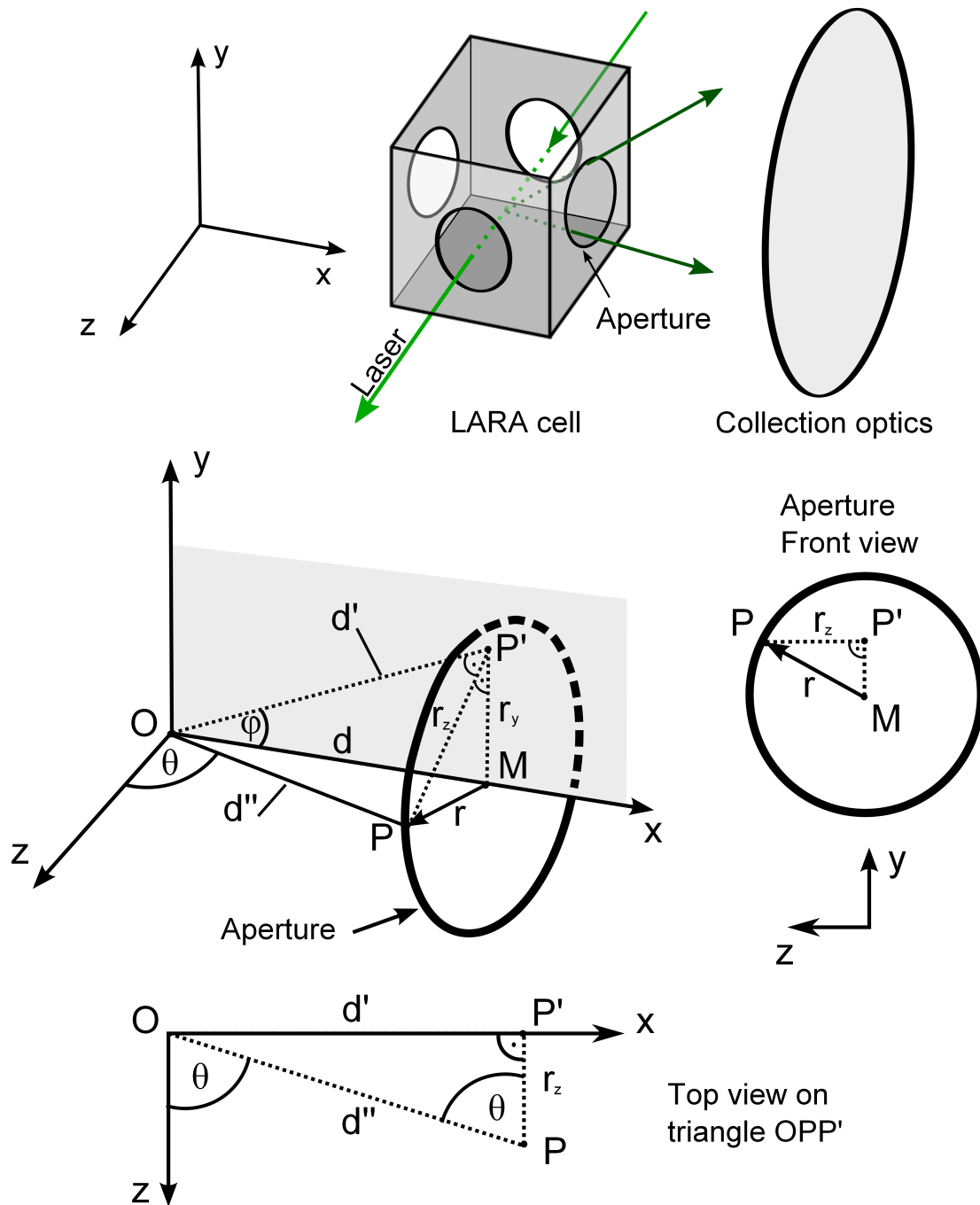


Figure 6.2: Scattering geometry and parametrisation of aperture by angles φ and θ . *Top:* Schematic drawing of scattering geometry. The aperture, i.e. the flange of the cell window, limits the flux of scattered light towards the collection optics. *Middle:* The aperture with radius r is located in distance d from the scattering centre, placed in the origin O of the coordinate system. The centre M of the aperture is placed on the x -axis. Every point on the edge of the aperture can be described by the angles φ and θ but also by its vertical distance r_y and horizontal distance r_z from the centre of the aperture. The distances d' and d'' are used to calculate r_y and r_z as function of φ and θ (see text). *Bottom:* Top view on triangle OPP' which is used to determine r_z as function of θ . Note that the point P' is located in the xy plane and not directly on the x -axis.

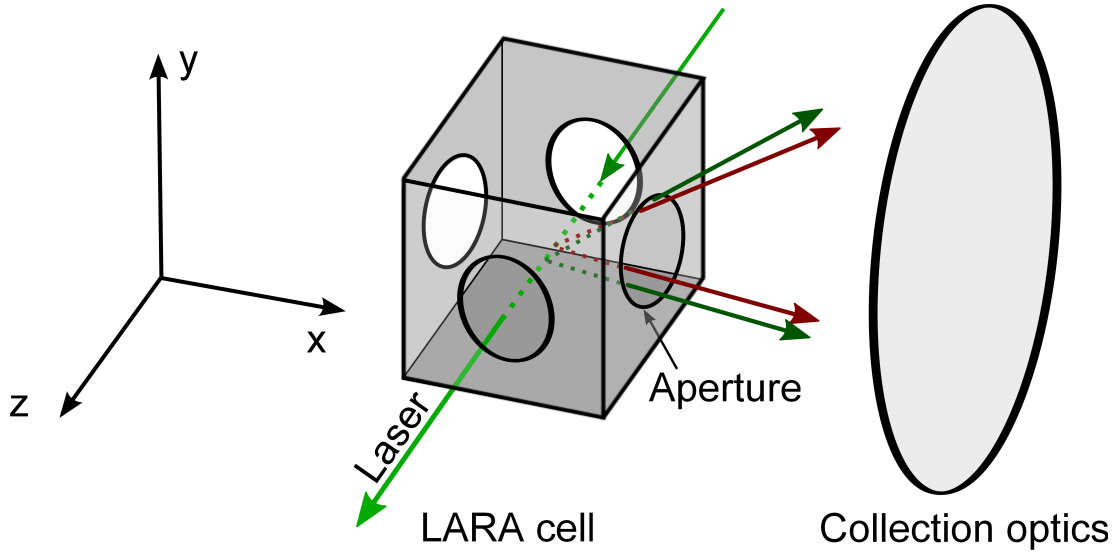


Figure 6.3: Consideration of extended scattering region. Light from an extended region along the laser beam leaves the LARA cell and is observed by the collection optics, here shown for two scattering centres along the laser beam. The collection optics image 1:1 the extended scattering region onto the optical fibres (not shown) which are arranged along a 6 mm long horizontal line.

6.1.2 Consideration of extended scattering region

Although this effect is not considered in the preliminary analysis of the experimental data in section 6.4 it will be briefly motivated in this subsection why the extended scattering region has to be taken into account in later depolarisation measurements. Up to now a point like scattering region was assumed, i.e. that all scattered light is emitted from the centre position of the LARA cell. In reality the scattered light is emitted from all points along the laser beam in the volume of the LARA cell. The light that leaves the LARA cell is imaged 1:1 on the optical fibres which guide the light to the filter and spectrograph. The volume in the LARA cell which is observed by the collection optics is determined by the optical fibres that are aligned along a 6 mm long horizontal line (see figure 4.8).

The consideration of the extended scattering region will introduce a third integration into equation (6.2) which is performed after the two other integrations and integrates the line strength function over the position l along the beam path.

$$I(a^2, \gamma^2, \perp^s + \parallel^s, \psi) = \kappa \int_{l_{\min}}^{l_{\max}} dl \int_{\theta_{\min}(l)}^{\theta_{\max}(l)} \sin \theta d\theta \int_{\varphi_{\min}(\theta, l)}^{\varphi_{\max}(\theta, l)} d\varphi \Phi(a^2, \gamma^2, \varphi, \theta, \perp^s + \parallel^s, \psi) \quad (6.10)$$

The limits of the φ - and θ -integrations will both depend on the integration variable l . This correction is not considered in this work but has to be applied in later measurements. A further effect is introduced when the extended scattering region is considered since the window of the LARA cell, and not only the flange, limits the flux of scattered light if scattering centres further away from the centre position are considered (see figure 6.4).

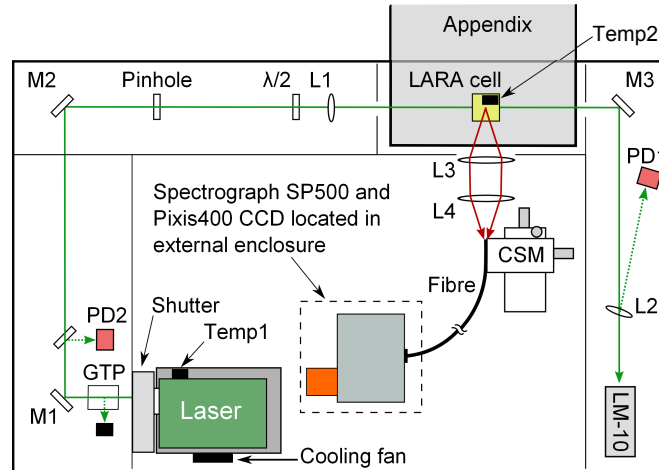


Figure 6.5: Experimental setup of depolarisation measurements. The wave plate ($\lambda/2$) is used to gradually turn the polarisation angle of the incident laser light. The scattered light is analysed with the SP500 spectrograph and the PIXIS:400B using a high resolution grating to resolve nearly all lines of the Q_1 branch of T_2 .

6.3 Measurement procedure

The acquisition time per spectrum has to be well chosen in this experiment since it determines the achievable signal-to-noise ratio (SNR) in the RAMAN spectra. The SNR, in turn, directly affects the accuracy of the peak area determination which is used to measure the line intensity. The line intensities are expected to vary significantly due to the turning of the polarisation angle of the incident light. Therefore, a long enough acquisition time has to be chosen to be able to determine the peak areas even in case of minimum line intensity. The usage of the high resolution grating of the SP500 further reduces the SNR due to the limited spectral intensity of the scattered light in the very narrow part of the spectrum which is monitored in this measurement. The acquisition time was set to $T=750\text{ s} = 12.5\text{ minutes}$ as a compromise between maximising the SNR and overall duration of the measurement which still was in the order of 13 hours. The

Table 6.1: Parameters of depolarisation measurement

Location	Operation at LOOPINO
Gas mixture, operation mode	T_2 gas with about 200 mbar total pressure and about 95 % T_2 concentration. The valves in front and after the cell were closed after the filling of the cell.
Spectrometer (slit width, grating, central wavelength)	SP500, 125 μm , 2400 grooves/mm, 612.0 nm
CCD (Temperature, read-out speed, gain)	Pixis:400B, -75 $^\circ\text{C}$, 100 kHz, gain 3
Acquisition time per spectrum	750 s
Laser:	Power set point 2 W

measurement parameters are summarised in table 6.1. The width of the entrance slit of the spectrometer was set to $125 \mu\text{m}$ as a compromise between high light intensity and high spectral resolution.

The rotational mount was set to $\psi_{\text{mount}} = 0^\circ$ for the first acquisition, which is close to the setting of an intensity maximum in the modulation curve shown in figure 3.13. The angle ψ_{mount} of the rotational mount was gradually increased in $\Delta\psi_{\text{mount}} = 4^\circ$ steps from acquisition to acquisition. Therefore the polarisation angle ψ of the incident light was increased in $\Delta\psi = 2 \cdot \Delta\psi_{\text{mount}} = 8^\circ$ steps since the wave plate turns the polarisation of the light by two times the rotational angle of the wave plate. The change of the setup between two measurements took about 3 minutes and the measurement was performed for the angles from $\psi = 0^\circ$ to $\psi = 166^\circ$ without interruptions over a period of about 10.5 hours in order to minimise environmental effects on the measurement. After this first part of the measurement, the laser was kept on and the shutter was closed over night and the measurement was continued the next morning for the angles $\psi = 156^\circ$ to $\psi = 188^\circ$. The settings $\psi = 156^\circ \approx 5.44 \text{ rad}$ and $\psi = 160^\circ \approx 5.58 \text{ rad}$ were repeated to check the reproducibility of the measurement which was found to be within the statistical fluctuations.

The data file of the measurement for $\psi = 256^\circ \approx 4.46 \text{ rad}$ was corrupted and hence not considered in the analysis.

6.4 Data analysis and preliminary results

The spectra for $\psi_{\text{mount}} = 88^\circ$ rad and $\psi_{\text{mount}} = 136^\circ$ rad are shown in figure 6.6 as exemplary spectra of the measurement and demonstrate the significant variation of the

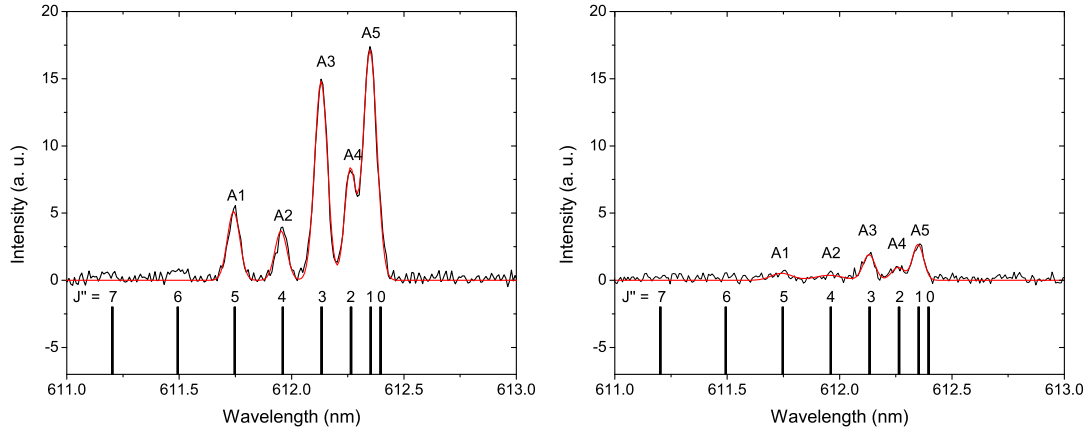


Figure 6.6: Spectrum of the Q_1 branch of T_2 for $\psi_{\text{mount}} = 88^\circ$ (left) and $\psi_{\text{mount}} = 136^\circ$ (right). The peak intensities vary significantly due to the rotation of the polarisation angle of the incident laser light. The black bars indicate the expected line positions of the Q_1 lines of T_2 . *Left:* The $J''=0$, $J''=1$ and $J''=2$ are overlapping each other while the $J''=3$, $J''=4$ and $J''=5$ lines are well resolved. The intensity of the $J''=6$ line is just slightly above the background level while the $J''=7$ line is not visible. The peaks are labelled from A1 to A5. The spectrum is fitted by five Gaussian peaks (red line), i.e. the overlapping $J''=0$ and $J''=1$ lines are fitted by one Gaussian peak "A5". *Right:* The peak intensities are strongly reduced. The $J''=0$ to $J''=3$ peaks are still visible while the intensity of the $J''=4$ and $J''=5$ peaks is comparable with the background level.

peak intensities due to the rotation of the wave plate. The individual Q_1 peaks of T_2 for $J''=0$ to $J''=5$ are observed in case of maximum peak intensity but not all peaks can be resolved. The $J''=0$ peak is strongly overlapping with the $J''=1$ peak, which is also overlapping with the $J''=2$ peak. The other peaks are nicely resolved.

The laser parameters and the temperature readings are shown in figure 6.7 and allow to deduce several conclusions:

- A periodical variation of the photo diode 1 voltage is clearly visible which is probably caused by beam walk, i.e. by a variation of the beam position due to the rotation of the wave plate. A small variation of the beam direction might have moved the reflection of the beam slightly onto or off the active area of the photo diode and hence might have caused a variation of the photo diode voltage.
- The laser power measurements by the photo diode 2, which was placed directly at the beginning of the beam path (see figure 6.5), and the LM-10 sensor show no significant variation of the laser power. Therefore it will be assumed in the following that the laser power was constant over the duration of the depolarisation measurement. Hence the peak intensities do not have to be normalised to the laser power.
- The photo diode 1 voltage is slightly increasing besides the already mentioned periodic variation. This agrees with run#3 of the long term measurements in chapter 5 where also a steady increase of the photo diode 1 voltage was observed.
- The laser base plate temperature rises during the first 6 measurements which indicates that the laser was not completely warmed up. Accordingly a corresponding trend is seen in the vertical beam position which agrees with the findings from run#3 of the long term measurements. The base plate temperature further increases during the interruption of the measurement over night since the laser was kept on over night.
- The temperature of the LARA cell rises by about 0.7 K during the first measurements probably due to the irradiation of the laser light. A slight cooling down of the LARA cell by about 0.1 K is visible during the interruption of the measurement when no laser light was present in the LARA cell.

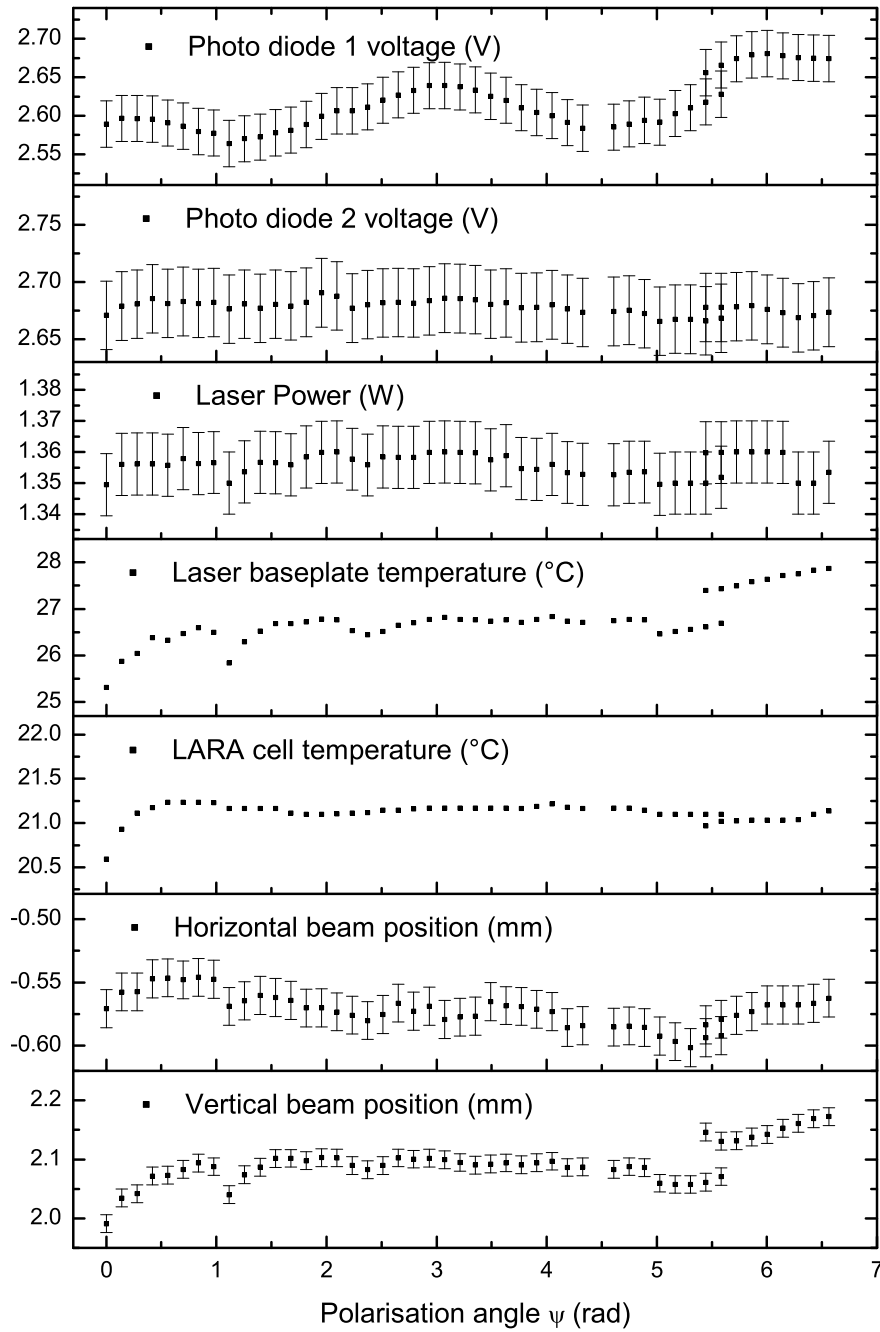


Figure 6.7: Laser parameters during depolarisation measurement. The interruption of the measurement and the repeated measurements for $\psi \approx 5.44$ rad and $\psi \approx 5.58$ rad are clearly visible in most of the laser parameters. The data point for $\psi \approx 4.46$ rad is missing due to a corruption of the data file. The errorbars of the photo diode voltages are estimated from the variation of the photo diode voltage during the acquisition. The error bars of the LM-10 sensor represent the read-out resolution of 10 mW.

Each of the acquired spectra is analysed in four steps:

- A baseline is fitted to the spectrum and subtracted.
- The five peaks in the spectrum are fitted by Gaussian peaks.
- The peak area, which is one of the fit parameters, is extracted and used as a measure of the line intensity.
- For each peak, the peak areas are plotted as function of polarisation angle ψ and the intensity function (defined in equation (6.2)) is fitted on the data using the integration limits from equations (6.8) and (6.9). The fit is done using the ROOT² data analysis framework. The source code of the analysis macro can be found in appendix D. The Placzek-Teller factor $b_{J',J''}^{(2)}$ which is an input parameter of the intensity function was calculated according to equation (3.48).

The absolute peak intensity of the Q₁ lines and the fitted intensity function are shown in figure 6.8. The peak A5 was fitted assuming J=1, i.e. the overlap with the smaller J=0 peak was neglected. In a full analysis, the overlapping J=0 and J=1 peaks have to be resolved in the spectrum and then treated separately. A quantification of the goodness of the fits by the reduced χ^2 will not be done in the following since the uncertainties of the peak area determination were not considered in this first analysis. This will be done in a later, more sophisticated analysis. The fit of the modulation of the area of peak A2, which has the lowest absolute peak intensity in the spectrum and hence the strongest statistical fluctuations, does not converge. Therefore this peak is not further considered in the analysis. The fit parameters $a' = \kappa a$ and $\gamma' = \kappa \gamma$ are denoted by a prime to indicate that they differ from the real a and γ values by the unknown overall factor κ . The uncertainties of the fit parameters a' , γ' and ψ_0 are underestimated since the uncertainties of the peak areas are not considered in this first analysis.

²<http://root.cern.ch/drupal/>

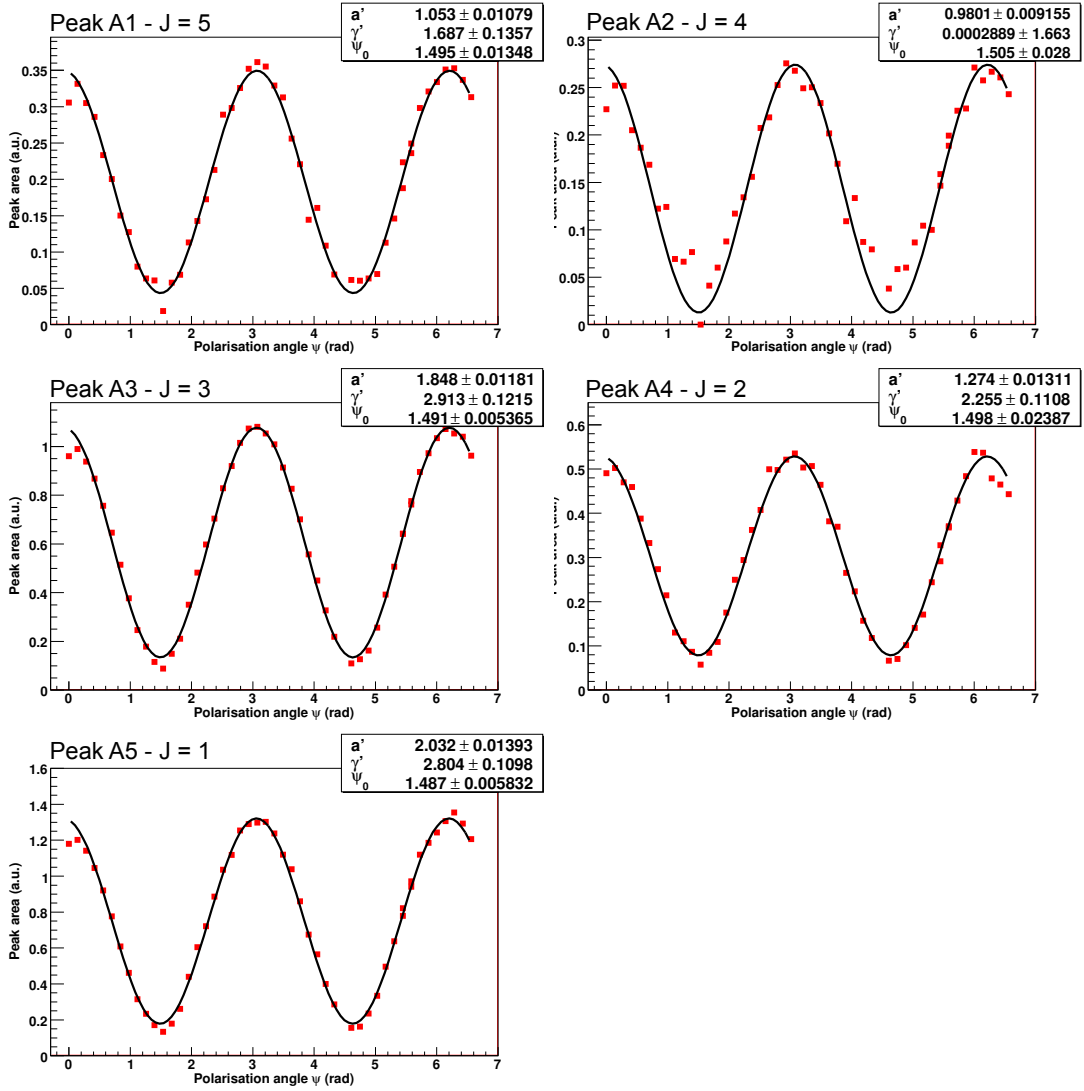


Figure 6.8: Variation of absolute peak intensities in depolarisation measurement. The fits of the intensity function on the data converge well for all peaks apart the A2 peak which has the lowest absolute intensity in the spectrum. The A5 peak which consists of the two overlapping J=0 and J=1 peaks is fitted with J=1, neglecting the contribution from the smaller J=0 peak. The prime on the fit parameters $a' = \kappa a$ and $\gamma' = \kappa \gamma$ indicate that both parameters are actually the parameters of interest multiplied by the overall scaling factor κ .

Table 6.2: Determination of a/γ ratios. For each peak the rotational quantum number J and the corresponding Placzek-Teller factor $b_{J',J''}^{(2)}$, which is used in the fit of the experimental data, are indicated. The uncertainties of a/γ are underestimated. The theoretical values of a/γ are extracted from [Hun84].

Peak	J	$b_{J',J''}^{(2)}$	a/γ	a/γ (theo)
A1	5	$\frac{10}{39}$	0.62 ± 0.06	1.2327
A3	3	$\frac{4}{15}$	0.63 ± 0.03	1.2382
A4	2	$\frac{2}{7}$	0.56 ± 0.03	1.2401
A5	1	$\frac{2}{5}$	0.72 ± 0.03	1.2414

The a/γ ratios are determined by the division of a' by γ' . The uncertainties of the a/γ ratios are calculated by the propagation of uncertainty assuming no correlation between a' and γ' . The results can be found in table 6.2. A strong disagreement is found between the measured a/γ ratios and the theoretical values. All measured a/γ ratios are about a factor of two smaller than the theoretical values. Even if the statistical uncertainties are enlarged by considering the statistical uncertainties of the peak area determination a systematic disagreement between measured and theoretical values will remain. In general this disagreement can have three different sources:

- **Incorrect theoretical values**

The a/γ ratios for the Q_1 branches of the non-tritiated isotopologues H_2 and D_2 were measured by Golden and Crawford [Gol62] and agree well with the theoretical values [Hun84]. The theoretical a/γ ratios of the Q_1 lines of T_2 vary by less than 5 % from the a/γ ratios of H_2 [Hun84]. Therefore, an error in the theoretical values of T_2 in the order of 50 % can very likely be excluded.

- **Systematic effects in data analysis**

It was stated in the beginning of this chapter that the consideration of the solid angle of the collection optics is only one of the necessary corrections which has to be applied on the idealised treatment of the line strength function in section 3.3. The consideration of the extended scattering region, which was briefly discussed in subsection 6.1.2, might help to improve the agreement of the measured and theoretical ratios. This should be done in the near future for completeness although a significant improvement is not expected. A detailed study of the statistical uncertainties of the peak area determination in the second step of the data analysis should be performed to estimate the significance of the disagreement between measured and theoretical a/γ ratios.

Besides the currently not considered correction also an error in the current data analysis has to be considered. Therefore the experimental data was analysed without taking into account the solid angle of the collection optics, i.e. the line strength function in equation (6.1) was directly fitted on the data with fixed angles $\varphi = 0$ and $\theta = \pi/2$ as shown in figure 6.9.

Table 6.3: Determination of a/γ ratios without taking the solid angle of the collection optics into account. The a/γ ratios are determined by a direct fit of the line strength function from equation (6.1) on the data for the fixed angles $\varphi = 0$ and $\theta = \pi/2$. The Placzek-Teller factor $b_{J',J''}^{(2)}$, which is used in the fit of the experimental data, is indicated. The uncertainties of a/γ are underestimated. The theoretical values of a/γ are extracted from [Hun84].

Peak	J	$b_{J',J''}^{(2)}$	a/γ	$a/\gamma(\text{theo})$
A1	5	$\frac{10}{39}$	0.48 ± 0.05	1.2327
A2	4	$\frac{20}{77}$	0.40 ± 0.05	1.2358
A4	2	$\frac{2}{7}$	0.46 ± 0.019	1.2401

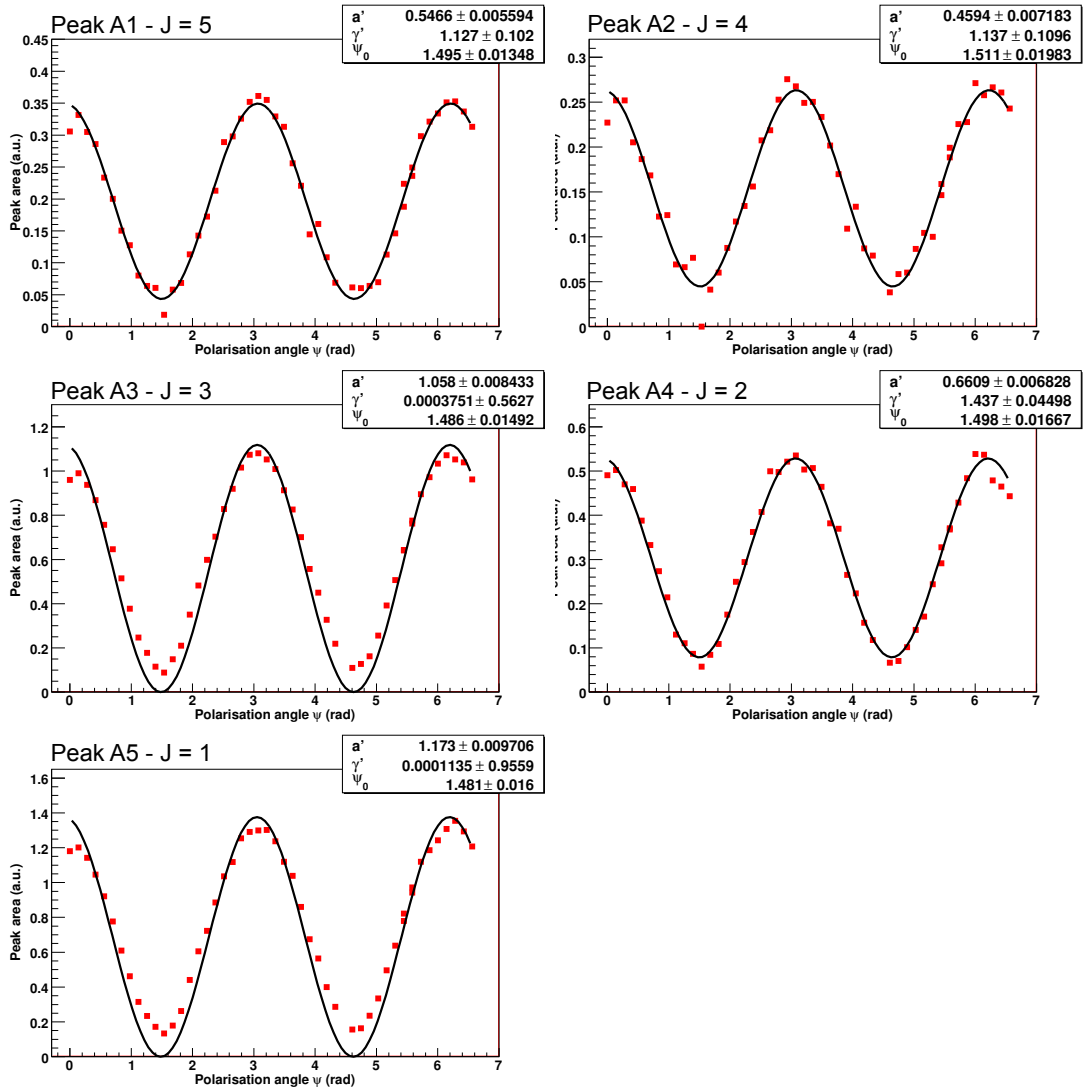


Figure 6.9: Data analysis without geometrical considerations. The fits of the line strength function function on the data converge well for all peaks apart the A3 and A5 peaks. The prime on the fit parameters $a' = \kappa a$ and $\gamma' = \kappa \gamma$ indicate that both parameters are actually the parameters of interest multiplied by the overall scaling factor κ .

This time the fits of the A3 and A5 peaks do not converge, the reason is currently not known. The resulting a/γ ratios for the remaining A1, A2 and A4 peaks disagree even more with the theoretical values (see table 6.3) than the results from the analysis with consideration of solid angle of the collection optics. The increased systematic deviation of the measured values from the theoretical ratios shows that the consideration of the solid angle of the collection optics is a necessary correction in the data analysis. An indication for a significant error in the consideration of the solid angle of the collection optics therefore cannot be found.

- **Systematic effects in the experimental setup**

Systematic effects in the experimental setup are the third potential cause of the observed disagreement between measured and calculated a/γ ratios.

Deviations of the actual scattering geometry from the geometry which is used in the data analysis might cause systematic effects. The most likely deviation is a change of the distance of the aperture to the beam due to beam walk and uncertainties in the alignment of the setup. The influence of a small (≤ 1 mm) variation of the beam - aperture distance on the consideration of the solid angle of the collection optics should be estimated.

Of particular importance are polarisation dependent effects which will be briefly discussed now.

Changes of the transmission of the focus lens L1 (see figure 6.5) and the entrance window of the LARA cell due to the change of the polarisation angle are expected to be small since the beam points perpendicular on the surfaces of these optical components. The large solid angle of the side window of the LARA cell, which was discussed in subsection 6.1.1, causes that the scattered light passes through the side window of the LARA cell under different angles. The transmission of the scattered light through the window depends, according to Fresnel's equations, on the angle of incidence and on the polarisation of the light. This could cause a variation of the transmitted light when changing the polarisation angle of the incident light.

The efficiency of the SP500 spectrometer, which is of Czerny Turner type and hence internally uses mirrors (see subsection 4.3.6), is also polarisation dependent due to the polarisation dependent reflectivity of the mirrors. This effect is currently neglected since it is assumed the polarisation of the scattered light is completely scrambled by the optical fibre. If a fraction of the polarisation of the scattered light is preserved after passing through the optical fibre a polarisation dependent effect might be present in the spectrograph. Furthermore polarisation dependent effects in the coatings of the optical components in the beam path are currently not considered and could, if present, cause a variation of the laser intensity. The mentioned potential sources for systematic effects and their impact on the depolarisation measurement should be investigated in the near future.

6.5 Conclusion and consequences for KATRIN

First depolarisation measurements with tritium were performed in the Tritium Laboratory Karlsruhe to verify the ratio of the theoretically calculated constants a and γ of the Q_1 branch of T_2 . These molecular specific constants are necessary to accurately calculate line intensities in Raman spectra. It was shown that the scattering geometry of the experimental setup, i.e. the solid angle of the collection optics and the extended scattering region in the cell, has to be considered when data from a depolarisation measurement are analysed. The former correction was applied in this first analysis while the latter was neglected.

A systematic deviation of measured a/γ ratios of the tritium Q_1 branch from the theoretical values was found. A currently not considered systematic effect in the experimental setup is assumed to be the cause of the systematic disagreement since an error about 50 % in the theoretical calculations of the a/γ ratios is unlikely. Several potential sources of systematic effects are presented and have to be further investigated. The statistical uncertainties are not fully considered in this first proof-of-principle analysis.

Based on these findings the following next steps are suggested:

- Implementation of the complete treatment of the statistical uncertainties and of the second data correction routine, due to the extended scattering region, into the ROOT macro for a repeated analysis of present data.
- Repetition of the measurement with H_2 and/or D_2 and comparison of achieved a/γ ratios with available theoretical [Hun84] [Sch87] and experimental data [Gol62]. This allows to test the accuracy and reliability of the current setup and data analysis procedure. If again a systematic deviation from the reference values is observed it must be assumed that currently not all systematic effects are known and understood.
- Investigation if the currently overlapping Q_1 ($J=1$ and $J=0$) peaks of T_2 can be resolved with the SP500 by reducing the slit width of the spectrometer.

Although unexpected challenges appeared in the accurate determination of the a/γ ratios the general feasibility of the depolarisation measurements could be shown by this first proof-of-principle measurement.

Chapter 7

Summary and Outlook

Laser Raman spectroscopy is used in the KATRIN experiment to monitor the purity of the tritium gas inside the WGTS. The precision of the purity monitoring has to be better than 10^{-3} in order to reach the claimed sensitivity of $200 \text{ meV}/c^2$ on the electron anti neutrino mass. The power and pointing stability of the laser is expected to significantly influence the precision of the measurement of the gas composition and hence has to be measured and minimised. The aim is to guarantee a stable and reliable operation of the LARA setup over a typical period of about 2 months.

A dedicated study of laser stability and the influence of thermal effects on the system was performed with the LARA2 system which was set-up within the scope of this thesis. A static gas sample with 217 mbar total pressure and a T_2 concentration of $> 85 \%$ was monitored over a period of 15 days using the test loop system LOOPINO which is located in the ISS glovebox of TLK.

It was found that the beam pointing is strongly correlated with the temperature of the laser base plate. A temperature variation of 4 K caused a vertical beam movement of 0.4 mm at the end of the beam path. The laser base plate temperature is affected by the changes of the laboratory ventilation system between the night and day operation mode: Periodic temperature variations of typically $\pm 0.5 \text{ K}$ and corresponding vertical beam movements of the order of 0.05 - 0.1 mm were observed. A periodic distortion in one of the laser power measurements and in the beam position measurement was found and could be traced back to the regular flushing of the glove box atmosphere with nitrogen gas. A disagreement between the individual laser power measurements was found which might be caused by long term drifts of the employed pre-amplifiers. Based on these findings several suggestions for the improvement of the setup could be made.

A precision of $(3.5 - 6.3) \cdot 10^{-3}$ was achieved for the monitoring of the Q_1 branch of about 185 mbar partial pressure T_2 in the long term measurement with 2W laser power and 250 s acquisition time. The variation of the precision is mainly caused by beam pointing instabilities which were induced by temperature variations. Although the LARA2 setup cannot reach the precision of the LARA1 setup, which has a 2.5 times more powerful laser and will be the standard system of KATRIN, LARA2 can be used as an interim replacement in case of a failure of the LARA1.

Most of the findings concerning laser stability are also expected to be valid for the LARA1 setup since both systems are based on the same design and both use a diode

pumped solid state laser. Beam pointing instabilities, caused by temperature fluctuation, and the distortion of sensor readings due to the flushing of the glove box atmosphere with nitrogen gas were in the meantime also observed in the LARA1 setup. Therefore most of the proposals for an improvement of the LARA2 system are also valid for the LARA1 system and hence should be applied as well.

In a second step, the LARA2 setup was used to perform first depolarisation measurements with T_2 in order to show the feasibility of a measurement of the ratio of the average and anisotropic components a and γ of the polarisability of T_2 . The aim is to experimentally verify theoretically calculated values for a and γ which are necessary for the theoretical calculation of Raman spectra and hence for the accurate determination of the gas composition. A method for the consideration of the finite solid angle of the collection optics was developed and applied in the first analysis of experimental data. The general feasibility of the method could be shown since the expected variation of the line intensity as function of the polarisation angle of the laser light was observed.

The preliminary results for the a/γ ratios deviate from the theoretically calculated values by about a factor of two which is seen as an indication for a currently not considered systematic effect. Since not all necessary corrections of the experimental data were applied in the analysis and the statistical uncertainties on the a/γ ratios are currently underestimated, a second, more detailed analysis has to be performed in the future as well as additional measurements. It is proposed to perform e.g. further depolarisation measurements with H_2 and D_2 , since theoretical and experimental data is available for these isotopologues. This allows to check the accuracy and precision of the experimental method for the determination of the a/γ ratios and to test if the deviation of the acquired ratios is caused by a currently not known systematic effect.

Further improvements of the LARA setups are planned for the near future in order to increase the precision for the measurement and to enhance the monitoring sensors in the setup:

- The more than 10 years old laser in the LARA1 setup will be replaced by a new, more stable laser (Finesse 5 W, Laser Quantum) since a reliable operation for the complete measurement periods of KATRIN can no longer be guaranteed and a reconditioning of the existing laser would be uneconomical. The base plate of the new laser will be temperature stabilised in order to reduce beam walk due to temperature variations which were also observed in the LARA1 setup. With this replacement it is expected that the LARA1 setup will fulfil the requirement of 10^{-3} precision continuously during KATRIN neutrino mass measurement periods.
- A second photo diode should be permanently installed in the LARA setups, located at the beginning of the beam path. A monitoring of the laser power directly at the beginning of the beam path promises a more precise power measurement since variations of the illumination of the photo diode due to beam walk are expected to be smaller than at the end of the beam path.
- A new read-out algorithm of the CCD is currently being investigated in order to reduce the read-out noise of the CCD which is added to every read-out signal. Currently the intensity of each pixel is read out individually and hence contains read-out noise. On-chip binning of several rows of the CCD before read-out reduces the number of signals which have to be read out and hence reduces the read out noise. Since the performance of the post-processing routines, described

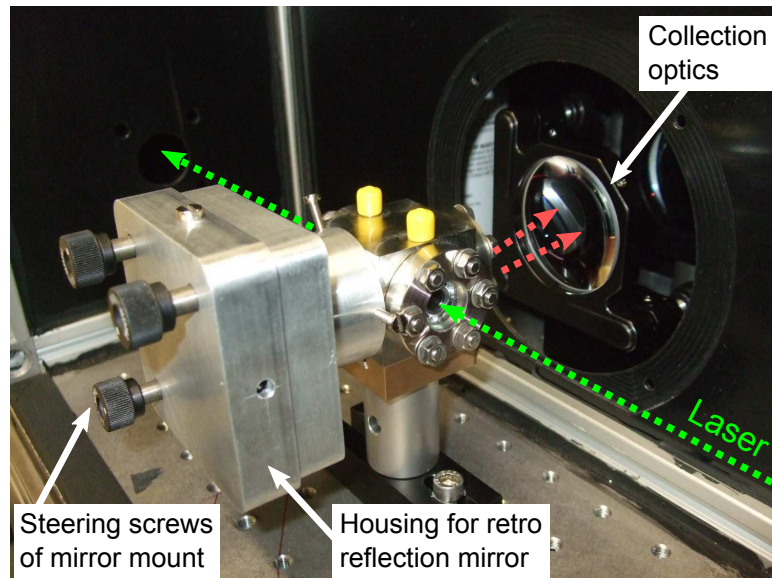


Figure 7.1: Test of the retro reflection mirror. A light tight housing for a spherical mirror is attached to the currently not used side window of the LARA cell. Light which is emitted towards the mirror is back reflected and hence emitted towards the collection optics. The intensity of the observed scattered light can, in principal, be increased by up to a factor of two. The picture shows a first test with a LARA cell filled with ethanol. The fluid ethanol is used since the intensity of scattered light is much higher than from gaseous hydrogen due to the enhanced particle density.

in subsection 4.3.10, reduces with decreasing spatial resolution in the acquired CCD image a compromise between reduction of read-out noise and performance of post-processing routines has to be found.

- A housing for a spherical retro reflection mirror which back reflects the scattered light that is emitted towards the currently not used side window of the LARA cell (see figure 7.1) was designed and manufactured. An increasing of the intensity of the observed scattered light by up to a factor of two is expected by the retro reflection mirror. This allows to improve the signal-to-noise ratio in the spectrum and hence the precision in long term measurements. A characterisation of the improvement of the signal-to-noise ratio is currently being performed, results will be found in [Her11].
- The intensity of the scattered light can be again enhanced by up to a factor of two by a double pass geometry, i.e. by back reflecting and re-focusing the beam after passing the LARA cell the first time. First tests, performed at Swansea University [Jam10] were successful and showed the feasibility of this method.
- After a replacement of the defective internal mirror of the Triax320 spectrograph the SP500 can be substituted by the Triax320 which also houses three optical gratings but has a smaller f-number and hence a larger light yield (see table 4.2). This will allow to increase the signal-to-noise ratio in high resolution spectra which is beneficial for future depolarisation measurements.

In summary it can be said that several disturbing influences on the LARA setups could be identified and suitable measures for the reduction these could be applied or proposed

within this thesis. The implementation of the proposed measures has to be done in the near future to finally prepare the LARA setups for standard operation in KATRIN. The first proof-of-principle depolarisation measurement with tritium was successful although further investigations have to be done to identify and eliminate the currently unknown systematic effect.

A further field of study in the near future at TLK will be the monitoring of tritiated methane species with the LARA setups. Tritiated methanes can trigger the formation of tritium clusters in the WGTS which have different endpoint energies and hence have an impact on the measured electron β spectrum of KATRIN.

In addition to “standard” Raman Spectroscopy which is applied in the existing LARA setups, advanced spectroscopic methods like Cavity Ring-Down Spectroscopy and Stimulated Raman Spectroscopy will be investigated in the future at TLK to improve the sensitivity and the precision of the determination of the WGTS gas composition by several orders of magnitude. With these advanced techniques a further improvement of the sensitivity of KATRIN beyond the 200 meV/c² level might be possible.

Appendix A

Malfunction in position read-out of LM-10 sensor

The LM-10 sensor is used in the LARA2 setup to measure the laser power and the beam position in vertical and horizontal direction. The sensor is read out every second but the readings are averaged over the period of the acquisition of a Raman spectrum, i.e. typically over 250 s. During run#2 (described in section 5.5) a malfunction of the LM-10 sensor was recognised. After about 80 hours of normal operation of the system, the vertical beam position reading occasionally changed sign. In figure A.1 the raw, i.e. not yet averaged, sensor readings of the vertical beam position and the laser base plate temperature are shown for the relevant interval of run#2. At the beginning the malfunction happened only sporadically, i.e. for individual seconds, but then the frequency of the malfunction gradually increased until all readings were negative.

An actual change of the beam position can be excluded due to two reasons:

- The response time of the LM-10 sensor is of the order of 2-3 seconds due to its design as thermal sensor. Therefore an abrupt change of the beam position would cause a gradual change of the beam position reading but not an individual jump of the position reading as it was seen several times during run#2.
- It was shown in chapter 5 that the vertical beam position is correlated with the laser base plate temperature. This correlation can only be established in this period of run#2 as well if the absolute value of the vertical beam position reading is considered as the actual vertical beam position (see figure A.1).

The malfunction seems to be caused by an internal error in the control electronics of the sensor or in the data acquisition software. Due to the fact that the vertical beam position reading was clearly positive before the beginning of the malfunction the actual vertical beam position can be reconstructed by taking the absolute value of the vertical beam position reading. The vertical beam position reading in run#2 was accordingly corrected before averaging over the 250 s long acquisition time.

This malfunction could not be reproduced in the subsequent measurements. Therefore the origin of the malfunction is still unknown. In order to avoid data loss in case of a repeated malfunction, the LM-10 sensor can be set up in the beam path such that the beam is always slightly off the centre position of the sensor. This allows to reconstruct the data in the same way as it was done in this chapter.

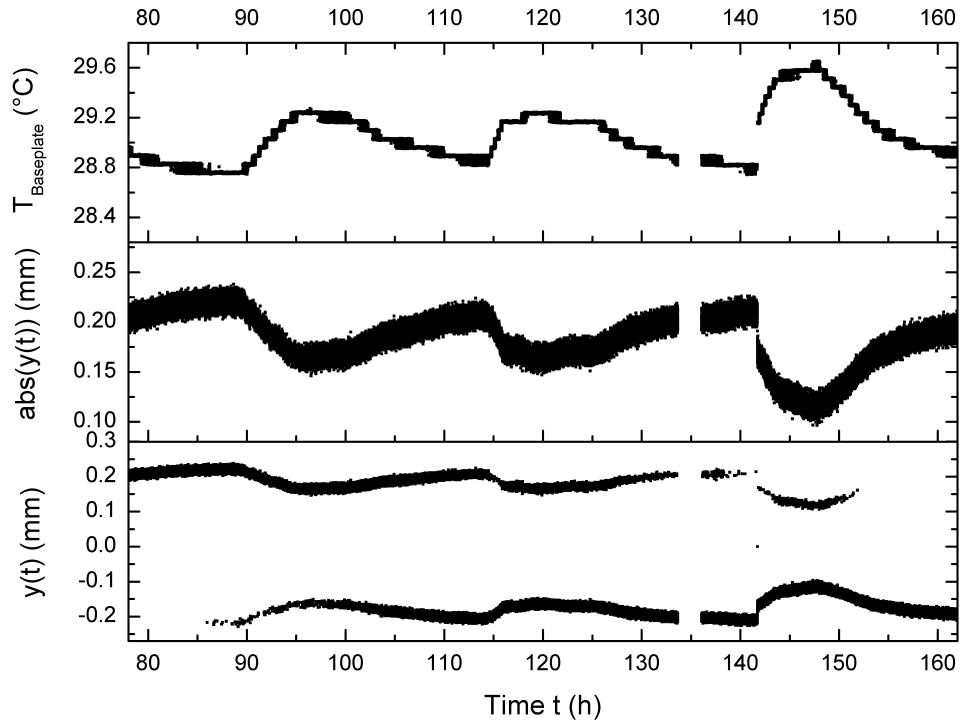


Figure A.1: Malfunction of LM-10 sensor. The raw sensor data is plotted in this figure, i.e. one data point per second. The vertical beam position readings $y(t)$ of the LM-10 sensor change sign due to a malfunction of the sensor. At the beginning the malfunction occurs occasionally but later regularly until all readings are negative in the end. These abrupt changes of the reading do not correspond to actual changes of the beam position since they occur faster than the response time of the sensor. The vertical beam position was clearly positive (about 0.2 mm) before the malfunction. Therefore the actual beam position can be reconstructed by calculating the absolute value of $y(t)$. The absolute value of $y(t)$ is correlated with the temperature of the laser base plate which was already also seen chapter 5. This is further indication that the absolute value of $y(t)$ corresponds to the actual beam position.

Appendix B

Estimate of beam walk at position of LARA cell

The LM-10 sensor, which is placed at the end of the beam path (see figure B.1), is used to measure the beam position during measurement runs. The precision of the beam position measurement in vertical and horizontal direction is $\Delta x = \Delta y = 0.015$ mm. Drifts of the beam position, so called beam-walks, of up to 0.4 mm were observed in the measurements described in chapter 5. Relevant for the stability of the system is however the beam position inside the LARA cell which is placed about 625 mm in front of the LM-10 sensor. Therefore the beam position inside the LARA cell has to be estimated from the measured beam position at the LM-10 sensor.

This can be done using the ray transfer matrix analysis [Dem02] in which a beam is described by its distance r to the optical axis of the setup and by the angle θ it makes with the optical axis. The ray transfer method is based on the assumption that the angle θ is small enough that the approximation $\sin \theta \approx \theta$ can be used. Both beam

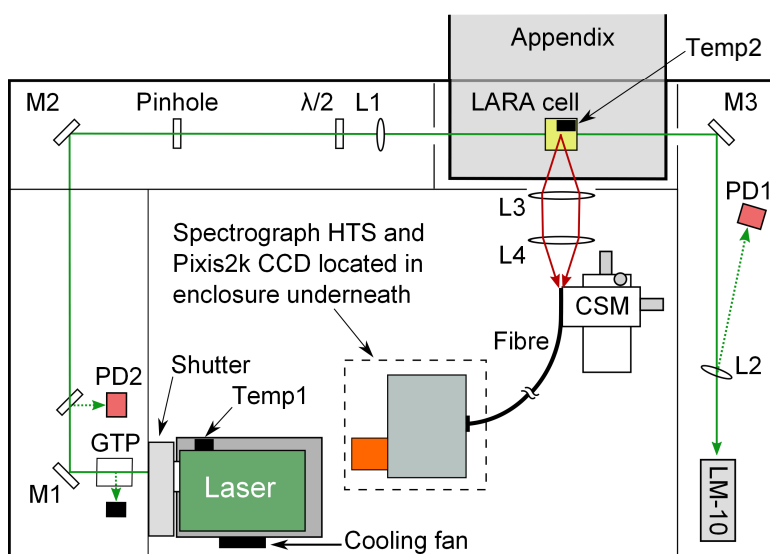


Figure B.1: Experimental setup of LARA2 in run#3

Table B.1: Typical ray transfer matrices of optical elements [Men07]

Element	Ray transfer matrix M
Free propagation of beam over a distance d in medium with constant refractive index	$M_1(d) = \begin{pmatrix} 1 & d \\ 0 & 1 \end{pmatrix}$
Refraction at a flat interface from medium with refractive index n to medium with refractive index n'	$M_2(n, n') = \begin{pmatrix} 1 & 0 \\ 0 & \frac{n}{n'} \end{pmatrix}$
Thin lens with focal length f	$M_3(f) = \begin{pmatrix} 1 & 0 \\ \frac{1}{f} & 1 \end{pmatrix}$

parameters can be combined into a beam vector

$$\begin{pmatrix} r \\ \theta \end{pmatrix} \quad (\text{B.1})$$

that fully describes the orientation of the initial beam. At the end of the optical axis the beam will have in general a distance r' to and an angle θ' with the optical axis and hence a beam vector

$$\begin{pmatrix} r' \\ \theta' \end{pmatrix}. \quad (\text{B.2})$$

The final beam vector is connected to the initial beam vector by a 2×2 ray transfer matrix M that contains all information about the optical setup.

$$\begin{pmatrix} r' \\ \theta' \end{pmatrix} = M \begin{pmatrix} r \\ \theta \end{pmatrix} \quad (\text{B.3})$$

Ray transfer matrices for typical elements in an optical setup can be found in table B.1. If an optical element with ray tracing matrix M is followed by another element with ray tracing matrix M' the overall effect of both elements is given by $M'' = M'M$.

For this coarse estimate of the beam-walk at the position of the LARA cell as a function of the observed beam walk by the LM-10 sensor, the following aspects have to be mentioned:

- Not all optical components are considered in this estimation: The Glan-Taylor-Polariser (GTP), the first beam sampler (located after the GTP), the second beam sampler at the end of the beam path and pinhole since it was fully opened during measurements.

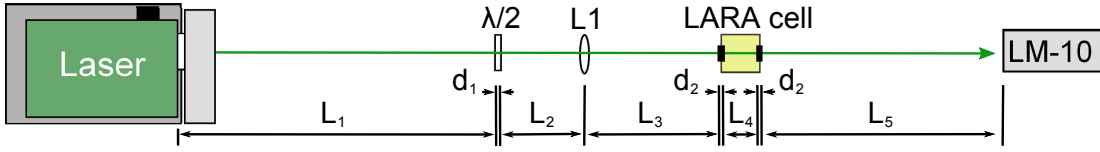


Figure B.2: Hypothetical optical setup for beam walk estimation. All components are aligned along a straight line. Laser windows with the thickness d_2 are located on both sides of the LARA cell.

Table B.2: Parameters for determination of beam walk according to figure B.2

Parameter	Size
L_1	925 mm
L_2	50 mm
L_3	236.7 mm
L_4	17.6 mm
L_5	611.7 mm
Thickness of wave plate d_1	0.93 mm
Thickness of LARA cell windows d_2	4.5 mm
Refractive index of air n	1
Refractive index n_1 of SiO ₂ (material of wave plate and LARA cell windows) at 532 nm	1.46 [Mal65]
Focal length f of focus lens	250 mm

- The laser mirrors are neglected and it is assumed that the optical components are aligned along a straight line, i.e. the optical axis (see figure B.2). The parameters of the setup are given in table B.2.

The total ray transfer matrix of the setup shown in figure B.2 is calculated by multiplying the ray transfer matrices of the individual components

$$\begin{aligned}
 M_{\text{total}} &= M_1(L_5) \cdot \underbrace{M_2(n_1, n) \cdot M_1(d_2) \cdot M_2(n, n_1)}_{\text{Cell window 2}} \cdot M_1(L_4) \cdot \underbrace{M_2(n_1, n) \cdot M_1(d_2) \cdot M_2(n, n_1)}_{\text{Cell window 1}} \cdot \\
 &\quad M_1(L_3) \cdot \underbrace{M_3(f)}_{\text{Focus lens}} \cdot M_1(L_2) \cdot \underbrace{M_2(n_1, n) \cdot M_1(d_1) \cdot M_2(n, n_1)}_{\text{Wave plate}} \cdot M_1(L_1) \\
 &= \begin{pmatrix} -2.4872 & -1554.7310 \frac{\text{mm}}{\text{rad}} \\ -0.0040 \frac{\text{rad}}{\text{mm}} & -2.9024 \end{pmatrix} \quad (\text{B.4})
 \end{aligned}$$

In order to be able to calculate the initial beam vector from the final beam vector

$$\begin{pmatrix} r \\ \theta \end{pmatrix} = M_{\text{total}}^{-1} \begin{pmatrix} r' \\ \theta' \end{pmatrix} \quad (\text{B.5})$$

the total ray transfer matrix has to be inverted

$$M_{\text{total}}^{-1} = \begin{pmatrix} -2.9025 & 1555.862 \frac{\text{mm}}{\text{rad}} \\ 0.0040 \frac{\text{rad}}{\text{mm}} & -2.4887 \end{pmatrix}. \quad (\text{B.6})$$

For the next calculations the parameterisation

$$M_{\text{total}}^{-1} = \begin{pmatrix} a & b \\ c & d \end{pmatrix}. \quad (\text{B.7})$$

of the inverted total ray transfer matrix will be used.

At first the central part of the laser beam will be considered which is at the laser aperture equal to the optical axis, i.e. $r = 0$. From the first row of (B.5) we get $r = ar' + b\theta' = 0$ and hence $\theta' = -a r'/b$. With this expression we can replace θ' in (B.5) since θ' cannot be measured by the LM-10 sensor and we get

$$\theta = r'(c - a/bd). \quad (\text{B.8})$$

In chapter 5 a beam walk in vertical direction of up to $r' = 0.4$ mm due to a temperature drop of 4 K was observed during run#3. If it was only caused by beam pointing instability of the laser, the beam has to move according to (B.8) by an angle of $\alpha = -258 \mu\text{rad}$. This is an enormous drift compared to typical thermal drifts of diode pumped solid state lasers¹.

The ray transfer matrix for the optical setup from the laser to the centre position of the LARA cell is given by

$$\begin{aligned} M_{\text{cell}} &= M_1(L_4/2) \cdot \underbrace{M_2(n_1, n) \cdot M_1(d_2) \cdot M_2(n, n_1)}_{\text{Cell window 1}} \cdot M_1(L_3) \cdot \underbrace{M_3(f)}_{\text{Focuslens}} \cdot M_1(L_2) \cdot \\ &\quad \cdot \underbrace{M_2(n_1, n) \cdot M_1(d_1) \cdot M_2(n, n_1)}_{\text{Wave plate}} \cdot M_1(L_1) \\ &= \begin{pmatrix} 0.00567 & 254.1156 \frac{\text{mm}}{\text{rad}} \\ -0.0040 \frac{\text{rad}}{\text{mm}} & -2.9025 \end{pmatrix} \end{aligned} \quad (\text{B.9})$$

and can be used to calculate how much the beam was shifted away from the optical axis at the central position of the LARA cell. This is done by multiplying M_{cell} with the estimated initial beam vector

$$\begin{pmatrix} r \\ \theta \end{pmatrix} = M_{\text{cell}} \begin{pmatrix} 0 \\ -258 \mu\text{rad} \end{pmatrix} = \begin{pmatrix} -0.065 \text{ mm} \\ 0.00075 \text{ rad} \end{pmatrix} \quad (\text{B.10})$$

¹Thermal beam drifts of the Verdi V5 laser of the LARA1 setup are stated to be smaller than 2 $\mu\text{rad}/\text{K}$ [Ver99]. A reference value for the Excel laser itself is currently not known.

and leads to the result that the beam was shifted by $-0.065 \text{ mm} = -65 \mu\text{m}$ away from the optical axis. The absolute peak intensity in the Raman spectra is expected to decrease by about 85 % in case of such a shift [Sch09] which was not observed during the measurement. A final evaluation is not possible at this point, since the uncertainty of the calculated shift of the beam at the position of the LARA cell is not estimated.

First indications were found in test measurements [Sch10] that the mounts of the beam steering mirrors are affected by temperature variations and hence also introduce a change of the beam direction. Therefore further investigations should be performed to identify the most dominant sources of beam walk in the LARA setup.

Appendix C

Characterisation of wave plate induced beam-walk

The $\lambda/2$ wave plate is used in the LARA2 setup to turn the polarisation angle of the laser. Two wave plates were used within this thesis: A “thick” wave plate made of mica which is placed between glass plates for stabilisation and hence has a total thickness of about 2 mm. It was found that the rotation of the “thick” wave plate caused a displacement of the beam which was not acceptable for the depolarisation measurements, which are described in chapter 6. Therefore a second, “thin” wave plate made of crystalline quartz was installed in the setup which does not need additional glass plates and hence has a thickness of about 0.2 mm. In this chapter the beam walk, which is induced by both wave plates is characterised using the webcam monitor. The pixels of the webcam have a size of $5 \pm 1 \mu\text{m}$ and hence allow to monitor the beam position with a precision of the same order of magnitude.

The experimental setup for the determination of beam walk induced by the “thick” wave plate is shown in figure C.1. Although all available neutral density filters were placed in front of the webcam monitor, the image of the webcam monitor was saturated in the central region of the beam, shown in figure C.3. Nevertheless it is possible to determine the beam position with an uncertainty of about $\pm 1 \text{ pixel} \approx 5 \pm 1 \mu\text{m}$ in horizontal and vertical direction by fitting a Gaussian profiles to the intensity distribution. The beam walk induced by the thin wave plate was measured with a modified experimental setup, shown in figure C.2. The laser intensity was further reduced in comparison to the first measurement by the monitoring of a reflection of the beam instead of the beam itself. The acquired beam profile, shown in figure C.3, is more symmetric and has less noise due to less prominent saturation of the sensor. Therefore the uncertainty of the beam position measurement is reduced to about $\pm 0.3 \text{ pixel} \approx 1.5 \pm 0.3 \mu\text{m}$.

The beam position was measured in both setups for various rotation angles of the wave plates between 0° and 360° . The results are plotted in figure C.4 and show that the “thick” wave plate induces a circular like beam walk with about $7 - 10 \text{ pixels} \approx 35 - 50 \mu\text{m}$ radius. In case of the “thin” wave plate a variation of the beam position within a circular area with about $4 \text{ pixels} \approx 20 \pm 1.2 \mu\text{m}$ radius was observed. It was shown in [Sch09] that a beam walk of about $38 \mu\text{m}$ in vertical direction causes a drop of the observed intensity of scattered light by 22 % while no significant intensity drop, i.e. $< 5 \%$, occurs for beam walks of up to $20 \mu\text{m}$. In the proof-of-principle depolarisation measurement, described in chapter 6, an intensity variation of less than

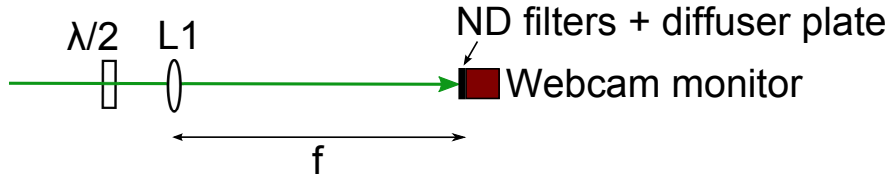


Figure C.1: Experimental setup for determination beam walk due to rotation of “thick” wave plate. The webcam monitor is placed in the focal point of lens L1 (focal length f), i.e. at the regular position of the LARA cell. Three neutral density (ND) filters with a total optical density of $OD = 8.3$, i.e. a transmittance of $10^{-8.3}$ and a glass diffuser plate are placed in front of the webcam monitor to reduce the laser power and to remove interference pattern, respectively. The laser power is reduced to about 5 mW which is the lowest possible setting. The position of the laser beam is monitored by the webcam monitor while the wave plate is gradually rotated.

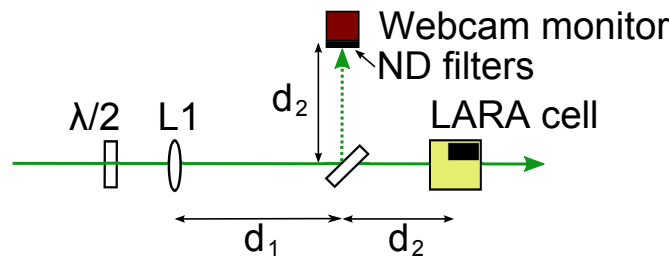


Figure C.2: Experimental setup for determination beam walk due to rotation of “thin” wave plate. An anti reflection coated glass plate is placed into the beam path between the focus lens L1 (focal length f) and the LARA cell. The webcam monitor is placed such that it monitors the reflection of the beam in the focus point of the focus lens, i.e. $d_1 + d_2 = f$. Two neutral density (ND) filter with a total optical density $OD = 7$, i.e. a transmittance of 10^{-7} are placed in front of the webcam monitor to reduce the laser power. The position of the laser beam is monitored by the webcam monitor while the wave plate is gradually rotated.

5 % can be accepted. In later, high accuracy measurements the intensity variation due to the small but still present beam walk should be taken into account.

Therefore, it can be concluded that the “thick” wave plate cannot be used in the depolarisation measurements in which the variation of the intensity of the scattered light is monitored as function of the rotation angle of the wave plate since significant intensity variations are caused by the beam walk. The “thin” wave plate is suitable for the depolarisation measurements since the induced beam walk causes a variation of the observed intensity by less than 5 % which is sufficient for the proof-of-principle measurement that is presented in chapter 6. If possible, the variation of the intensity of the scattered light due to wave plate induced beam walk should be taken into account in the data analysis when the final depolarisation measurements are performed.

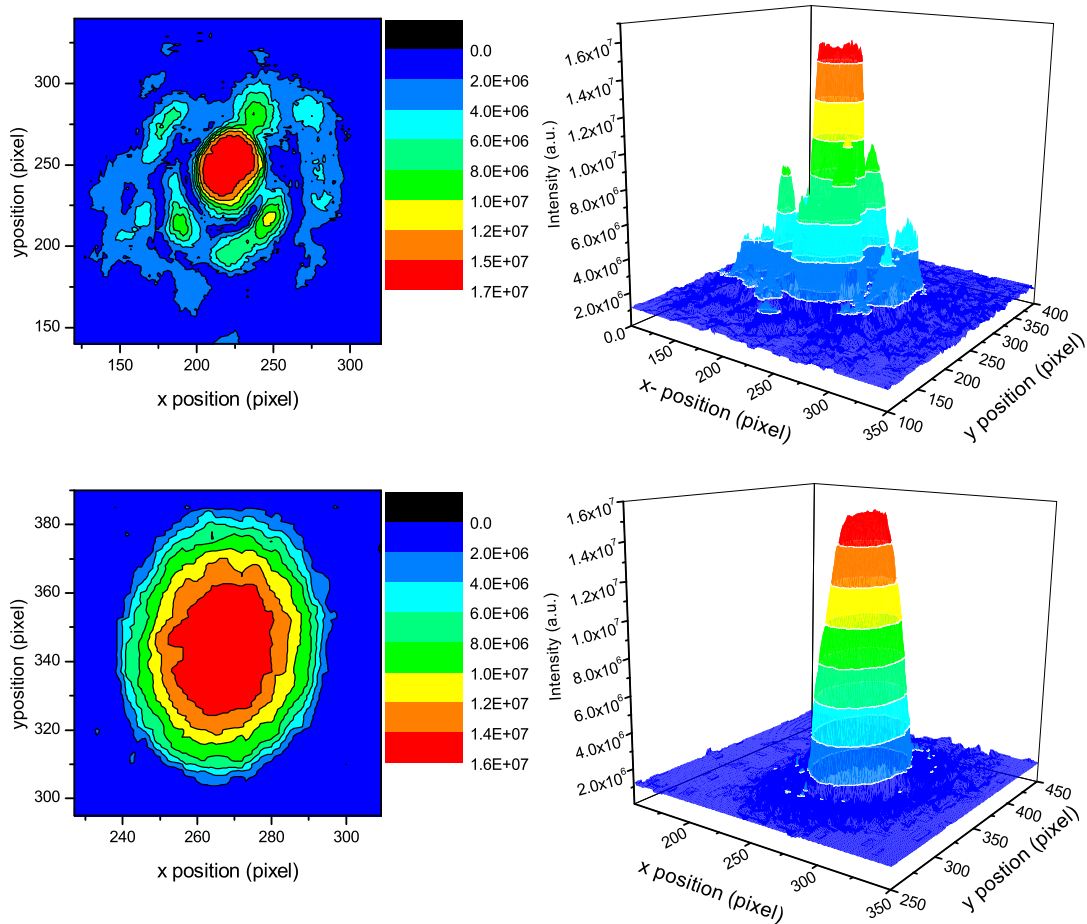


Figure C.3: Beam profiles measured with webcam monitor for characterisation of wave plate induced beam walk. *Top:* Contour plot and 3D intensity profile of the laser beam measured with the experimental setup shown in figure C.1 for the characterisation of beam walk induced by the “thick” wave plate. Although the webcam monitor is saturated in the central region of the laser the beam position can be determined with about ± 1 pixel $\approx 5 \pm 1 \mu\text{m}$ uncertainty by fitting the profile with Gaussian profiles. *Bottom:* Contour plot and 3D intensity profile of the laser beam measured with the experimental setup shown in figure C.2 for the characterisation of beam walk induced by the “thin” wave plate. The webcam is still saturated in the central region of the beam but the uncertainty of the beam position measurement in horizontal and vertical direction is reduced to about ± 0.3 pixel $\approx 1.5 \pm 0.3 \mu\text{m}$ due to the more symmetric intensity profile.

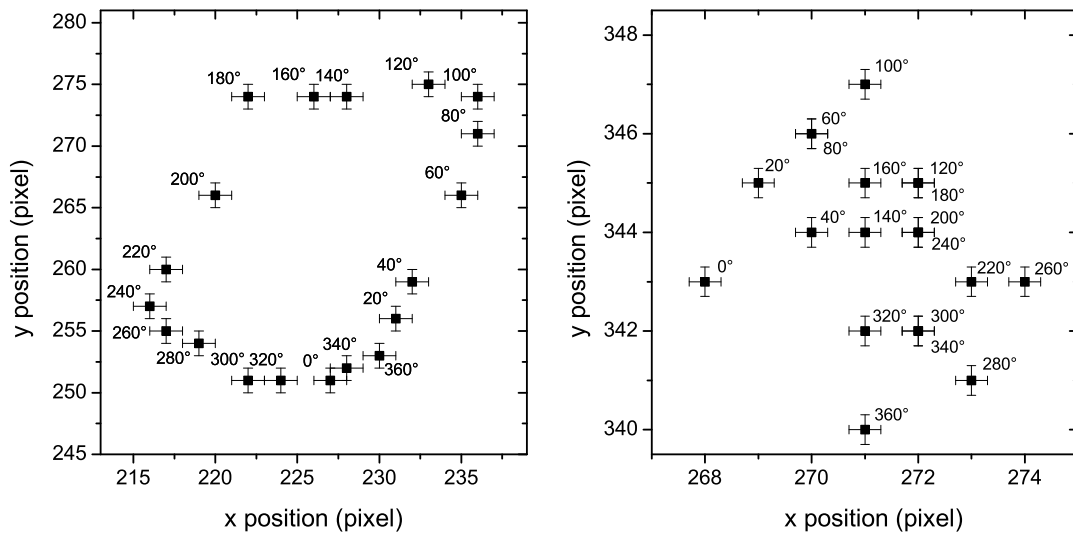


Figure C.4: Beam walk due to rotation of “thick” (left) and “thin” (right). The data points are labelled with the rotation angle of the wave plates. The rotation of the “thick” wave plate causes a circular movement of the beam position with a radius of 7 – 10 pixels. The beam walk due to rotation of the “thin” wave plate is significantly smaller, all data points are contained in a circular area with 4 pixels radius.

Appendix D

ROOT Macro for depolarisation measurement

In this chapter the source code of the ROOT analysis macro can be found that is used in section 6.4 to fit the expected intensity function, see equation (6.2), to the data measured in the depolarisation measurement.

```
#include"TF1.h"
#include"TH1F.h"
#include"TGraph.h"
#include"TCanvas.h"
#include"TFrame.h"
#include"TStyle.h"
#include"TList.h"
#include"TPaveStats.h"
#include"TMath.h"
#include<fstream>
#include<iostream>

// #####
// Global parameters and constants
// #####
// Input and Output
const char datafile[] = "Final_analysis/peaks_all.dat"; //Name datafile
const Int_t graphsize = 48; // Number of data points
const char filename[] = "Plot_peaks_all_FINAL"; // Name of plots

// #####
// Placzek-Teller Factor
// J = 0:
//Double_t const b = 0;
// J = 1:
//Double_t const b = 2./5.;
// J = 2:
//Double_t const b = 2./7.;
// J = 3:
```

```

//Double_t const b = 4./15.;
// J = 4:
//Double_t const b = 20./77.;
// J = 5:
//Double_t const b = 10./39.;

// #####
// Plot options
// Set limits for y-axis in plot?
const bool limits = true; // True = set limits manually
const double y_min = 0; // Minimum of y-axis
const double y_max = 4; // Maximum of y-axis

// #####
// Geometry of experiment
Double_t const r = 7.9; // Radius of aperture in mm
Double_t const d = 25; // Distance of aperture from centre of cell

// #####
// Integration parameters
Double_t const epsilon = 1.e-4; // Integration accuracy
const double* foo = NULL; // Dummy variable necessary for integrations

// #####
// Define line strength function for consideration of solid angle of
// collection optics including the sin(theta) term from integration in
// spherical coordinates
Double_t linestrength(Double_t *x, Double_t *par)
{
  Double_t a = par[0];
  Double_t gamma = par[1];
  Double_t psi_0 = par[2];
  Double_t psi = par[3];
  Double_t theta = par[4];
  Double_t phi = x[0];

  Double_t function = (b*pow(gamma,2)/ 15. + ( pow(a,2) + b*
  pow(gamma,2) / 45. ) * pow(theta,2) + b*pow(gamma,2)/ 15. ) *
  pow(cos (phi - psi + psi_0),2) + ( pow(a,2) + 4. /45. * b*pow(gamma,2)) *
  pow(sin (phi - psi+psi_0),2))*sin(theta);

  return function;
}

// #####
// Integration I: Integrate linestrength function over variable phi
Double_t h(Double_t *x, Double_t *params)
{
  Double_t a = params[0];

```

```

Double_t gamma = params[1];
Double_t psi_0 = params[2];
Double_t psi = params[3];
Double_t theta = x[0];

// Integration limits
double ax = -atan(sqrt(r*r/(d*d)*pow(sin(theta),2) -
pow(cos(theta),2)));
double bx = -ax;

// Definition of line strength function
TF1* func = new TF1("linestrength",*linestrength,ax,bx,5);
// Set Parameters of line strength function
func->SetParameter(0,a);
func->SetParameter(1,gamma);
func->SetParameter(2,psi_0);
func->SetParameter(3,psi);
func->SetParameter(4,theta);
func->SetParNames("a","gamma","psi_0","psi","theta");

Double_t result = func->Integral(ax,bx,foo,epsilon);
delete func;
return result;
}

// #####
// Integration II: Integrate line strength function over variable theta
Double_t g(Double_t *x, Double_t *params)
{
Double_t a = params[0];
Double_t gamma = params[1];
Double_t psi_0 = params[2];
Double_t psi = x[0];

// Integration limits and
Double_t ax = atan( d /r );
Double_t bx = M_PI - atan( d /r );

// Definition of function h
TF1* func = new TF1("h",*h,ax,bx,4);
func->SetParameter(0,a);
func->SetParameter(1,gamma);
func->SetParameter(2,psi_0);
func->SetParameter(3,psi);
func->SetParNames("a","gamma","psi_0","psi");

Double_t result = func->Integral(ax,bx,foo,epsilon);
delete func;
return result;

```

```

}

// #####
void MultiFit_neu2()
{
  gStyle->SetOptFit(11);
  gStyle->SetStatColor(0);
  gStyle->SetPadColor(0);
  gStyle->SetPadBorderMode(0);

  // #####
  // Read data from text file
  std::ifstream input(datafile); // Input file with experimental data
  Double_t* psi = new Double_t[graphsize];
  Double_t* integral = new Double_t[graphsize];
  for(Int_t i = 0; i < graphsize;i++){
    input >> psi[i] >> integral[i];
  }
  input.close();
  std::cout << "File successfully read in." << std::endl;

  // #####
  // Define Graph with exp. Data
  TGraph* gr = new TGraph(graphsize,psi,integral);

  if(limits == true){
    gr->SetMaximum(y_max);
    gr->SetMinimum(y_min);}
  gr->SetTitle("");
  gr->GetXaxis()->SetLimits(-0.3, 7);

  // #####
  // Generate linestrength function + consideration of optics for fitting
  Int_t npar = 3;
  Double_t xmin =psi[0];
  Double_t xmax =psi[graphsize-1];
  TF1* func = new TF1("g",*g,xmin,xmax,npar);

  // #####
  // Initialise fit parameters
  func->SetParameter(0,3); // a
  func->SetParLimits(0,0,100);
  func->SetParameter(1,2); // gamma
  func->SetParLimits(1,0,100);
  func->SetParameter(2,1.4); // psi_0
  func->SetParLimits(2,0,1.6);
  func->SetParNames("a","#gamma","#psi_{0}");

  // #####

```

```

// Fit function to data + Calculation of a/gamma and uncertainty
gr->Fit(func,"R");
double a = func->GetParameter(0);
double gamma = func->GetParameter(1);
double sigma_a = func->GetParError(0);
double sigma_gamma = func->GetParError(1);
double psi_0 = func->GetParameter(2);
double sigma_psi_0 = func->GetParError(2);
double sigma_a_gamma = TMath::Abs(1./gamma) * TMath::Abs(sigma_a) +
TMath::Abs(a/pow(gamma,2)) *TMath::Abs(sigma_gamma);

std::cout << "chi2/dof: " << func->GetChisquare()/func->GetNDF()
    << std::endl;
std::cout << "a = " << a << " +/- " << sigma_a << std::endl;
std::cout << "gamma = " << gamma << " +/- " << sigma_gamma
    << std::endl;
std::cout << "psi_0 = " << psi_0 << " +/- " << sigma_psi_0
    << std::endl;
std::cout << "a/gamma = " << a/gamma << " +/- " << sigma_a_gamma
    << std::endl;

// #####
// Plotting
// Canvas
TCanvas *c1=new TCanvas(filename,"Plot",0,0,1200,800);
c1->SetFillColor(kWhite);
c1->SetBorderMode(kWhite);
c1->GetFrame()->SetBorderSize(12);

gr->Draw("AP");

gr->SetMarkerStyle(21);
gr->SetMarkerSize(1);
gr->SetMarkerColor(2);
gr->GetXaxis()->SetTitle("Polarisation angle #psi (rad)");
gr->GetYaxis()->SetTitle("Peak area (a.u.)");
gr->GetXaxis()->CenterTitle(kTRUE);
gr->GetYaxis()->CenterTitle(kTRUE);

// Plot of fit parameters
(TPaveStats*)gr->GetListOfFunctions()->FindObject("stats");

// #####
// Saving of plots
c1->SaveAs(".eps");
std::cout << "Program finsished" << std::endl;
}

```


Bibliography

- [Aal05] C.E. Aalseth et al., *The proposed Majorana ^{76}Ge double-beta decay experiment*, Nucl. Phys. B (Proc. Suppl.) **138** (2005) 217-220.
- [Als09] A. Alshahrie, *Internal note*, University of Swansea, Wales (2009).
- [ACT05] *HTS Lens spectrograph*, Princeton Instruments / Acton, Rev A0 (2005).
- [Ahm01] Q.R. Ahmad et al., *Measurement of the Rate of $\nu_e + d \rightarrow p + p + e^-$ Interactions Produced by ^8B Solar Neutrinos at the Sudbury Neutrino Observatory*, Phys. Rev. Lett. **87** 7 (2001).
- [Aki05] D. Akimov et al., *EXO: an advanced Enriched Xenon double-beta decay Observatory*, Nucl. Phys. B (Proc. Suppl.) **138** (2005) 224.
- [Ale88] E.N. Alexeyev et al., *Detection of the neutrino signal from SN 1987A in the LMC using the INR Baksan Underground Scintillation Telescope*, Phys. Lett. B **205** (1988) 209.
- [Ali05] E. Aliu et al., *Evidence for Muon Neutrino Oscillation in an Accelerator-Based Experiment*, Phys. Rev. Lett. **94** (2005) 081802.
- [Ans92] P. Anselmann et al., *Solar neutrinos observed by GALLEX at Gran Sasso*, Phys. Lett. B **285** (1992) 376-389.
- [Ase00] V.N. Aseev et al., *Energy loss of 18 keV electrons in gaseous T_2 and quench condensed D_2 films*, Eur. Phys. J. D **10** (2000) 39-52.
- [Bab10] M. Babutzka, *Untersuchung eines verfahrenbaren Monitordetektors zur Überwachung der Aktivität des β -Zerfalls in der kryogenen Pumpstrecke des KATRIN-Experiment*, Universität Karlsruhe (2010).
- [Bak04] S.V.N Bhaskara Rao et al., *Rovibrational matrix elements of polarizability of HD, HT and DT molecules*, Journal of Quantitative Spectroscopy Radiative Transfer **87**, 203–210 (2004).
- [Bah06] J.N. Bahcall et al., *10,000 Standard Solar Models: A Monte Carlo Simulation*, Astrophys. J. S. **165** (2006) 400-431.
- [Ben03] C. L. Bennett et al., *The Microwave Anisotropy Probe Mission*, Astrophysical Journal **583** 1 1-23 (2003), DOI: 10.1086/345346.
- [Ber72] K. E. BERGKVIST, *A high-luminosity, high-resolution study of the end-point behaviour of the tritium β -spectrum*, Nucl. Phys B **39**, 317 (1972).

- [Bis69] D. M. Bishop, L. M. Cheung, *Radiative corrections for the vibrational energy levels of the $X^1\Sigma_g^1$ state of the hydrogen molecule*, J. Chem. Phys. **69**, 1881 (1978).
- [Bra88] C.B. Bratton et al., *Angular distribution of event from SN1987A*, Phys. Rev. D **37** (1998) 12.
- [Bri66] N. J. Bridge and A. D. Buckingham, *Polarization of Laser Light Scattered by Gases*, Proc. Roy. Soc. Lond. Math. Phys. Sci. **295** 1442 334-349 (1966).
- [Bun77a] P. R. Bunker and R. E. Moss, *The breakdown of the Born-Oppenheimer approximation: the effective vibration-rotation hamiltonian for a diatomic molecule*, Molecular Physics **33** 2 417-424 (1977).
- [Bun77b] P. R. Bunker and R. E. Moss, *Application of the effective vibration-rotation hamiltonian to H^2 and D^2* , Molecular Physics **33** 2 425-429 (1977).
- [Car72] R. W. Carlson and W. R. Fenner, *Absolute Raman Scattering Cross-Section of Molecular Hydrogen*, Astrophysical Journal **178** 551-556 (1972).
- [Cha14] J. Chadwick, Verh. d. Deutsch. Phys. Ges. **16** 383 (1914).
- [Cha32a] J. Chadwick. *Possible existence of a Neutron*, PRSL, A136, 692.
- [Cha32b] J. Chadwick. *The existence of a Neutron*, Proceedings of the Royal Society of London. Series A, Containing Papers of a Mathematical and Physical Character **136** 930 692-708 (1932).
- [Cho07] S. Choudhury, *Experimental efforts in search of ^{76}Ge Neutrinoless Double Beta Decay*, arXiv:0704.0063 (2007).
- [Dan62] G. Danby, J-M. Gaillard, K. Goulianos, L. M. Lederman, N. Mistry, M. Schwartz, J. Steinberger, *Observation of High-Energy Neutrino Reactions and the Existence of Two Kinds of Neutrinos*, Phys. Rev. Lett. **9**, 36-44 (1962).
- [Dav68] R. Davis, Don S. Harmer and Kenneth C. Hoffmann, *Search for Neutrinos from the Sun*, Phys. Rev. Lett. **20** (1968) 1205-1209.
- [Dia09] M. Ubieto-Díaz et al., *A Broad-Band FT-ICR Penning Trap System for KATRIN*, Int. J. Mass Spectroscopy, **288**, 1-5, (2009).
- [Dem02] W. Demtröder, *Experimentalphysik 2, Elektrizität und Optik*, 2. Auflage, Springer (2002).
- [Dos08] N. Doss and J. Tennyson., *Excitations to the electronic continuum of ^3HeT + in investigations of T_2 β -decay experiments.*, Journal of Physics B At. Mol. Opt. Phys. **41**, 125701 (2008)
- [Edw78] H. G. M. Edwards, D. A. Long, H. R. Mansour, *Pure rotational and vibration-rotational Raman spectra of tritium, $^3\text{H}_2$* , J. Chem. Soc., Faraday Trans. 2 **74** 1203 - 1207, (1978) DOI: 10.1039/F29787401203.
- [Eic08] F. Eichelhardt et al., *First tritium results of the KATRIN test experiment TRAP*, Fus. Sci. Tech. **54** (2008).

- [Eic09] F. Eichelhardt, *Measurement of the Tritium pumping properties of a 4.2 K Argon Condensate for the Cryogenic Pumping Section of KATRIN*, PhD Thesis, Universität Karlsruhe (2009).
- [Eic06] J. Eichler and H.J. Eichler, *Laser - Bauformen, Strahlführung, Anwendungen*, 6. Auflage, Springer (2006).
- [Ell87] S.R. Elliot et al., *Direct evidence for two-neutrino double-beta decay in ^{82}Se* . Phys. Rev. Lett. **59** 2020 (1987).
- [Egu03] K. Eguchi et al., *First Results from KamLAND: Evidence for Reactor Antineutrino Disappearance*, Phys. Rev. Lett. **90** (2003) 021802.
- [Eng92] U. Engelmann, *Ramanspektroskopische und massenspektroskopische Untersuchungen der Wasserstoffisotope und isotope substituierter Methane*, PhD-Thesis, KfK 5116:2 (1992).
- [Exc06] *Excel technical data sheet*, Laser Quantum (2006).
- [Fer34] E. Fermi, *Versuch einer Theorie der β -Strahlen.*, Z. Phys. **88** 161 - 177 (1934)
- [Fix96] D. J. Fixsen et al., *The Cosmic Microwave Background Spectrum from the Full COBE FIRAS Data Set*, Astrophys.J.Suppl. **473** 576 (1996), doi:10.1086/178173.
- [Fuk98] Y. Fukuda et al., *Measurements of the Solar Neutrino Flux from Super-Kamiokande's First 300 Days*, Phys. Rev. Lett. **81**, 1158–1162 (1998).
- [Gol62] D. M. Golden, B. Crawford, *Absolute Raman Intensities. I. Method for Molecules in the Gas Phase* J. Chem. Phys. **36** 1654 (1962), doi:10.1063/1.1732793.
- [Gri69] V. Gribov and B. Pontecorvo, *Neutrino astronomy and lepton charge*, Phys. Letters B **28** 7, 493-496 (1969).
- [Gro09] S. Grohmann, *Stability analyses of the beam tub cooling system in the KATRIN source cryostat*, Cryogenics **49** 8 (2009) 413-420.
- [Hak04] H. Haken and H.C. Wolf, *Atom- und Quantenphysik*, 8.Auflage, Springer (2004).
- [Hak06] H. Haken and H.C.Wolf, *Molekülphysik und Quantenchemie*, 5.Auflage, Springer (2006).
- [Han04] St. Hannestad, *Neutrinos in Cosmology*, arXiv:hep-ph/0404239 v1 (2004).
- [Her39] G.Herzberg, *Molekülspektren und Molekülstruktur, I. Zweiatomige Moleküle*, Verlag von Theodor Steinkopff, Dresden, Leipzig (1939)
- [Her65] L. J. F. Hermans et al., *The polarizability of the hydrogen-isotopes and of ortho and para hydrogen*, Physica **31** 10, 1567-1574 (1965).
- [Her11] P. Herwig, *Diploma thesis in preparation*, Karlsruhe Institute of Technology , 2011.

- [Hir88] K.S. Hirata et al., *Observation in the Kamiokande-II detector of the neutrino burst from supernova SN1987A*, Phys. Rev. D **38** (1988) 12.
- [Hug08] K. Hugenberg, *Design of the electrode system for the KATRIN main spectrometer*, Diploma thesis, University Münster (2008).
- [Hun84] J. L. Hunt, J. D. Poll, L. Wolniewicz, *Ab initio calculation of properties of the neutral diatomic hydrogen molecules H_2 , HD, D_2 , HT, DT, and T_2* , Can. J. Phys. **62**, 1719 (1984).
- [Ish52] Ishiguro et al., *On the Polarizability of the Hydrogen Molecule*, Proc. Phys. Soc. A **65** 178 (1952).
- [Jam10] T. James, *Internal note*, 2010.
- [KAT05] KATRIN Collaboration, *KATRIN Design Report 2004*, FZKA **7090** (2005).
- [Kla04] H.V. Klapdor-Kleingrothaus, *Search for neutrinoless double beta decay with enriched ^{76}Ge in Gran Sasso 1990-2003*, Phys. Lett. B **586** (2004) 198-212.
- [Koe70] W. Koechner, *Thermal lensing in a Nd:YAG laser rod*, Appl. Opt. **9** **11**, 2548-2553 (1970).
- [Kol64] W. Kolos, L. Wolniewicz *Accurate Adiabatic Treatment of the Ground State of the Hydrogen Molecule*, J. Chem. Phys. **41** 3663-3673 (1964).
- [Kol86] W. Kolos, K. Szalewicz, H. Monkhorst, *New Born-Oppenheimer potential energy curve and vibrational energies for the electronic ground state of the hydrogen molecule*, J. Chem. Phys. **84** 6, 3278-3283 (1986).
- [Kom10] E. Komatsu et al., *Seven-year Wilkinson microwave anisotropy probe (WMAP) observations: Cosmological interpretation*, arXiv:1001.4635v1 [astro-ph.CO], submitted to Astrophys.J.Suppl.
- [Kod01] K. Kodama et al., *Observation of tau neutrino interactions*, Physics Letters B, **504** 3, 218-224 (2001).
- [Kra05] Ch. Kraus et al., *Final Results from phase II of the Mainz Neutrino Mass Search in Tritium β Decay*, Eur. Phys. J. C **40** (2005) 447-468.
- [Krui83] P. Kruit, F. H. Read, *Magnetic field paralleliser for 2π electron-spectrometer and electron-image magnifier*, J. Phys. E: Sci. Instrum. **16** 313 (1983).
- [Leb10] M. Leber, *Update on the Rear Section: turning a conceptual design into a technical design*, presentation at the 18. KATRIN collaboration meeting, (2010).
- [Lew07] R.J. Lewis, *Development of a Raman System for In-line Monitoring of Tritium at the Karlsruhe Tritium Neutrino (KATRIN) Experiment*, PhD-Thesis (2007).
- [Lob03] V.M. Lobashev, *The search for the neutrino mass by direct method in the tritium beta-decay and perspectives of study it in the project KATRIN*, Nucl. Phys. A **719** (2003) 153.

- [Lob99] V.M. Lobashev et al., *Direct search for mass of neutrino and anomaly in the tritium beta-spectrum*, Phys. Lett. B **460** (1999) 227-235.
- [Log10] E. Gundermann, *Personal communication*, Technical support Logitech (2010).
- [Lon02] D.A. Long, *The Raman Effect*, John Wiley & Sons, Ltd (2002).
- [Lor02] T.J. Loredo and D. Q. Lamb, *Bayesian analysis of neutrinos observed from supernova SN 1987A*, Phys. Rev. D **65** (2002) 063002.
- [Lub80] V. A. Lubimov, E. G. Novikov, V. Z. Nozik, E. F. Tretyakov and V. S. Kosik, *An estimate of the ν_e mass from the β -spectrum of tritium in the valine molecule* Phys. Lett. **94B**, 266-268 (1980).
- [Mal65] I. H. Malitson, *Interspecimen Comparison of the Refractive Index of Fused Silica*, J. Opt. Soc. Am. **55**, 1205-1208 (1965).
- [Mau09] D. Maurel, *Designstudien zur Messung der Aktivität der Tritiumquelle im KATRIN-Experiment mit Röntgenstrahlung*, Diploma thesis, Universität Karlsruhe (2009).
- [Men07] R. Menzel, *Photonics, Linear and Nonlinear Interactions of Laser Light and Matter* 2nd Edition, Springer(2007).
- [Mic06] D.G. Michael, *Observation of Muon Neutrino Disappearance with the MINOS Detectors in the NuMI Neutrino Beam*, Phys. Rev. Lett. **97** (2006) 191801.
- [Mor77] G. A. Morris, *Methane formation in tritium gas exposed to stainless steel* Report of Lawrence Livermore Laboratory, UCRL-52262 (1977).
- [Mro32] B. Mrowaka, *Wellenmechanische Berechnung der Polarisierbarkeit des Wasserstoffmoleküls* Zeitschrift für Physik A Hadrons and Nuclei **76** 5, 300-308 (1932).
- [Ott08] E.W. Otten and Ch. Weinheimer, *Neutrino mass limit from tritium β decay*, Rep. Prog. Phys. **71** (2008).
- [Pau30] Wolfgang Pauli, *Offener Brief an die Gruppe der Radioaktiven bei der Gauvereins- Tagung zu Tübingen, 4. Dez. 1930*. Reproduced in: R. Kronig and V. Weisskopf (Eds.), Wolfgang Pauli, Collected Scientific Papers, Vol. 2, Interscience, New York (1964) 1316 - 1317.
- [PDG08] C. Amsler et al. (Particle Data Group), *Review of Particle Physics*, Phys. Lett. B **667** (2008) and 2009 partial update for the 2010 edition.
- [Ped08] M. Pedretti et al., *Cuore Experiment: The search for neutrinoless double beta decay*, Int. J. Mod. Phys. A **23** (2008) 3395.
- [Per09] W.J. Percival et al., *Baryon acoustic oscillations in the Sloan Digital Sky Survey Data Release 7 galaxy sample*, MNRAS **401** 4 2148-2168 (2009).
- [Pho06] *Data sheet of Photodiode SM1PD1A*, Coherent, 14000-S01 Rev. A (2006).
- [PIX07a] *PIXIS:2K Specifications*, Princeton Instruments, RevB0 (2007).

- [PIX07b] *PIXIS:400 Specifications*, Princeton Instruments, RevD0 (2007).
- [Pla33] G. Placzek and E. Teller, *Die Rotationsstruktur der Ramanbanden mehratomiger Moleküle*, Zeitschrift für Physik A Hadrons and Nuclei **81** 3, 209-258 (1933).
- [Pon67] B. Pontecorvo, J. Expl. Theoret. Phys. **53** 1717 (1967).
- [Pow09] *PowerMax-USB/RS Sensors*, Coherent, MC-xxx-09-0M1009 (2009).
- [Pow07] *Smart QuadSensors*, Coherent, http://www.coherent.de/fileadmin/redakteur/pdf/Quadsensor_LM-1__bis_LM_5000_.pdf, (2007).
- [Pra10] M. Prall, *PhD thesis in preparation*, Universität Münster (2010).
- [Pri09] F. Priester, *Systematische Untersuchungen zum Stabilitätsverhalten des KATRIN Tritiumloop*, Diploma thesis, Karlsruhe Institute of Technology (2009).
- [Reb09] H. Rebscher, *Personal communication*, Coherent (2010).
- [Rei09a] S. Reimer, *Ein elektrostatisches Dipolsystem zur Eliminierung von Ionen in der DPS2-F. des KATRIN Experimentes*, Diploma thesis, Universität Karlsruhe (2009).
- [Rei09b] J. Reich, *Magnetfeldmessungen und Designarbeiten für das EMCS Luftspulensystem am KATRIN Hauptspektrometer*, Diploma thesis, Universität Karlsruhe (2009).
- [Rei56] F. Reines and C.L. Cowan, *The Neutrino*, Nature **178** (1956).
- [Rei59] F. Reines and C.L. Cowan, *Free Antineutrino Absorption Cross Section. I. Measurement of the Free Antineutrino Absorption Cross Section by Protons*, Phys. Rev. **113**, 273–279 (1959).
- [Rep83] W. W. Repko and C. Wu, *Radiative corrections to the end point of the tritium β decay spectrum*, Phys. Rev. C **28** 6, 2433–2436 (1983)
- [Rie09] A. G. Riess et al., *A Redetermination of the Hubble Constant with the Hubble Space Telescope from a Differential Distance Ladder*, Astrophysical Journal **699** 539, doi:10.1088/0004-637X/699/1/539.
- [Row71] R. L. Rowell, G. M. Aval, J. J. Barrett, *Rayleigh-Raman Depolarization of Laser Light Scattered by Gases*, Journal of Chemical Physics **54** 1960-1964 (1971).
- [RSK10] *RSK - Raman spectroscopy for KATRIN, version 2.0.1* developed by R. Lewis under GNU licence, University of Swansea, Wales (2010).
- [Ryc83] J. Rychlewski, *Frequency dependent polarisabilities for the ground state of H₂, HD, and D₂*, J. Chem. Phys. **78** 12, 7252-7259 (1983).
- [Sch87] C. Schwartz and R.J. LeRoy, *Nonadiabatic eigenvalues and adiabatic matrix elements for all isotopes of diatomic hydrogen*, J. Mol. Spectrosc. **121** 2 (1987) 420-439.

- [Sch97] N.Schmitz, *Neutrinophysik*, Teubner (1997).
- [Sch05] S. Schoenert et al., *The GERmanium Detector Array (GERDA) for the search of neutrinoless $\beta\beta$ decays of ^{76}Ge at LNGS*, Nucl. Phys. B (Proc. Suppl.) **145** (2005) 242.
- [Sch08] U. Schmitt, *Entwicklung eines Monitordetektors für das KATRIN-Experiment*, PhD thesis, Universität Karlsruhe (2009).
- [Sch09] M. Schlösser, *First Laser Raman measurements with tritium for KATRIN and studies of systematic effects of the LARA-setup*, Diploma thesis, Karlsruhe Institute of Technology (2009).
- [Sch10] M. Schlösser, *Internal note*, 2010.
- [Sis04] M. Sisti et al., *New limits from the Milano neutrino mass experiment with thermal microcalorimeters*, Nucl. Instr. Methods A **520** (2004) 125-131.
- [Sis07] E. Andreotti et al., *MARE, Microcalorimeter Arrays for a Rhenium Experiment: A detector overview*, Nucl. Inst. Meth. Phys. Res. A **572** 1 (2007) 208-210.
- [Smi05] E. Smith, G. Dent, *Modern Raman spectroscopy: a practical approach*, Wiley (2005).
- [Spe00] *Acton Research SpectraProTM* Roper Scientific, Rev A0, (2000).
- [SPE09] R.J. Lewis, *SpecGen*, LabVIEW program, (2009).
- [Stu07] M. Sturm, *Bestimmung der Tritiumflussreduktion einer Tritium-Argon-Frostpumpe für das Neutrinomassenexperiment KATRIN*, Diploma thesis, Universität Karlsruhe (2007).
- [Stu10a] M. Sturm et al., *Monitoring of All Hydrogen Isotopologues at Tritium Laboratory Karlsruhe Using Raman Spectroscopy*, Laser Physics **20**, 2, 493-507 (2010).
- [Stu10b] M. Sturm, *PhD thesis in preparation*, Karlsruhe Institute of Technology (2010).
- [Sut04] J. Sutton and J. Driscoll, *Rayleigh scattering cross sections of combustion species at 266, 355, and 532 nm for thermometry applications*, Opt. Lett. **29**, 2620-2622 (2004).
- [Tay01] D.J. Taylor, M. Glugla and R.-D. Penzhorn, *Enhanced Raman sensitivity using an actively stabilized external resonator*, Rev. Sci. Instrum. **72** (2001) 1970.
- [TLA09] *Technische Liefer- und Abnahmebedingungen für Apparate und Behälter*, Tritiumlabor Karlsruhe (2009).
- [Tri02] *Triax series*, Jobin Yvon Horiba, OSD-0002 Rev.A (2002).
- [Tur01] S. Turck-Chièze et al., *Solar Neutrino Emission Deduced from a Seismic Model*, Astrophys. J. Lett. **555**, L69 (2001).

- [Ver99] *Verdi V2, V5 data sheet*, Coherent (1999).
- [Vei87] D. K. Veirs, G. M. Rosenblatt, *Raman line positions in molecular hydrogen: H₂, HD, HT, D₂, DT, and T₂*, *Journal of Molecular Spectroscopy* **121** 2, 401-419 (1987).
- [Wan09] N. Wandkowsky, *Field and trajectory calculations for the KATRIN main spectrometer and air coil system*, Diploma thesis, Universität Karlsruhe (2009).
- [Web99] R. Weber, B. Neuenschwander, H. P. Weber, *Thermal effects in solid-state laser materials*, *Optical Materials* **11**, Issues 2-3, 245-254, (1999), DOI: 10.1016/S0925-3467(98)00047-0.
- [Wei03] Ch. Weinheimer, *Laboratory Limits on Neutrino Masses*, in: G. Altarelli and K. Winter, *Neutrino Mass*, Springer (2003).
- [Wol78] L. Wolfenstein, *Neutrino oscillations in matter*, *Phys. Rev. D* **17** (1978).
- [Wol83] L. Wolniewicz, *The X¹Σ_g¹ state vibration-rotational energies of the H₂, HD, and D₂ molecules*, *J. Chem. Phys.* **78**, 6173 (1983).
- [Wue10] S. Wuestling, et al., *Results from a 64-pixel PIN-diode detector system for low-energy beta-electrons*, *Nucl. Instr. and Meth. A* (2010), doi:10.1016/j.nima.2010.03.120.
- [Zac09] M. Zacher, *Electromagnetic design and field emission studies for the inner electrode system of the KATRIN main spectrometer*, Diploma thesis, University of Münster (2009).

Danksagung

Diese Arbeit wäre ohne die Mitarbeit und Unterstützung vieler Personen nicht möglich gewesen.

Ich danke Prof. Dr. Guido Drexlin, da er mir die Durchführung dieser sehr interessanten Arbeit ermöglicht hat.

Ich danke Dr. Beate Borschein für ihr, deutlich über das Maß des Selbstverständlichen hinausgehende, Engagement und die exzellente Betreuung dieser Diplomarbeit.

Ich danke Prof. Dr. Helmut H. Telle für die fachliche Unterstützung und die Übernahme der Zweitkorrektur.

Weiteren Dank gilt Michael Sturm und Magnus Schlösser für die sehr gute gemeinsame Zusammenarbeit und Betreuung.

Ich danke der gesamten Laser Raman Gruppe (Ahmed Alshahrie, Dr. Beate Borschein, Timothy James, Dr. Richard Lewis, Magnus Schlösser, Monika Sirch, Michael Sturm und Prof. Dr. Helmut Telle) für die hervorragende Zusammenarbeit.

Für die Unterstützung beim Aufbau und Betrieb des LARA2 Systems danke ich Hans-Dieter Adami, Helmut Dittrich, Siegfried Horn, Nando Gramlich, Frank Kramer, Florian Priester, Frank Rehlinghaus, Dieter Stern sowie den Mitarbeitern der IK Werkstatt.

Ich danke Benjamin Leiber und Ioan-Catalin Petrutiu für die Unterstützung zur Lösung numerischer Integrale.

Für die Bereitstellung von Temperaturdaten des Campus Nord danke ich Martin Kohler.

Ich allen weiteren Mitarbeitern im Umfeld des TLKs für ihre Hilfsbereitschaft: Catalin-Gabriel Alecu, Nikolas Bekris, Dr. Uwe Besserer, Erhan Cilbir, Dr. Ion Cristescu, Dr. David Demage, Eleonore Fanghänel, Manfred Göckel, Norbert Kernert, Beate Kloppe, Zoltan Köllö, Sylvia Krieger, Thanh Long Le, Christin Melzer, Robert Michling, Harald Moosmann, Dirk Osenberg, Ana Parracho, Christoph Plusczyk, Thomas Polzer, Eva Porter, Peter Schäfer, Rolf Schön, Peter Schuster, Karl-Heinz Simon, Sascha Singer, Robert Wagner, Stefan Welte, Dr. Jürgen Wendel, Werner Wurster und den Mitarbeitern des Strahlenschutzes.

Ich bedanke mich bei allen Mitarbeitern bei KATRIN. Besonderer Dank gilt den Diplomanden und Doktoranden für eine interessante, gemeinsame Zeit.

Zuletzt möchte ich mich bei meiner Familie und ganz besonders bei Judith bedanken, die mir in der anstrengenden Phase der Diplomarbeit den Rücken frei gehalten haben und mich stets in meiner Arbeit unterstützt haben.